Plasmon Decay Dynamics in Hybrid Metal/Doped-semiconductor Nanostructures

Supervisor:

Prof. Luca Pasquini

Submitted by:

Matteo Marchesini

Co-supervisor:

Prof. Andrea Baldi

Academic Year 2019/2020

God made the bulk; surfaces were invented by the devil.

Wolfgang Pauli [1]

Abstract

The study of interactions between plasmonic nanomaterials *and* dielectrics *is a thriving field of research, which in recent years proved that such nanostructures can be applied in a wide range of applications, from sensing to catalysts. These are all based on the nanoscale surface interactions happening between the nanomaterials and their surrounding environment. In this thesis, the possible interaction between* plasmonic nanoparticles *and the V doping states in the* Anatase (TiO_2) *bandgap, rather than in their undoped counterpart, is studied. The aim is to better understand the dynamics of these phenomena, and obtaining insights on the V states position in the TiO_2 bandgap. The work done encompasses all the steps needed to achieve the experimental results: from the preparation and characterisation of the samples, to the simulations of the phenomena involved, until the actual measurements of their optical properties and the discussion of the results. The findings achieved are not decisive in explaining the dynamics involved, but preliminary interpretations could be formulated. Moreover, the specific investigations displayed in this thesis have never been done before in literature, and the work performed might be used in the future as a starting point for more thorough and deep studies of these phenomena.*

Contents

1 - Introduction

Among the many branches that make up the vast field of *nanotechnology*, one of the most prominent and widely studied is the one concerning *metallic nanostructures*. When illuminated by certain frequencies of light, the electrons of these objects can enter in an oscillatory state, called *plasmon*, which interacts with the surrounding environment. This peculiar property make them suited for a variety of applications, from *chemical sensing* of Hydrogen to their use as *catalysts* in water-splitting reactions. It is in fact known that these *plasmonic nanomaterials* can interact with semiconductors and insulators near them, through a *direct-charge-transfer* from their surface to the dielectric usually called *chemical interface damping* (*CID*). Recent literature largely explored this phenomenon in wide bandgap semiconductors, for which there is evidence of a possible "coupling" between the *plasmonic excitation* in the nanomaterial and *electron promotion* to the conduction band in the semiconductor.

The focus of this thesis is to try to find this "coupling", but between the *plasmons* and *electronic transitions* to or from *doping states* in the bandgap of a semiconductor. This approach is a novelty, as no study in this specific subject can be found in literature. In fact the presence of such a coupling is not certain, and investigations are necessary to ascertain its existence.

As dielectric, thin films of *Titanium dioxide* (TiO_2) in its *Anatase* phase deposited on a glass substrate were used. TiO_2 has a wide gap, starting to absorb light only in the near *ultraviolet*. Doping such a material can thus make it absorb *visible* light, with the possibility of tuning the specific wavelength "ad libitum" using the right dopant, making it suited to any application involving *visible light*. In fact it is widely used as photocatalytic agent in many applications which involve that range of the light spectrum. For the purpose of this work, *Vanadium* (V) was used as dopant. This choice partly comes from the fact that the exact position of V states in the TiO_2 gap is unknown, and the experiments performed could give hints on where they actually are (it is expected $\approx 2.2eV$ below the conduction band). The fact that thin-film deposited on transparent substrates had to be used is dictated by the necessity

to perform measurements of transmission spectra, for which bulk materials are not suited.

The nanomaterials used for this project are *Ag* and *Au* nanoparticles. The choice was done because of the extensive literature concerning them, and their cheap and wide commercial availability.

Eight samples in total were prepared, 4 of *undoped* Anatase and 4 with 8% *V* doping, on which were deposited nanoparticles of different size, in order to have a wider range of possible interactions, both above and below the expected *V* doping levels energy. The combination of *metallic nanoparticles* and *semiconductor film* constitute the *nanostructure* to be studied in this thesis. Film preparation was performed at the *University of Bologna*, while nanoparticle deposition and all the experimental analysis were carried out at the *Dutch Institute For Future Energy Research* (*DIFFER*) in Eindhoven.

The thesis is structured to first provide a theoretical discussion of the phenomena that are studied.

Then, a thorough explanation of the experimental procedures carried out in this project is given. These range from the thin film deposition, to the techniques used to characterise their physical properties (thickness, refractive index and microscopic imaging), how the nanoparticles were placed on the samples, and to the final measurements of their optical properties were performed.

Finally, an overview of the results obtained is provided, before the concluding remarks of this project are discussed.

2 - Theoretical Foreword

In this chapter, an overview of the theoretical concepts on which this thesis is based are presented.

As the phenomena studied in this work involve nanoparticles deposited on semiconductor thin-films, understanding the properties of these systems is crucial. Concerning the semiconductor films, only TiO_2 (and only V doping) is treated as it is the sole material studied. Regarding the nanoparticles, a wider argument is discussed. In fact they have more tunable properties compared to a film of a specific material, as their size and shape too influence their light interaction capabilities.

Finally, as this thesis emphasizes on the interaction between nanoparticles and their surrounding environment, an introduction to nanoparticles-dielectrics interactions is discussed. This is an emerging field of plasmonics, promising interesting applications in the near future, including practical the use of nanoparticles as photocatalytic agents in chemo-physical reactions, such as water-splitting an synthetic fuels production.

2.1 V-Doped TiO_2 Thin Films

TiO_2, generally referred as *Titania*, is a semiconductor with bandgap located in the *least energetic ultraviolet* (UVA) portion of the light spectrum. It is commonly found in iron ores and is widely used in industry, especially as an extremely reflecting white pigment and UV shield in sunscreen creams. It possesses three different crystalline structures, which can be obtained from its amorphous state via annealing at different temperatures [2].

Due to its wide bandgap, TiO_2 doesn't absorb *visible light* (VIS). That is why it is perfectly suitable for being doped, in order to allow interband absorption of VIS and *near-infrared* (NIR) light, with the theoretical possibility of engineering it to the desired photon energies. As V is the chemical element following Ti in the periodic table, it is the ideal doping candidate to obtain deep dopant stated in the TiO_2 bandgap.

Ref/Year	Amorphous TiO_2 [eV]	Rutile [eV]	Anatase [eV]	Brookite [eV]
[4]/2018	$3.0 - 3.29$	$3.0 - 3.37$	3.2(I), 3.53(D)	$3.13 - 3.45$
[2]/2017	-	3.0	3.2(I)	-
[5]/2013	-	3.03	3.2(I)	-
[6]/2012†	-	$3.39 - 3.73$	$3.60 - 4.05$(I)	$3.30 - 3.68$
[7]/2002†	-	≈ 3.0	-	-

Table 2.1: Literature on the band gaps of *amorphous TiO_2*, *Rutile*, *Anatase* and *brookite*. In the *Anatase* column (I) indicates the value referred to an *indirect* transition, wheread (D) concerns *direct* ones.
†: these values come from mathematical simulations rather than experimental measurements; notice that they are overestimated in comparison to the experimental ones.

In order to study the optical properties of any of the aforementioned materials, it is necessary for them to be prepared in the form of thin films. This way, the samples to be studied will remain decently transparent, allowing for analysis of their transmission spectrum other than the reflection one only. However, it must be taken into consideration that the structure of a thin film gives rise to inevitable artefacts in such spectra, due to the interference of light reflected by the interfaces *thin film – air* and *thin film – substrate*.

2.1.1 TiO_2 Phases & Bandgaps

From its amorphous state, three separate crystalline phases of TiO_2 may arise by annealing it at different temperatures: *Rutile* (tetragonal), *Anatase* (tetragonal), *brookite* (orthorombic) [3]. Of these phases, only the first one is stable, while the other two are metastable and may be converted into Rutile at high temperatures (above 650^oC) [2].
The general consensus in literature is that *Rutile* and *brookite* have direct bandgaps while *Anatase* has an indirect one, and also a direct one at slightly higher energy. There is not, however, perfect agreement on the actual value of the bandgaps [2, 4–7]. Literature shows that *Rutile* and *brookite* have similar gaps, while *Anatase* has it slightly wider and *amorphous TiO_2* falls in between them, as shown in Table 2.1, but no certain values can be found. These discrepancies might actually be due to artefacts in the measurements used to calculate the bandgap values. As the experiments are usually performed on films of materials, this can cause artificial shifts of the bandgap, directly correlated to the thickness of the films [4].
As the samples prepared and studied in this thesis are made in *Anatase*, only

this phase will be taken into consideration from here onwards. In summary: *Anatase* is a tetragonal crystalline phase of TiO_2 obtained annealing its amorphous state at temperatures below 600^oC, has an indirect bandgap $\approx 3.2\ eV$ and a direct gap $\approx 3.5\ eV$.

2.1.2 V Dopant States in Anatase (TiO_2)

Being neighbouring transition metals in the periodic table of elements, V and Ti have many similar properties. They both have mostly empty $3d$ shells, similar atomic radius and mass, and same oxidation states. This make the two elements easily interchangeable between them at an atomic level, without inducing too much strain in the crystalline structure. This translates to the fact that V is a good dopant for Ti-based non-metallic compounds. This way, V states form in the bandgap of the compound, and may also cause a shrinkage of the gap itself. Focusing on TiO_2 as a compound, its doping with V can effectively cause it to be optically active in the VIS. This mean that such a compound could be used as photocatalyst for many reactions, using solar light rather than UV sources for it to be activated [8].

References can be found for mathematical modelling of the band structure of $V : TiO_2$. These models however regard only the stable *Rutile* phase, which shows a shallow dopant state, which eventually merges with the conduction band at doping levels above 8% [7, 9]. On the contrary, literature concerning the *Anatase* phase is more focused on experimental results. The general scientific consensus is that V doping causes a broadening of the range of light absorbed by *Anatase*, through and apparent "bandgap shrinking" from $\approx 3.2\ eV$ down to $\approx 2.7 - 2.5\ eV$, depending on doping level [8]. Recent works however examined the position of the V states through photocatalytical processes, coming to the conclusion that these dopant states lie deep in the bandgap, $\approx 2.2\ eV$ below the conduction band at $\approx 3\%$ V doping [10]. This could explain the apparent shrinking of *Anatase* bandgap if it is also taken in consideration that, as the doping levels increase, the dopant states can widen into small interbands which can also overlap with the valence band. A summary of these findings is shown in Figure 2.1.

As the literature references are not exhaustive on the subject, an analysis on possible interactions between plasmonic nanoparticles of known plasmon energy could give insight on the real position and nature of such V states in the bandgap of *Anatase*. The arising of such an interaction at specific wavelengths could in fact mean that at those energies lie an active dopant state. These aspects will also be covered in Section 4.6.
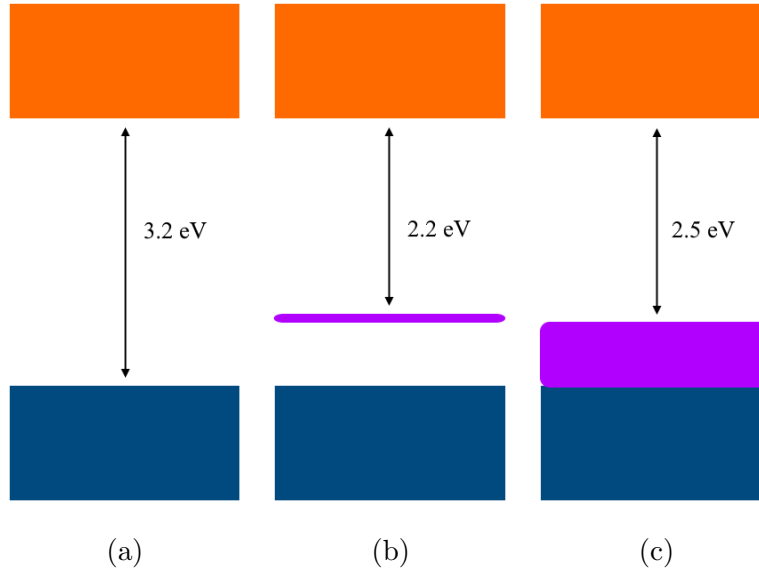
Figure 2.1: Overview of the bandgap of pristine *Anatase* (a), of the *V* dopant state (b), and of the *V* interband which may arise at high doping levels (c).

2.1.3 Thin Film Interference

When an electromagnetic wave reaches an interface between two materials with different refractive index, part of the wave is transmitted through the second material and part of it is reflected. Due to the nature of thin film materials, which are deposited on a substrate that mechanically supports them, at least three of such reflections take place: at the air-film interface, at the film-substrate one, and finally at the substrate-air interface. These reflections are schematised in Figure 2.2.

The resulting effect of these reflections is that, at great distance from the interfaces, certain wavelengths of light might interfere constructively or destructively, causing fringes in the spectrum. These fringes appear both in transmitted and reflected spectra, due to the possibility of having more reflections inside the layers of the sample, which are transmitted forward through the substrate of the film.

In first approximation, the fringe distribution can be described by Bragg's law

$$n\lambda = 2d\sin\theta \tag{2.1}$$

where n is any positive integer, λ is the light wavelength, d is the layer thickness, and θ is the incident angle. However, for a better modelling of the phenomena, the deviation of light when passing through the interfaces must be taken into
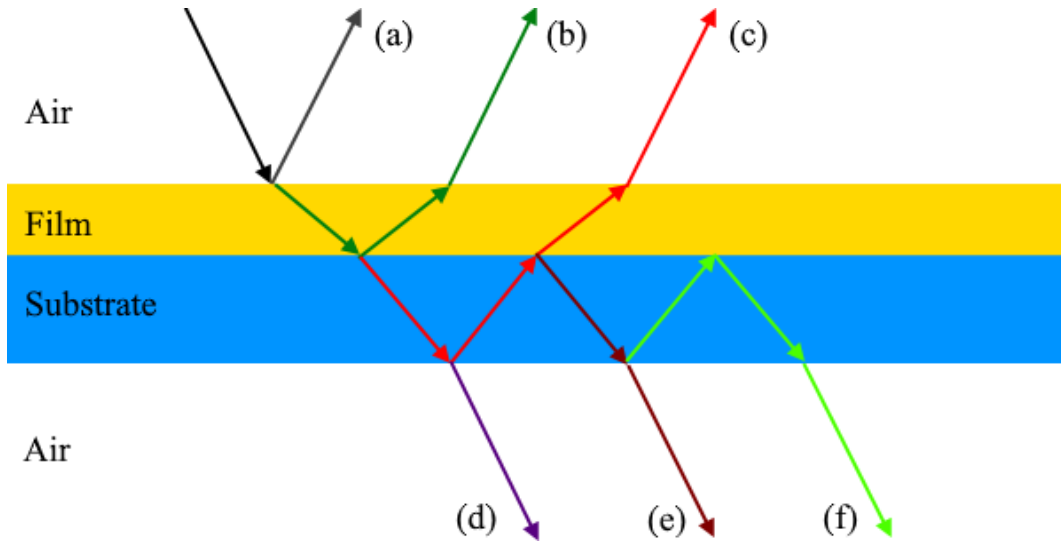
Figure 2.2: Graphical representation of some of the possible light reflections happening in a thin film sample: (a) simple reflection; (b) reflection at the film-substrate interface; (c) "deep" reflection; (d) simple transmission; (e) transmission from double-reflection; (f) transmission from four-fold-reflection

considerations. This way it is possible, known the complex refractive index of the film and of the substrate, to simulate the transmitted and reflected spectra of the sample [11, 12]. As the interference fringes produced are dependent only on the refractive index and the thickness of the materials, if one of these two quantities is known the other can be obtained by adequately modelling the shape and position of such fringes.

The presence of this interference phenomenon is detrimental to achieving good quality measurements, as the fringes can alter significantly the data, tainting its analysis by messing or covering important features of the spectrum. Besides a good modelling of the samples which can take into consideration the disturbs, different approaches can be found in literature to deal with these fringes, and potentially remove them. The main way of doing so, concerning the transmitted spectrum, is to normalise it to the absorbed power [13, 14]. This can be applied in practice by measuring the transmission (T) and reflection (R) spectra with a 90° incident beam of light and applying the following [4]

$$T_c = \frac{T}{1 - R} \tag{2.2}$$

thus obtaining the corrected transmission spectrum (T_c), devoid of interference fringes.

Finally, it must be noted that these interferences only happen when the in-

terfaces are flat enough to not allow the dispersion of the incident light. Very rough films, or roughening the substrate can in fact negate the interference entirely without requiring any mathematical effort.

2.2   Plasmon Resonant Nanoparticles

When stimulated by an external electromagnetic field, the nearly-free-electrons on the surface of metals can be excited in a state of collective oscillation. The intensity of this light-electron interaction peaks at a specific frequency called *plasmon frequency*, where the light absorbed by the metal increases significantly. The value of this frequency depends on the chemical element and crystalline structure of the metal. In the case of metallic nanostructure, including nanoparticles, a similar phenomenon called *localised surface plasmon resonance* (*LSPR*) happens. But other than the material properties, size and shape and arrangement contribute to define this LSPR frequency. This gives the possibility to fine tune the energy at which plasmonic states arise, to best suit it to specific purposes.

After being excited to a plasmonic state, the electrons tend to relax into their ground state dissipating their excess energy. The relaxation process is not unique, and electrons have different ways to perform it. They way they do it can be influenced by the environment surrounding the plasmonic structure, as discussed in Section 2.2.2.

Of particular interest concerning this thesis is the *chemical interface damping* (*CID*), which consist of a direct charge transfer between the plasmonic structure and the surrounding medium rather than an exchange of energy.

Moreover, in recent times the interest in how the plasmonic states of different nanostructures interact with dielectric materials increased significantly in literature. This is because evidence has been found that plasmonic nanostructures can be effectively used as catalysts in chemical reactions, or in sensing applications.

2.2.1   Plasmon Resonance in Metallic Nanoparticles

In the Drude model, an approximated formulation of the dielectric function of a metal can be written as

$$\epsilon(\omega) = -\frac{\omega_p^2}{\omega} \tag{2.3}$$

$$\omega_p^2 = \frac{4\pi n e^2}{m^*} \tag{2.4}$$

where ω is the frequency of the light interacting with the metal, ω_p is the *plasmon frequency* of the metal, n and m^* are respectively the electron density and effective mass of the material [15]. It has been known for more than half a century that thin metallic films show peaks of light and electron absorption at the energy $\hbar\omega_p$ [16]. This is due to the formation of *plasmons*. They are non-radiative electromagnetic surface waves that propagate in a direction parallel to the interface between the metal and the surrounding dielectric, formed when the incident light or electron beam resonate at integer multiples of ω_p [17]. Plasmons are not unique to metallic thin films, and in the case of metallic nanostructures, their electrons can be excited in a peculiar kind of plasmonic resonance: the LSPR. As this thesis focuses on using metallic nanoparticles as plasmon-excitable items, only these will hence be discussed.

LSPR happens in nanoparticles with dimensions smaller than the wavelength of the exciting light, and when its frequency matches the one of the electronic oscillation. The LSPR frequency is mainly determined by the material they are made of (chemical element & crystalline structure) and their size, with smaller diameters giving higher resonance energies [18–21]. Other than that, the material surrounding the particles also plays a role in determining the position of the LSPR peak, and deviations from a spherical shape can give rise to resonance shifts or splitting [18, 19, 22]. Given the wide variety of metals available and of diameters a nanoparticle can be made of, it is possible to choose among an amazingly wide range of plasmon frequencies, according to the specific requirements. In practice, there are constraints due to the particle manufacturing processes, which make extremely small ($< 10nm$ diameter) particles difficult to produce with an acceptable and reliable quality [20, 21]. Moreover, oxidation of the nanoparticle surface can compromise their long term reliability, and that is why there is a focus in industry and research alike to use noble metals particles.

The practical applications of plasmonic nanoparticles require that they are either suspended in a colloidal solution, or deposited on a material with which they can interact. An issue which can arise is that, due to their small size, the van-der-Waals interaction between particles near each other can cause them to cluster together. The clusters of nanoparticles have non-predictable sizes and shapes that inevitably shift or split the plasmon resonance. This is a problem concerning especially nanoparticles kept in solution for long periods of time, or dropcasted onto materials. To prevent this from happening, nanoparticles are usually "capped" with dielectric shells which weakly influence the plasmonic resonance but at the same time reduce the clustering phenomenon [20, 21]; complementarily, different deposition techniques such as *spin-coating* can be used to prevent the particles to come too close to each other [23]. On the other hand, if an ordinate array or structure of plasmonic nanoparticles can

be fabricated, the mutual interaction between them ca be used to improve and further manipulate their light absorption property [17, 19, 24].

2.2.2 Plasmon Relaxation Dynamics

To understand why the medium surrounding the nanoparticles influences the plasmon resonance frequency, a more detailed insight into how the plasmonic oscillation relax back into their ground state must be obtained.

After the electrons are excited in a high energy state (the plasmon) by an external field, they inevitably tend to decay back to their ground state at a rate $\gamma_{plasmon}$. In their work, Besteiro et al [25] identify three contributions to this decay rate:

$$\gamma_{plasmon} = \gamma_{Drude} + \gamma_{inter-band} + \gamma_{hot-electrons} \ . \tag{2.5}$$

The first two terms of (2.5) come from *bulk* contributions:

 – γ_{Drude} comes from the the scattering of the oscillating electrons by phonons and defects, in analogy with the Drude interpretation of electron energy loss due to collisions;

 – $\gamma_{inter-band}$ represent the inter-band relaxation of the electron-hole couples, which can be created by either LSPR excitation or from direct photon absorption.

The last term of (2.5) describes the generation of energetic *electron-hole pairs* in a nanostructure, and represent a generalisation of the *surface-scattering* mechanism that electrons undergo when reaching the nanoparticle-dielectric interface. In fact, *hot electron* generation does happen at the surface, but also in eventual hot spot regions inside a particle. $\gamma_{hot-electrons}$ can itself be separated in two different contributions [26]:

 – *e-e scattering*, which is a fast radiative process dominating at high energies;

 – *e-phonon scattering*, describing the slow thermalisation of hot electrons through lattice interactions, which is prevalent at low energies.

A graphic overview of all the processes described so far is represented in Figure 2.3. The main effect of these relaxation processes is to either shift or change the width of the plasmon absorption and scattering peaks. From the analysis of these two quantities, informations about the neighbouring region of the particles can be obtained. Though γ_{Drude} and $\gamma_{inter-band}$ depend solely on
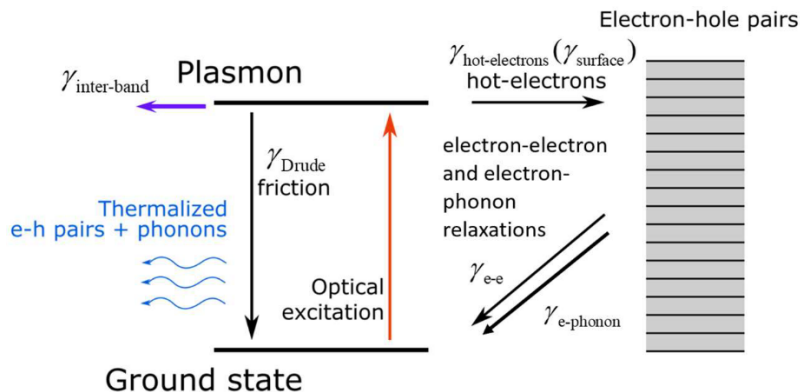
Figure 2.3: Diagram of the processes of plasmon decay; details described in the text. **From:** L. Besteiro et al., *Figure 2.a*, [25].

bulk properties and are not sensitive to the surrounding environment, the surface effects of $\gamma_{hot-electrons}$ are extremely sensitive and constitute an important short-range (nm range) probe of dielectric properties and interactions [22].

In recent times, however, a new way in which plasmonic nanoparticles interact with their surrounding medium through *direct charge-transfer*, rather than electromagnetic interactions. This phenomenon, called *chemical interface damping* (*CID*), is extremely surface-sensitive, and will be discussed in more detail in the next section.

2.2.3   A Focus on Chemical Interface Damping (CID)

Chemical interface damping (*CID*) is a direct decay mechanism of plasmons into an interfacial charge transfer state, entirely avoiding the intermediate creation of hot electrons [27]. The physical manifestation of such a phenomenon consist of a "damping", i.e. an additional widening, of the plasmon absorption and scattering linewidth [27, 28].

Though it has been mostly neglected, in recent times there has been a revived interest in this decay dynamics. This is due to the fact that, as the CID process involves direct interactions between a plasmonic nanoparticle and its neighbouring medium, it is an extremely sensitive and powerful instrument to both probe and influence its surroundings. Quantitative analysis of the plasmonic linewidth broadening are in fact possible, giving deep insights into the processes happening at the nanoparticle-dielectric interface [24, 29].

Moreover, not only the presence, but also the absence of CID can be used to investigate a variety of materials. It has been suggested by Parente et al. [30] that CID can interact with empty mid-gap states; as these states are occupied

11
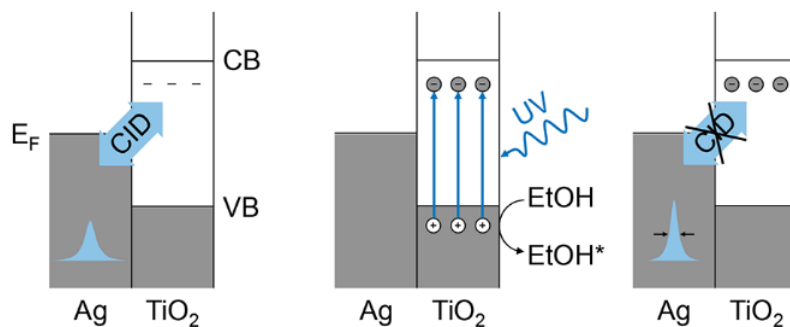
Figure 2.4: Schematic energy diagram of the Ag/TiO2 interface before (left), during (center), and after (right) UV irradiation used to pump electrons in shallow mid-gap states. The resulting shrinking of the plasmon linewidth is interpreted of a lack of the widening usually caused by CID. **From:** M. Parente et al., *Figure 4*, [30].

by electrons, the plasmon linewidth shrinks indicating that CID may become forbidden (see Figure 2.4). This evidence, if further confirmed, could make CID an important tool in studying the dopant states in semiconductors and insulators, and such an analysis will be tempted in this thesis too.

2.2.4 Photocatlyst & Sensing Applications

Through the relaxation processes described in Section 2.2.2 & especially Section 2.2.3, plasmonic nanostructures can easily interact and "couple" with the materials surrounding them. They are in fact optimal candidates to act as catalyst in various reactions, or to be used in sensing applications.

Concerning the photocatalytic effect, a prime focus is the use of plasmonic nanoparticles to improve the efficiency of photoelectrochemical water splitting, thus producing H_2 efficiently from solar power [23]. The main process involved is the direct-charge-transfer happening between the particle and the water during the plasmon relaxation (CID) [24, 29]. As of today these processes are still being studied to a fundamental level; but if engineering catalytic nanostructures that cover most of the solar spectrum is possible, they would be a valid addition to other form of production of "green" H_2.

Regarding the sensing applications of plasmonic nanoparticles, the localised enhancement of the electromagnetic field near the particles renders them useful in probing the dielectric environment within a few nm of their surfaces. They have in fact been used in biological studies regarding local dielectric variation under light and in surface-enhanced Raman sensing experiments [17, 19, 29]. Other applications recently found concern the use of plasmonic nanostructures

as charge sensors [18], and in H_2 detection exploiting the change in plasmon frequency that happens at the particles after the Hydrogen is adsorbed [31]. H_2 sensing at pressures below its flammability limit and below have already been achieved in laboratory settings [32]; an industrial application might soon be available, moving closer to reality the realisation of safe and widespread distribution of H_2 for transport applications.

3 - Experimental Procedures

In this chapter, the various experimental techniques used during the preparation of this thesis will be discussed. First it will be explained how the samples were realised; then the techniques used to characterise their physical properties (structural and electrical) are described. The spectroscopic instruments and procedures used to characterise the optical properties of the samples are shown. Finally, the technique used to deposit the nanoparticle solutions on the different samples are discussed.

As the aim of the discussion is mainly practical, it will be focused in describing the scientific procedures performed and the equipment used. Proper context will be provided regarding the reasons behind the use of the specific techniques, as well as brief theoretical explanations of the phenomena investigated when necessary.

3.1 Anatase Thin Film Preparation

Many techniques exist to deposit thin film of materials on either rigid or flexible substrates. For the purpose of this thesis, a *magnetron sputterer* was chosen, to deposit amorphous TiO_2 films on glass substrates.

After the deposition, the samples are to be annealed into the *Anatase* phase of TiO_2.

Finally, the films are plasma cleaned in order to remove any superficial contaminants and improve the quality of further measurements.

3.1.1 TiO_2 Magnetron Sputtering Deposition

Sputtering is a process in which atoms from a solid "source", called *target*, are emitted following collisions from highly energetic gas particles. Sputterers consist of a vacuum chamber in which a rarefied inert gas is placed. Then a high voltage is applied between the target (cathode) and where the sample will be placed (anode). This triggers the ionisation of the gas which becomes plasma,
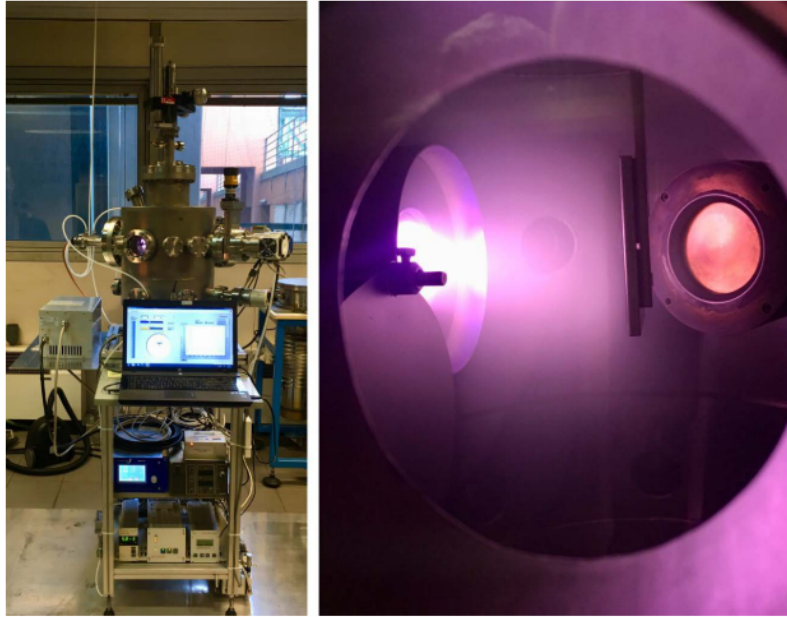
Figure 3.1: (left) The sputterer setup used; (right) the apparatus while performing a TiO_2 deposition, with the Ar plasma clearly visible. **_From:_** M. Bischi and L. Pasquini, _Figura 5.1_, [34].

and its ions are accelerated towards the target. After the impact, fragments of the target are ejected towards the anode, where they are absorbed by the substrate causing the formation of a film on top of it [33]. Both conductive and non-conductive materials can be used as targets, but in the latter case the voltage source must be AC in order to allow the activation of the sputtering process. The thickness of the deposited film will be proportional to the time spent in line of sight of the target.

The instrument used during this work, shown in Figure 3.1, was provided by the laboratory of Prof. Pasquini at the University of Bologna; its structural and operative details are described by Bischi and Pasquini [34], and were used to properly operate the device. The sputterer works with Ar as inert gas and can be used in "radio-frequency configuration" (RF) to deposit insulators and semiconductors such as the amorphous TiO_2 of which the target is made. The instrument was calibrated so that a direct correspondence between deposition time and thickness was known. To obtain the desired doping of the samples, a number of V strips were radially attached to the target as schematically shown in Figure 3.2: the amount of V deposited changed together with the number of strips attached, following a previously measured trend.

The substrates over which the thin films were deposited are $120 \mu m$ thick,
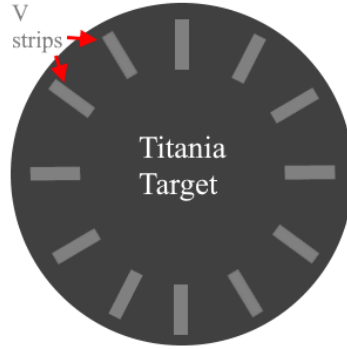
Figure 3.2: Schematic representation of the V strips disposition on the TiO_2 target of the sputterer. Reducing the number of strips reduces the resulting V doping level in the deposited samples.

$20 \times 20 mm$ $Menzel^{TM}$ *microscope coverslips* in Borosilicate. The material choice was done considering the relative smoothness of its surface, their cheapness and wide availability, and the prediction that no significant experimental feature would be found at energies comparable to the UV opacity limit of glass. Throughout this thesis preparation 8 samples were produced, 4 of which made of $\approx 8\%$ V $[at.\%]$ doped *Anatase*. Another batch of 8 samples with intermediate doping ($2 \div 4\%$ V $[at.\%]$) was also deposited, to be used as "training set" to test the experimental procedures before using them on the actual samples. Nonetheless, all the samples were deposited the same way:

– glass substrates were thoroughly cleaned with acetone, rinsed with distilled water and blew with compressed air;

– samples were deposited in $\approx 8 \cdot 10^{-3} mbar$ Ar atmosphere;

– deposition time was $24min$, which should correspond to a thickness $\approx 50nm$;

– samples were stored in a 3D printed case for storage and transport (Figure 3.3).

Finally, to check whether the doping calibration was correct, a thick dummy sample was deposited in the 8% V configuration and analysed through SEM (*Cambridge Stereoscan 360*). Figure 3.4a shows a side-view of the dummy, used to estimate its thickness. Then five X-ray spectra were measured in different regions, shown in Figure 3.4b. By the relative peak intensity of the various elements, it was determined that the V $at.$ content ranged from 6.73% to 8.74%, averaging at 7.96%; the full results are reported in Table 3.1.
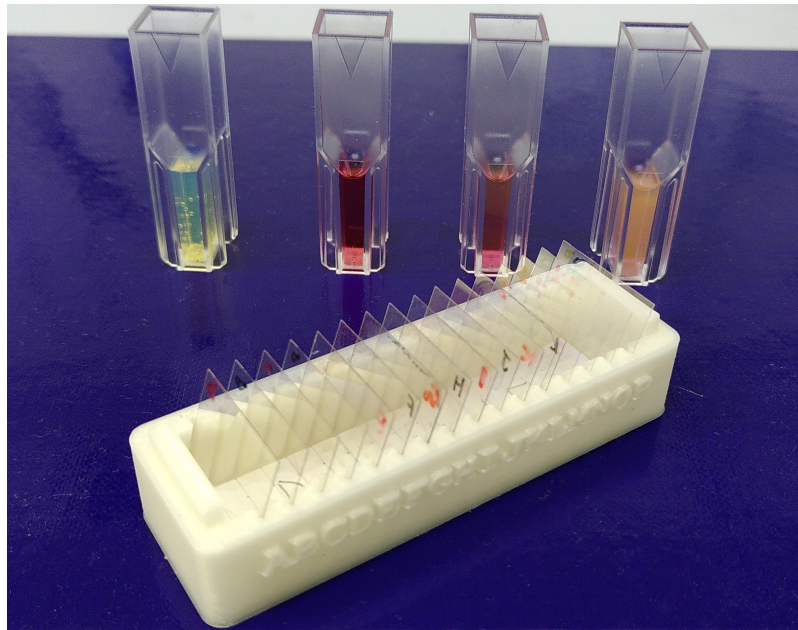
Figure 3.3: All the deposited samples are placed in their custom case, 3D printed at the University of Bologna by A. Piccioni. In the background, four cuvettes containing the nanoparticles solutions that will be deposited on the samples: (left to right, chemical element followed by particles diameter) *Ag* 50*nm*, *Au* 20*nm*, *Au* 50*nm*, *Au* 100*nm*. Notice how the difference in diameter of Gold nanoparticles corresponds to a difference in their colour.

3.1.2   Titania Annealing into Anatase Phase

As the sputterer target made of *amorphous Titania*, so are the deposited films. Thermal treatment was then necessary in order to obtain TiO_2 films in the required *Anatase* phase. The oven used for the process is a *Heraeus* tubular oven, with a *K thermocouple* and *PID* temperature controller. Based on literature evidence [2] and previous experience, all samples underwent an in-air annealing @400^oC for an overnight ($\approx 15 - 16\ h$ inside the oven).
No particular attention was posed in defining the heating and cooling curves, as it was known that they would not have influenced the lattice formation. An estimate of the temperature rates was anyway made, giving $\approx 5^oC/min$ for heating and $\approx 3^oC/min$ for cooling.

3.1.3   Plasma Cleaning of Surfaces

After the deposition and the annealing processes, the samples surface might be tarnished by external contaminants coming from the sputterer or from the
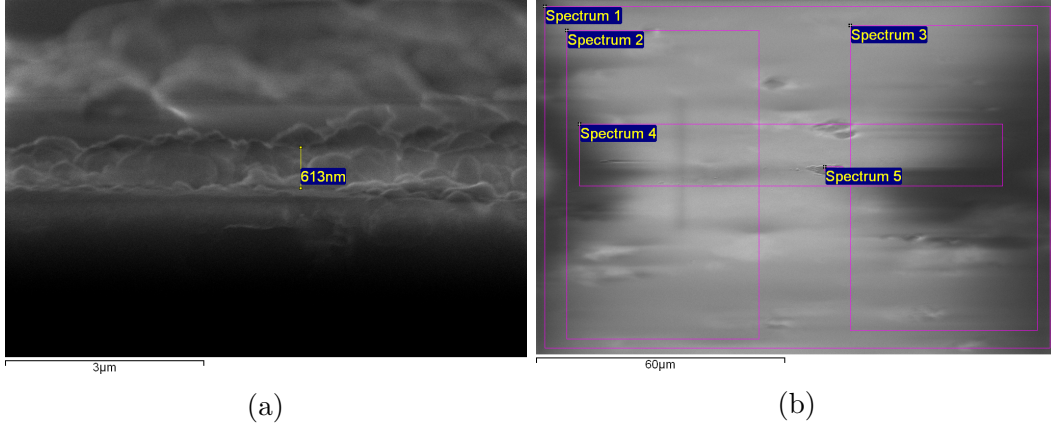
Figure 3.4: **(a)**: Side-view of the edge of the dummy sample; its thickness estimations is highlighted. **(b)**: Top-view of a central region of the dummy sample; the subregions investigated to determine the chemical $at.\%$ ratios are indicated by the yellow rectangles.

Spectrum #	O [%]	Ti [%]	V [%]	V/Ti [%]
Spectrum 1	70.77	17.63	1.69	**8.74**
Spectrum 2	71.33	17.59	1.51	**7.91**
Spectrum 3	68.39	19.7	1.61	**7.56**
Spectrum 4	71.96	16.86	1.64	**8.86**
Spectrum 5	71.84	17.46	1.26	**6.73**

Table 3.1: *Atomic*% of the main elements of the dummy sample; *spectrum* regions are the one shown in Figure 3.4b. The significant column is the **bold** one; Ti was chosen as reference rather than O due to the presence of the latter in the glass substrate too. Values are in agreement with the expected 8% V content; it must also be considered that the wider spectra regions give more reliable figures overall, while the smaller ones provide insight in local deviations. The elements measured but not shown because non-significant are Si, Na, Ca, K, which all belong to the substrate glass.

19

(a)   (b)
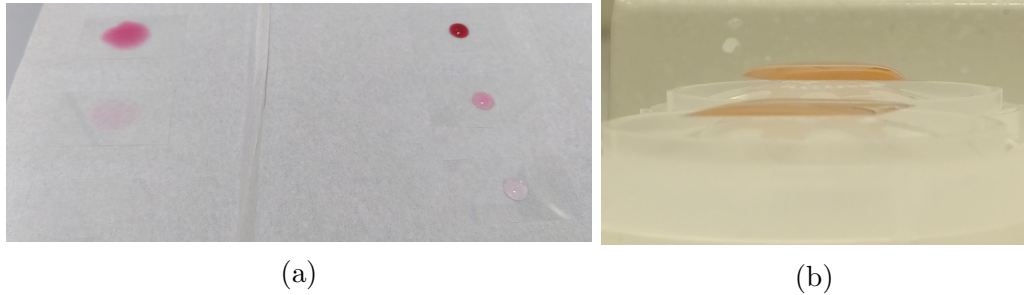
Figure 3.5: **(a)**: $50\mu L$ of various nanoparticle solutions deposited on glass coverslips; on the right, glasses were cleaned with acetone and methanol, then rinsed with *Milli-Q* water and blown dry with a N_2 gun; glasses on the left, after this treatment were plasma cleaned with the procedure explained in this section. **(b)**: Closeup of a $200\mu L$ deposition of $100nm$ Au nanoparticle solution on two "training" samples; the foreground sample was plasma cleaned while the one in the background was only blown with a N_2 gun. The wider spread of nanoparticle solution in the plasma cleaned samples is clearly visible in both images; in fact, in (a) the bottom left solution is so spread to be almost non-visible.

oven, or even organic residues caused by handling. An efficient way of removing such contaminants is the *plasma cleaning* process, which also helps in polishing samples surface. It consists in a low-power version of *plasma etching*, where a low pressure plasma is used to "attack" the sample surface and mechanically remove small amounts of material, through repeated and spatially homogeneous impacts [35]. Moreover, the increased smoothness of the samples after cleaning improves their *wettability*, spreading liquid droplets on larger surfaces due to reduced solid-liquid interface energy. An example of the improved wettability is shown in Figure 3.5.

The device used in this work is a *diener Zepto* plasma cleaner [36], which is shown in Figure 3.6. This instrument uses a O_2 plasma excited through RF waves. Due to its high chemical reactivity, the use of *oxygen* as plasma agent should not be easily overlooked. There is in fact evidence of damages to the cleaned materials if the plasma power is too high [37]. At the same time, small amount of damage at lower power is proved to enhance the optical properties of surfaces [38].

Taking into consideration literature evidence, the following cleaning routine was devised:

– samples are blown with a N_2 gun to remove dust and other particles, then placed in the plasma chamber;

Figure 3.6: **(a)**: The *diener Zepto* plasma cleaner used. **(b)** Closeup of the plasma chamber while performing a cleaning routine on a batch of samples.

- a pressure $< 0.25mbar$ is enforced in the chamber before supplying O_2 @$1.25scfh$, which ensures a plasma pressure $\approx 2mbar$;

- plasma is turned on with a RF power of $20W$ @$40kHz$ and maintained for $1min$;

- plasma and O_2 supply are turned off, and a pressure $< 0.25mbar$ is enforced before removing the samples, to allow floating debris to be sucked away from the chamber.

3.2   X-Ray Characterisation of Thin Films

X-Rays are powerful tools for many investigations concerning the structure of matter. In the study performed in this thesis, it is of paramount importance to know in detail both the crystalline structure and thickness of the samples deposited. *X-Ray Diffraction* (*XRD*) and *X-Ray Reflection* (*XRR*) are two techniques that can obtain such informations without actually damaging the samples [39].
All XRD & XRR measurements done for this thesis were performed with the same instrument, a *Brucker D8 ADVANCE eco* in the following configuration:

- $Cu : K_\alpha$ source ($8.04keV$, 1.5406Å);

- Göbel mirrors & $0.6mm$ slit on the source;

- Söller 0.2^o collimator on the detector;

- $0D$ acquisition mode.

The instrument was provided with a proprietary software (*DIFFRAC.EVA*) to interface with the instrument and perform basic data analysis [40].

Finally, on a general consideration, it must be noted that the quality of X-Ray measurements is strictly correlated to the smoothness of the samples surface. Rough interfaces might randomly scatter the incident photons and thus reduce the measurement accuracy, thus sample smoothness is a main necessity.

3.2.1 X-Ray Diffraction (XRD)

XRD allows to investigate the crystalline structure of materials in many different configurations [39].

The measurements performed were done with a 2θ configuration at a grazing incident angle of 1°. Data analysis was carried out with the *DIFFRAC.EVA* software, taking advantage of its built-in database to find diffraction patterns corresponding to the measured ones.

3.2.2 X-Ray Reflection (XRR)

XRR exploits a modified and more accurate variant of *Bragg law* (2.1) to determine the thickness of multilayers composed of k nano-layers [41].

$$\sin^2\theta_m = \left(\frac{\lambda}{2\Lambda}\right)^2 m^2 + 2\delta \tag{3.1}$$

is known as *modified Bragg law*; θ_m is the photon incident angle, λ its wavelength, m is a positive integer, and

$$\Lambda = \sum_{i=1}^{k} d_i \tag{3.2}$$

$$\delta = \frac{\sum_{i=1}^{k} d_i \delta_i}{\Lambda} \tag{3.3}$$

are respectively the *modulation period* of the multilayer (its total thickness) and its average refraction index, considering the *X-ray approximation* where $n = 1 - \delta$. A graphical description of the elements involved in (3.1), (3.2), (3.3) is shown in Figure 3.7. The reflection spectra measured can then be fitted to this or similar models to extract the d_i thickness of each single nano-layer.

A $\theta - 2\theta$ configuration of the instrument was chosen for these measurements, while spectra fitting was performed using the *GenX* software [42], which relies on the *Henke* database [43] to model the layers properties.

Figure 3.7: Schematic showing X-ray refractions and reflections at nano-layered multilayer surface and layer interfaces. ***From:*** Q. Yang and L. Zhao, *Figure 1*, [41].

3.3 Ellipsometry Analysis

Ellipsometry is an optical technique for investigating the dielectric properties of thin films (thickness, complex refractive index/dielectric function). Its name, first used in 1945, comes from the fact that it is a form of spectroscopy performed exploiting *elliptical polarisation* of light [44]. As with any other spectroscopic technique, it can be performed in reflection, absorption, scattering, or transmission configuration, though the first one is the most commonly used.

If one of the analysed thin film property is known (thickness or refractive index/dielectric function), mathematical models can be used to fit the remaining ones. This makes ellipsometry an extremely powerful tool in determining thickness and/or optical constants of films of all kinds in a non destructive and precise way [45, 46].

3.3.1 Refractive Index Determination

Knowing the complex refractive index of the samples prepared in this thesis is of paramount importance if any computational simulation regarding them is to be performed. As no database entry could be found in literature for V-doped TiO_2 [47], a direct measurement of the indices of the samples had to be

23

Figure 3.8: Experimental setup for an ellipsometry experiment. **_From:_** Buntgarn, [48].

performed.

The ellipsometer used is a _J.A. Woollam Co. M-2000FI_ coupled with a _ESM-300_ automated horizontal angle source and detector, and an _EC-400_ DAQ. Measurements were performed in reflection configuration (see Figure 3.8), at a fixed angle of 20°. This was done on the basis of previous experience, even though performing the same measurement at different angles usually results in better data quality [45].

The _ESM-300_ source projects a linearly polarised beam of light in the $UVA-VIS-NIR$ range onto the sample. As the incident light interacts with it, the polarisation of the reflected beam is inevitably changed, and results elliptically polarised [49]. What the _ESM-300_ detector actually measure is in fact the _ellipsometric ratio_ [50]

$$\rho = \frac{r_p}{r_s} \equiv \tan \Psi e^{i\Delta} \tag{3.4}$$

where r_p and r_s are respectively the p and s component of the reflected, elliptically polarised light, as represented in Figure 3.9; thus $\tan \Psi$ is the amplitude ratio upon reflection and Δ is the phase shift of the light beam.

As already stated for X-Ray techniques in Section 3.2, the superficial roughness of the samples should be as low as possible, to reduce light loss and distortion from undesired random scattering. Moreover, as the objective of the ellipsometry measurements in this thesis is to obtain the refractive index of the samples, a precise knowledge of their thickness obtained through XRR (Section 3.2.2) is required before any modelling is performed.
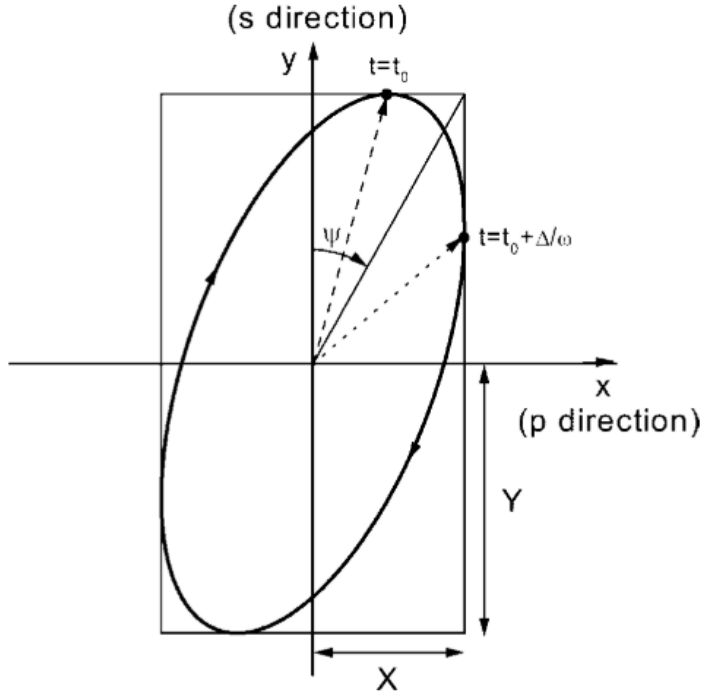
Figure 3.9: The ellipse of polarization and its parameters. ***From:*** J. Humlíček, *Figure 1.3*, [49].

3.3.2 Fitting Models

The main scope of the models used in fitting ellipsometry data is to accurately describe the behaviour of the materials in the multilayer making up the sample when interacting with incident light. Different materials are better represented by different models, and the multilayer making up a sample can be described by a variety of layers each modelled differently.
Data analysis on the measured samples was performed with the help of the dedicated software *CompleteEASE*®, which provides a wide variety of models [45]. The ones chosen to be used in this work are now listed.

– **Cauchy:** This model is commonly used for fully or partially transparent layers such dielectrics at energies below their fundamental bandgap; their refractive index is represented by a function that varies slowly with the wavelength, and exponential *Urbach tails*. The analytical expressions of the real and imaginary component of the index are the following:

$$n(\lambda) = A + \frac{B}{\lambda^2} + \frac{C}{\lambda^4} \tag{3.5}$$

$$k(E) = k_{amp}e^{E-E_{gap}} \tag{3.6}$$

where A, B, C, k_{amp} and E_{gap} are all fit parameters of the model

- **Tauc-Lorentz:** In this model the dispersion function of a layer describes the main absorption of the material as a broad Lorentzian lineshape, with zero absorption below a defined bandgap energy. For energies slightly larger than the gap value, the following law is used:

$$\epsilon_2(E) = \propto \frac{(E - E_{gap})^2}{E^2} \tag{3.7}$$

where E_{gap} is the only parameter other than the 3 describing the Lorentzian peak: E_0 the peak centre, A a peak amplitude factor, B a peak width factor.

- **Cody-Lorentz:** This model is extremely similar to the *Tauc-Lorentz*, with the exceptions that instead of (3.7) it uses

$$\epsilon_2(E) = \propto (E - E_{gap})^2 \tag{3.8}$$

and that it also includes an *Urbach* term to model absorption at energies below E_{gap}. So, other than the same parameters of *Cody-Lorentz*, this model has 3 more: U for the tail amplitude, E_p indicating where absorption changes from Lorentzian to Cody behaviour, E_t indicating where the absorption transitions from Cody to Urbach behaviour; a graphical representation of the meaning of the last two terms is shown in Figure 3.10.

3.4 UV-VIS-NIR Spectroscopy

The main goal of this thesis work, is to obtain meaningful information from the transmission and reflection spectra of the samples prepared. The instrument used to perform all measurements was a *Perkin Elmer UV/VIS/NIR Spectrometer "Lambda 1050"* with a *tungsten-halogen* lamp, which can provide a reliable intensity in the $NIR - VIS$ range and in the UV until $\approx 300nm$. The detector module used was however different for the transmission and reflection measurements, the latter one being done with an integrating sphere which, from previous experimental knowledge, was known to be less reliable in measuring transmission spectra.

Finally, it must be pointed out that, in order to achieve any meaningful insight
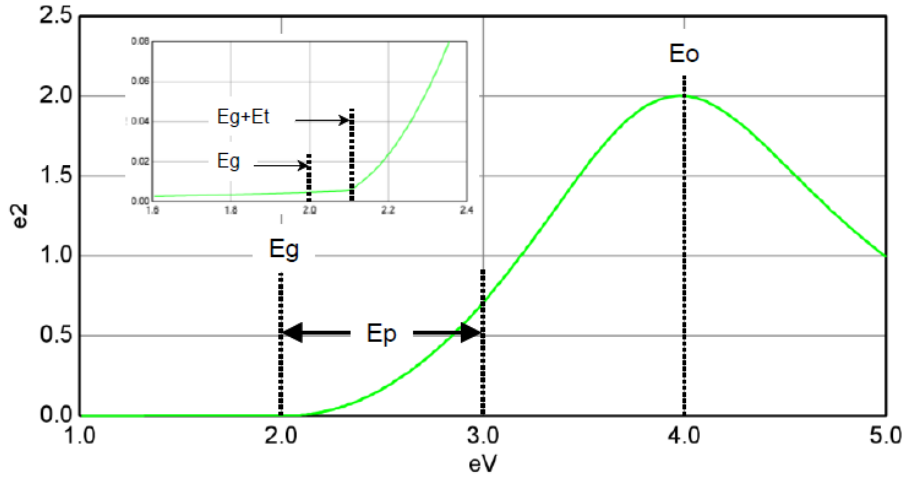
Figure 3.10: Parameter definitions for the Cody-Lorentz oscillator in *CompleteEASE®*. **From:** J. A. Woollam Co., *Figure 10-2.*, [45].

of the interaction between the deposited samples and the plasmonic nanoparticles, separate measurements had to be performed: with and without the particles deposited on the samples, and the spectrum of the nanoparticles before being deposited must also be known. Different datasets were then organised, as once the particles were deposited it would have not been possible to measure the "bare" samples again.

3.4.1 Transmission Spectra Module

The transmission spectra were measured with the *Perkin Elmer UV/VIS/NIR Accessory "3D WB Detector Module"*, using its *InGaAs* detector to scan in the range $810 \div 320 nm$. Before each dataset was measured, the detector was calibrated at 100% &0% transmitted light.

To improve data quality, all the measurements on the samples were performed placing them in the custom-made metallic mask shown in Figure 3.11a, whose circular opening is $\approx 2.6 mm$ in diameter. Other than allowing only the central part of the light beam to pass through, the sample holders present on the mask allow to always illuminate the same region of the samples, guaranteeing measurement consistency. The metallic mask was left in place, without any sample on, during the detector calibration too (Figure 3.11b).

To measure the transmission spectra of the nanoparticles solution, no mask was used. They were instead poured in a cuvette, which was then placed on the appropriate holder provided with the instrument.

<div align="center">(a)   (b)</div>
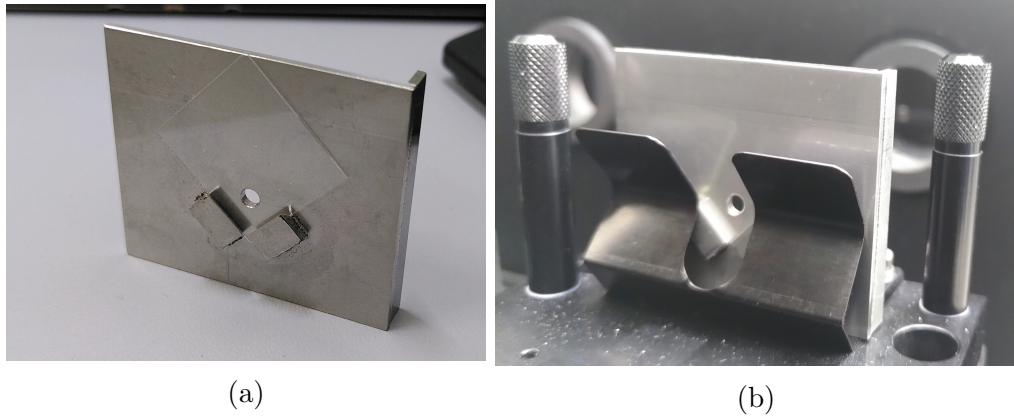
Figure 3.11: **(a)**: The metallic opaque mask used; a demonstrative glass coverslip is placed in the holder, showing how the samples could steadily and consistently be placed in the same position for different dataset measurements. **(b)**: The mask positioned inside the instrument; in the background, the openings to the measuring modules are visible.

3.4.2   Integrating Sphere Module

Reflection spectra measurements were performed with the *Perkin Elmer "150mm InGaAs Int. Sphere"*, using its *InGaAs* detector and scanning the range $810 \div 380$. The reduced spectral range compared to the transmission measurements is due to the poorer performance of the *InGaAs* detector. As for the transmission measurements, it was anyway calibrated at 100% &0% transmitted light before measuring each dataset. Calibration was performed using the same mask described in Section 3.4.1, placed in the same sample holder used for the transmission module, as in Figure 3.11b. This was done to maintain calibration consistency with the transmission measurements.

This integrating sphere (Figure 3.12) allows to perform measurements of diffracted and scattered spectra too, other than the "full-reflection" ones. However, due to the high sensitivity required in this work, only the latter could be performed. To do so, the samples were placed at the back window of the sphere as shown in Figure 3.12c, where the light would hit them at an angle of 4° before being reflected and collected by the *InGaAs* detector at the bottom of the sphere. All the other windows were kept closed, except for the reference entrance window, which do not posses a cover.

3.4.3   Sample Datasets

In order to obtain the greatest amount of information from the prepared samples, the same measurements described in this section were repeated on different dataset, formed by the same basic samples but at different stage of manipulation. Excluding the measurements performed directly on the nanoparticle solutions, three different dataset were measured in this project work:

– **"Naked" dataset:** This dataset is made of the samples simply deposited, annealed and plasma cleaned as described in Section 3.1, without any nanoparticle on them.

– **"Deposited" dataset:** This datased is obtained following this procedure, perfected after testing with the "dummy" samples, to deposit the nanoparticle solutions on the samples themselves:

   – samples are blown with a N_2 gun to remove dust, then placed in wafer-holders;

   – $200\mu L$ of nanoparticle solution are dropcasted on the samples, starting from a corner and spreading the liquid on the whole sample (Figure 3.13b);

   – samples are partially covered (Figure 3.13a) and left to dry at room temperature for $\approx 4h$ (Figure 3.13c);

   – samples are moved in a fumehood and, still partly covered and at room temperature, left to finish drying for $\approx 2h$ (Figure 3.13d).

The drying process diversification is due to the fact that a slow drying process is necessary to reduce "coffee stains" effect, but a too slow process might cause the nanoparticles still in solution to excessively cluster together.

– **"Washed" dataset:** This final dataset is obtained from the *deposited* one after the samples are quickly immersed in Milli-Q water and gently shaken; this is done in order to dissolve away the nanoparticle clusters, while keeping attached to the TiO_2 the more isolated ones.

A final definition for transmission measurements of these datasets is used to identify if the data are directly obtained from a measurement, or if the contribution to the sample transmission due to the glass substrate was subtracted from it. In the first case, the dataset is defined as "raw", while in the other it is "corrected". The *correction* is performed by algebraically subtracting the transmission spectra of a *reference glass* measured in *absorbance units* (*A.U.*) from the spectra of the samples (in *A.U.*).

3.5   Dark-field Microscopy (DF Microscopy)

Dark-field (DF) microscopy is an optical microscopy method in which only the light scattered by the studied sample is collected and observed [51]. There are many different configuration that can provide this outcome [52], though the fundamental idea is that the light used to illuminate the sample is directed away from the detecting optics, as for example shown in the schematics in Figure 3.14a. Besides from the fact that, contrary to regular optical microscopy, the background of the observed image is black, DF microscopy is an powerful tool in studying (or simply seeing) items whose scattered light carries an important information. This technique is in fact useful to actually see single nanoparticles or their clusters, and if a light source powerful enough is available, it is also possible to perform spectrography measurements solely of their scattered light [54].

In this thesis, DF microscopy has been used to visually analyse the nanoparticles dropcasted on the TiO_2 films and evaluate the quality of their deposition. The instrument used is made of the following components:

- *Zeiss Axio Observer 7 materials* microscope, with 1.6x internal magnification and 10x objective;

- *Thorlabs MLS203P2* sample holder, driven by a *Thorlabs BBD202* and relative software;

- *Zeiss Axiocam 105 color*, 2.2*μm pixels* camera, for image exporting in RGB format.

Due to the low intensity of the light source used, and instrumental issues in the white balancing of the camera, no spectrographic analysis could have been performed. Moreover, due to the excessively small size of the prepared samples, the custom made cardboard mask shown in Figure 3.14b,3.14c had to be used; this unfortunately prevented the use of 50x optics.
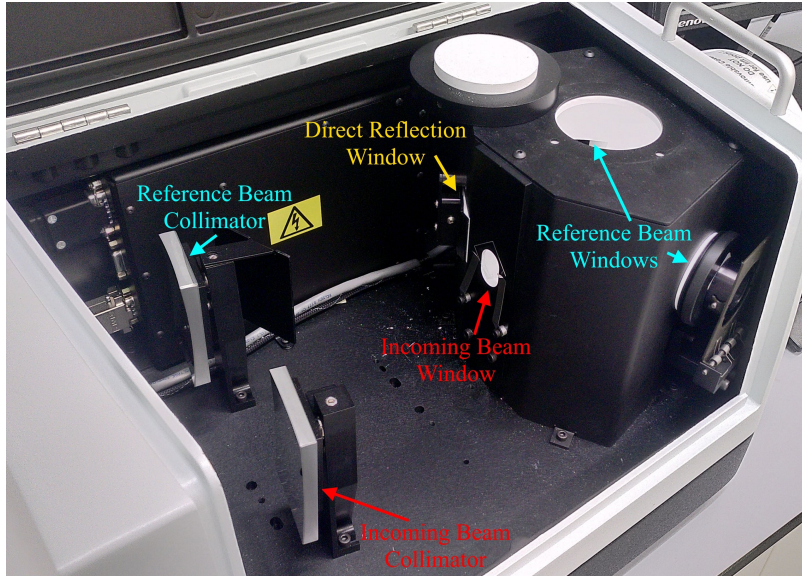
(a)
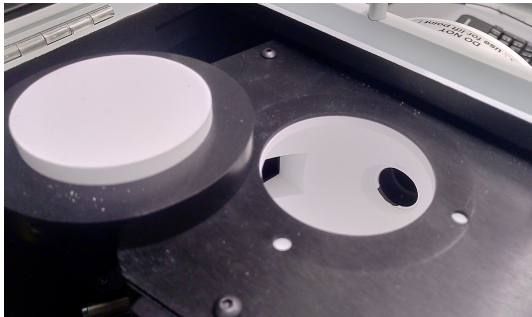
(b)
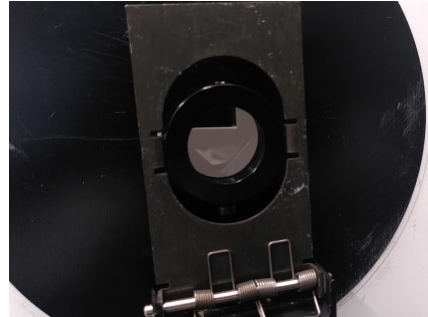
(c)

Figure 3.12: **(a)**: The integrating sphere module open, with its main features highlighted and the top cover of the sphere removed; a demonstrative glass coverslip is put in front of the entrance window as it would be done to perform a transmission measurement (which in the end were not done). **(b)** Closeup of the interior of the integrating sphere; on the left the entrance window for the reference beam, while on the right the transmitted light exit window, are clearly visible. **(b)**: Closeup of a demonstrative glass coverslip placed at the transmitted light exit window, showing how the samples are placed to perform reflection measurements.
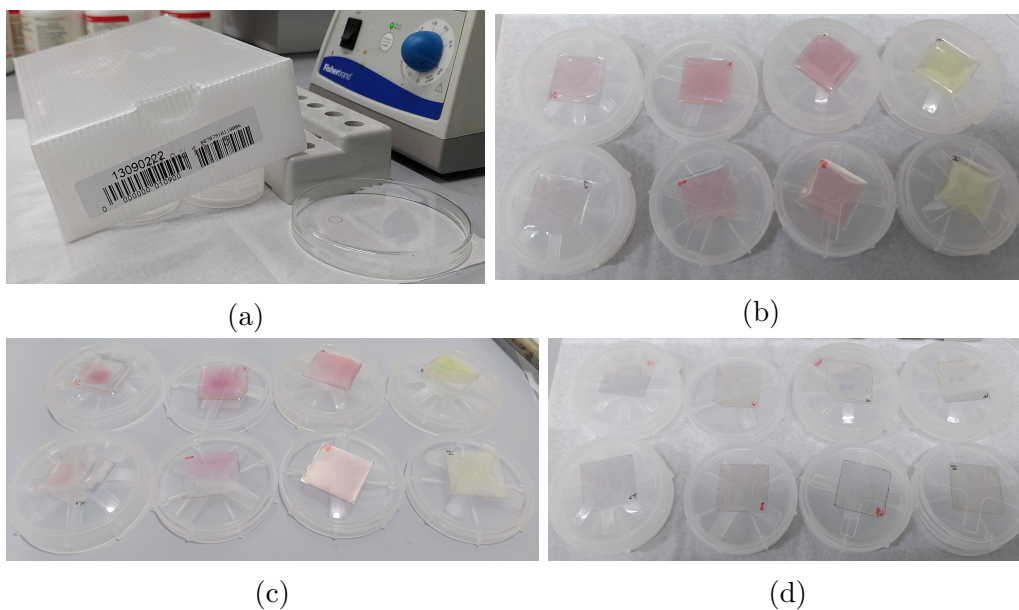
Figure 3.13: **(a)**: Drying setup; the samples are placed under the partially raised box, in order to allow some airflow. **(b)**: Dummy samples immediately after the nanoparticle solution dropcasting. **(c)**: Same samples as *(b)* after $\approx 3h$ of RT drying; most of them are still significantly wet and need some more drying-time. **(d)**: Same samples of *(c)* after another $\approx 1h$ drying in air, and a final $\approx 2h$ drying session in the fumehood; no liquid remains present.
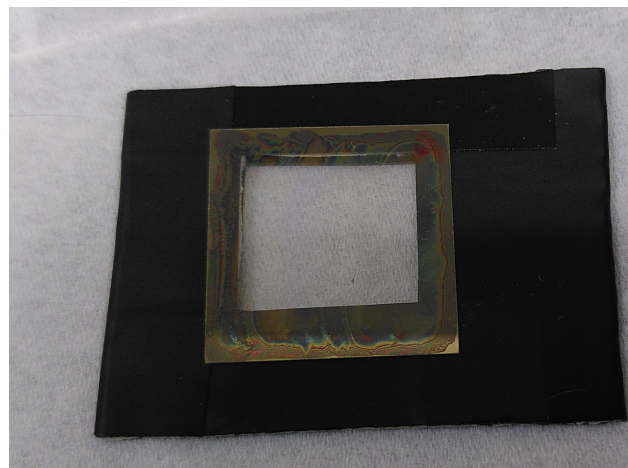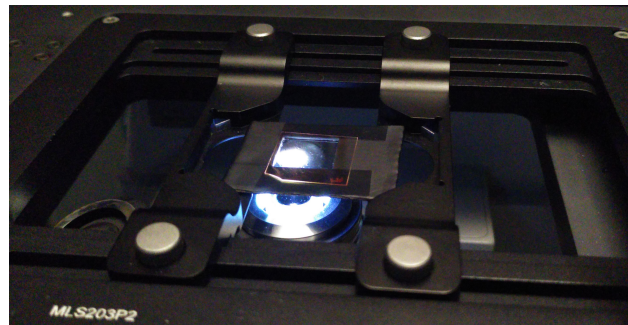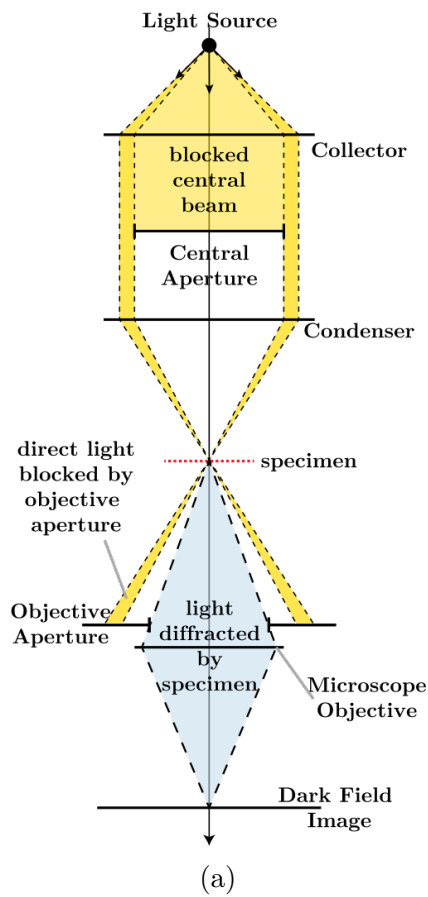
Figure 3.14: **(a)**: Diagram illustrating the light path through a generic dark-field microscope. Notice how the direct light (dark yellow path) is driven outside of the objective. **_From:_** R0oland, [53]. **(b)**: A demonstrative sample placed on the cardboard mask onto the sample holder of the DF microscope; in this instrument both le light source and the objective are placed under the sample, so that no direct light can be observed. **(c)**: Closeup of the cardboard holder, with a demonstrative sample placed on it.

4 - Results

In this chapter the experimental results obtained on the samples prepared, analysed using the techniques described in Chapter 3 are discussed. When necessary, further explanation concerning the adopted methodologies is provided. The scope of this chapter is mainly declarative, so insights and speculation on specific arguments are present, though the bulk of data interpretation is left to the concluding Chapter 5.

The order in which the results are presented is not a chronological representation of the work done. It was instead chosen to better guide the reader through the experimental work performed, in the most gradual, clear and linear fashion possible.

4.1 Sample Labels

A total of 8 samples were produced as described in Section 3.1 to be studied, plus another batch of 8 "dummy" samples. The latter ones were used only to practice the experimental procedures, in particular for testing the non-damaging effects of plasma cleaning (Section 3.1.3) and in devising the drop-casting procedure of nanoparticle solutions (Section 3.4.3).

Of the used samples, the 4 doped at 8% V are labelled A through D, while the *undoped* samples have labels from M to P. The in-between letters (E through L) were used for the *dummy* samples, whose doping level is uncertain, but lying in the $2 \div 4\%$ V according to previous experiences of the sputterer as stated in Section 3.1.1.

Table 4.1 provides a simple visualisation of the 8 samples prepared.

4.2 Refractive Indices Determination

The first step before proceeding to any analysis of the physical or optical properties of the samples is to determine their refractive indices. That is because this information is fundamental to perform any other modelling of the samples

Sample	V-doping [at.%]		Sample	V-doping [at.%]
A	≈ 8%		M	0%
B	≈ 8%		N	0%
C	≈ 8%		O	0%
D	≈ 8%		P	0%

Table 4.1: Doping levels of the 8 samples studied in this project.

behaviour, as discussed for XRR in Section 3.2.2, or to simulate their optical properties and interaction with the NPs.

To do so, it is necessary to perform an *ellipsometric analysis* on all samples as described in Section 3.3. The most reliable fits for the 8% V and 0% V samples are then chosen, and used to obtain an accurate refractive index for both doping levels.

4.2.1 Model Fittings

As a first guess for the samples thickness, the expected value of $50nm$ was used. It was kept as a fitting parameter, as it was not known for certain. First of all, the 4 *undoped* samples are fitted to all the three models described in Section 3.3.2, in order to find the least accurate one and discard it immediately. The fitting results are shown in Table 4.2.

The first noticeable feature emerging from the fits is that the thickness obtained is significantly different from the expected $50nm$, a finding that will later be corroborated by XRR and optical fittings in Section 4.3.2. Secondly it is clear that none of the models could achieve a solid fit, with the lowest *MSE* being as high as 4.312. Finally, it is clear that the *Tauc-Lorentz* model is the worse than the *Cauchy* and *Cody-Lorentz*, and discarded from the fittings of the *doped* samples. Their fit results are shown in Table 4.3.

4.2.2 Best Refractive Indices Determination

After fitting all samples, the *Cauchy* model has the best *MSE* in 5 out of 8 samples, averaging it at 7.254, versus the 8.093 of *Cody-Lorentz*. But it must also be noted that the latter one scores the absolute lowest *MSE* for both doped and undoped samples, and the average *MSE* values are not dramatically different. Moreover, if the actual fitting plots are observed it can be seen that it is the *Cody-Lorentz* model that actually provides the best fits overall.

Comparing the best fits of the *undoped* samples (Figure 4.1), graphical evidence confirms the *Cody-Lorentz* fit of sample M as the best one to obtain the

Sample	Model Used	Estimated Thickness [nm]	MSE of the Fit
M	Cauchy	69.51 ± 0.02	7.008
M	Tauc-Lorentz	71.700 ± 0.015	4.676
M	**Cody-Lorentz**	71.770 ± 0.014	**4.312**
N	**Cauchy**	73.40 ± 0.02	**6.446**
N	Tauc-Lorentz	74.69 ± 0.04	10.17
N	Cody-Lorentz	74.86 ± 0.03	6.874
O	**Cauchy**	72.80 ± 0.04	**10.561**
O	Tauc-Lorentz	73.98 ± 0.04	11.903
O	Cody-Lorentz	73.63 ± 0.04	11.021
P	**Cauchy**	74.36 ± 0.04	**6.198**
P	Tauc-Lorentz	75.39 ± 0.05	12.989
P	Cody-Lorentz	75.80 ± 0.03	8.923

Table 4.2: Ellipsometry fit results on the *undoped* samples. Bold values indicate the lowest *Mean Square Error* of the fits for the same samples.

Sample	Model Used	Estimated Thickness [nm]	MSE of the Fit
A	**Cauchy**	74.41 ± 0.02	**6.407**
A	Cody-Lorentz	75.57 ± 0.03	7.487
B	Cauchy	78.53 ± 0.03	7.361
B	**Cody-Lorentz**	78.88 ± 0.02	**4.354**
C	**Cauchy**	76.90 ± 0.02	**7.119**
C	Cody-Lorentz	77.74 ± 0.03	8.723
D	Cauchy	83.18 ± 0.03	6.929
D	**Cody-Lorentz**	83.39 ± 0.02	**4.441**

Table 4.3: Ellipsometry fit results on the *doped* samples. Bold values indicate the lowest *Mean Square Error* of the fit for the same sample.
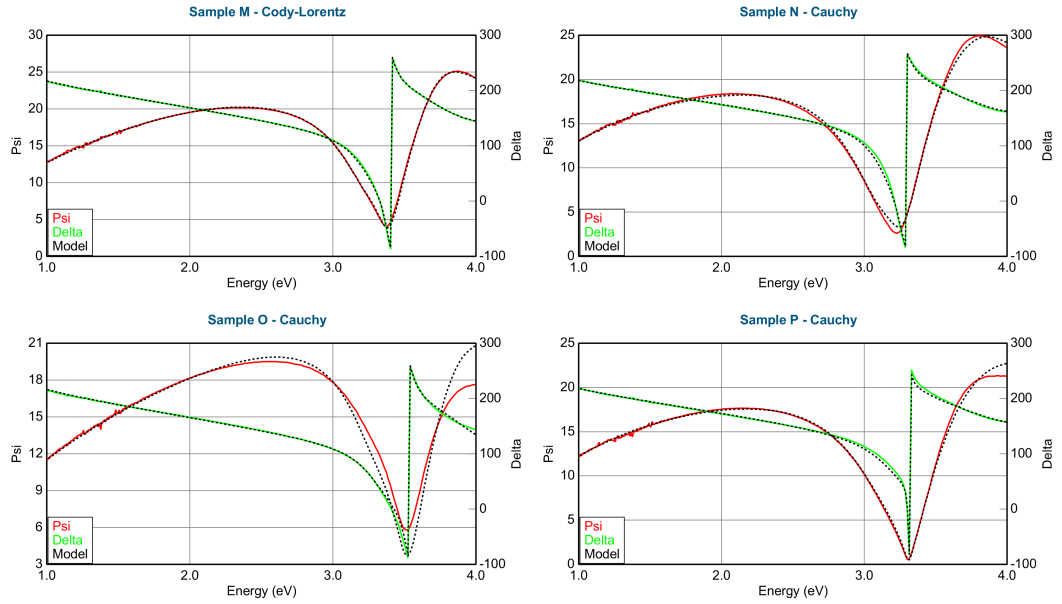
Figure 4.1: Best fits of ellipsometry data for the *undoped* samples. Coloured solid lines are the measured data of the ellipsometric values Ψ and Δ, while the dotted black lines are the result of fittings. It is clearly visible that the fit of sample M is the most accurate one.

refractive index of the 0% $V : TiO_2$. Focusing on the *doped* samples on the other hand gives less intuitive results. Observing their best fits (Figure 4.2) it is possible to see that none is able to properly model the ellipsometry data. The discrepancies are more emphasised near the sharp features of the plots, which should be near the bandgap of the samples and play a key role in modelling that spectral region. More generally, the *MSE* values of the *Cody-Lorentz* model are lower than *Cauchy*, indicating better fits overall. This prompts to look at the two missing *Cody-Lorentz* fits (Figure 4.3). Here it can be seen that sample A shows the best agreement with the data in the previously mentioned sharp features of the plot among the *Cody-Lorentz* fits, and was thus chosen as best one.

In conclusion, the two samples used to determine the complex refractive index of the 0% V and 8% V samples are, respectively, M and A. The decision was taken considering fit quality, and to have consistency in the values obtained, as in this way the two indices are determined using the same mathematical model: the *Cody-Lorentz* one. However, the fit quality is not fully satisfactory, and further improvements are needed to achieve better reliability.
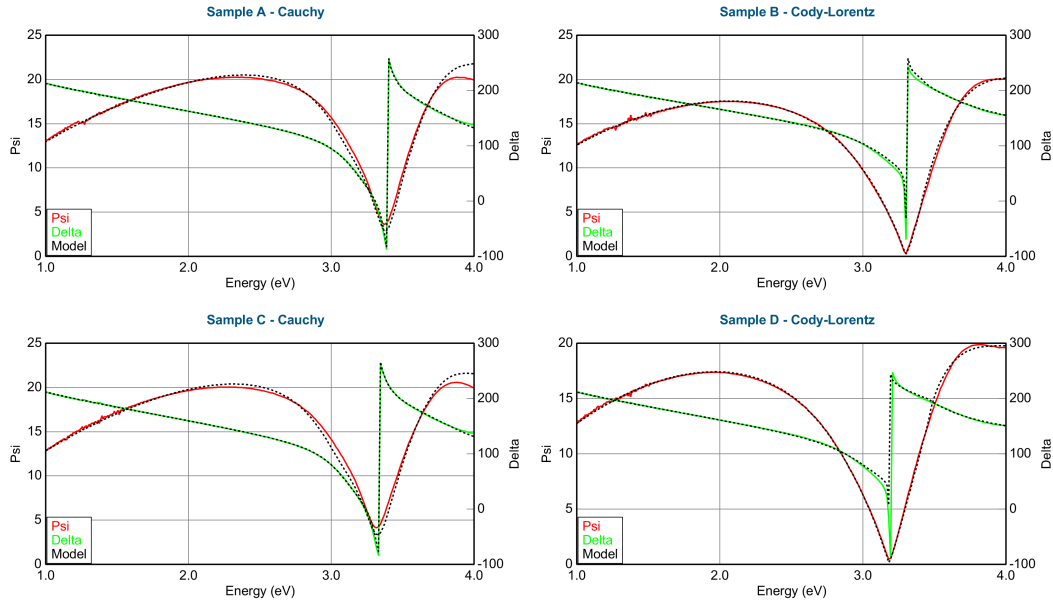
Figure 4.2: Best fits of ellipsometry data for the *doped* samples. Coloured solid lines are the measured data of the ellipsometric values Ψ and Δ, while the dotted black lines are the result of fittings. No-fit agreement as good as for sample M is present, as the *Cauchy* fits lack precision in the Ψ values, while *Cody-Lorentz* does in the Δ ones.
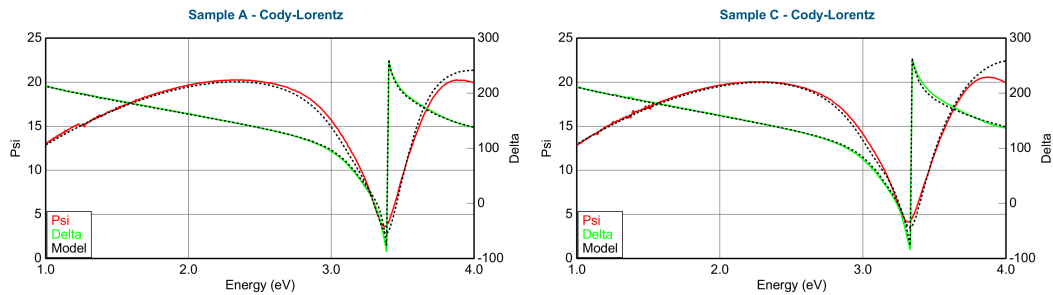
Figure 4.3: *Cody-Lorentz* fits of ellipsometry data for the remaining *doped* samples. Coloured solid lines are the measured data of the ellipsometric values Ψ and Δ, while the dotted black lines are the result of fittings. Both fits are not perfect, but A provides the best deal for achieving maximum accuracy in the region close to the sharp features of the measured data. the qualitative difference with D is extremely low.

4.3 Physical Characterisation of the Samples

After the refractive index of the samples is known, it is possible to proceed to characterise their physical properties, such as crystalline phase and thickness. The first goal was achieved using the XRD technique described in Section 3.2.1. Thickness estimation of the samples, on the other hand proved to be a rather complex task. First estimations of the thicknesses were performed with the XRR technique of Section 3.2.2.

However, looking at the transmission spectra of the *bare* dataset (which will further be discussed in Section 4.6), unphysical points of "negative absorbance" were found. This is attributable to instrumental or operative errors, which inevitably corrupt any data analysis. Thus, with the help of transmission spectra simulated using the *Optical* software [11], a common point to all the spectra was found to which shift all the data. This way all unphysical points were corrected, and more reliable values for samples thickness were obtained.

4.3.1 Crystalline Phase Determination

XRD measurements were performed and analysed as described in Section 3.2 and specifically Section 3.2.1. From the samples spectra gathered in Appendix A.1, it is clearly visible that all samples have the characteristic lines of the *anatase* phase of TiO_2. The lines for metallic V were also searched, to check if the dopant had assembled into significantly wide grains. As no line is clearly visible, this situation can be excluded and V can be considered "diluted" in the *anatase* matrix.

4.3.2 XRR Thickness Estimation

Following the procedures described in Section 3.2 and specifically Section 3.2.1, XRR measurements were performed on the samples, and subsequently analysed with the *GenX* software [42]. The fits required only to state the crystalline phase and density of the film studied: the value of $3.9g/cm^3$ [55]. The *Figure Of Merit* (*FOM*) used to determine the fit validity was the average of the absolute difference between the base10-logarithms of the data and the simulation. The software also provided an estimation of the samples surface roughness, and the results obtained are reported in Table 4.4.

The values obtained are in agreement with the ones showed in Table 4.2 and Table 4.3, suggesting that the calibration of the deposition times of the sputterer used (Section 3.1.1) should be adjusted.

4.3.3   Spectra Shifting & Optical Thickness Estimation

Looking at the *corrected* transmission spectra of the *bare* samples (Section 3.4.3 for the definitions, while a more thorough discussion will be done in Section 4.6.2) it is easily visible that some undoped samples show unphysical behaviour. In particular, as shown in Figure 4.4, some points result having negative *absorbance*, which is not possible: if true it would mean that the samples are emitting more light than they are receiving, producing it out of nowhere. This is in fact probably due to imperfect calibration of the instrument and/or small errors in samples placement.

To correct these unphysical features, both the transmission and reflection spectra of the *raw bare* samples were fitted using the *Optical* software with the refractive indices found in Section 4.2.2, searching for common points at energies $< 2eV$ in the spectra. This was done because at those energies light should not interact with the samples, as both their bandgap and the expected V states are above that value, thus leaving the spectra to be determined only by thin film interference effects (Section 2.1.3). Simulations results for transmission are shown in Figure 4.5, where the average intersection points for the two different doping level sample sets is also indicated. For the full range of the simulations see Appendix A.2.

The next step performed was to shift all the *raw bare* spectra in such a way that they would intersect those points. Then the *raw deposited* and *washed* dataset were shifted in such a way that their lowest energy points would coincide with the *raw bare* dataset values (see Section 3.4.3 for the meaning of dataset names). This was done to eliminate other instrumental or placement errors, as at those energies no deposited nanoparticle should absorb light in a significant way (see Section 4.5), and thus the samples behaviour should be the same. Only after this shift the glass contribution was subtracted, and no unphysical behaviour is now present as shown in Figure 4.6.

After all data have been shifted, a new simulations with *Optical* was performed in order to estimate even more accurately the samples thickness. The data obtained from those fits is summarised in Table 4.5. The values obtained are in agreement with XRR ones reported in Table 4.4, and are considered the best estimate of the actual samples thickness as the χ^2 values are more reliable than the FOM obtained in XRR fitting.

4.4   Samples Bandgap Measurement

After determining the samples physical characteristics, shifting their spectra to compensate instrumental errors and subtracting the glass substrate contri-

Sample	XRR Thickness [nm]	XRR Roughness [nm]	FOM Value
A	78.2	1.8	0.192
B	86.7	2.5	0.183
C	80.3	2.1	0.229
D	80.4	2.5	0.254
M	62.7	4	0.223
N	81.2	1.1	0.220
O	73.9	1.5	0.295
P	82.4	1.1	0.209

Table 4.4: Result of the fittings of the XRR spectra measured, using the *GenX* software. The first four samples are the *doped* ones, the last ones are the *undoped*. It must be noted that the *GenX* documentation indicates a fit as "good" if its *FOV* is $\lesssim 10^{-1}$, thus all the fits calculated are at the limit of reliability.
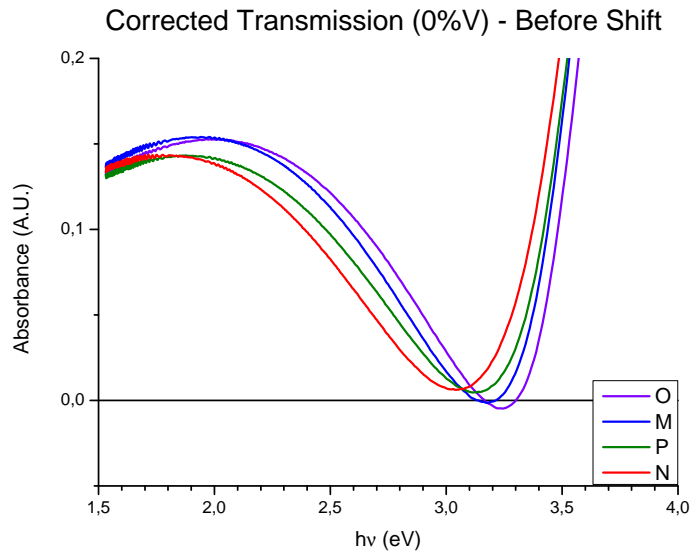
Figure 4.4: Transmission spectra, in *absorbance units*, of the *raw bare* undoped samples. The interference fringe appearing below $\approx 3.25 eV$ is clearly visible, and also that the spectra of sample O and M cross the X-axis reaching negative and unphysical values.
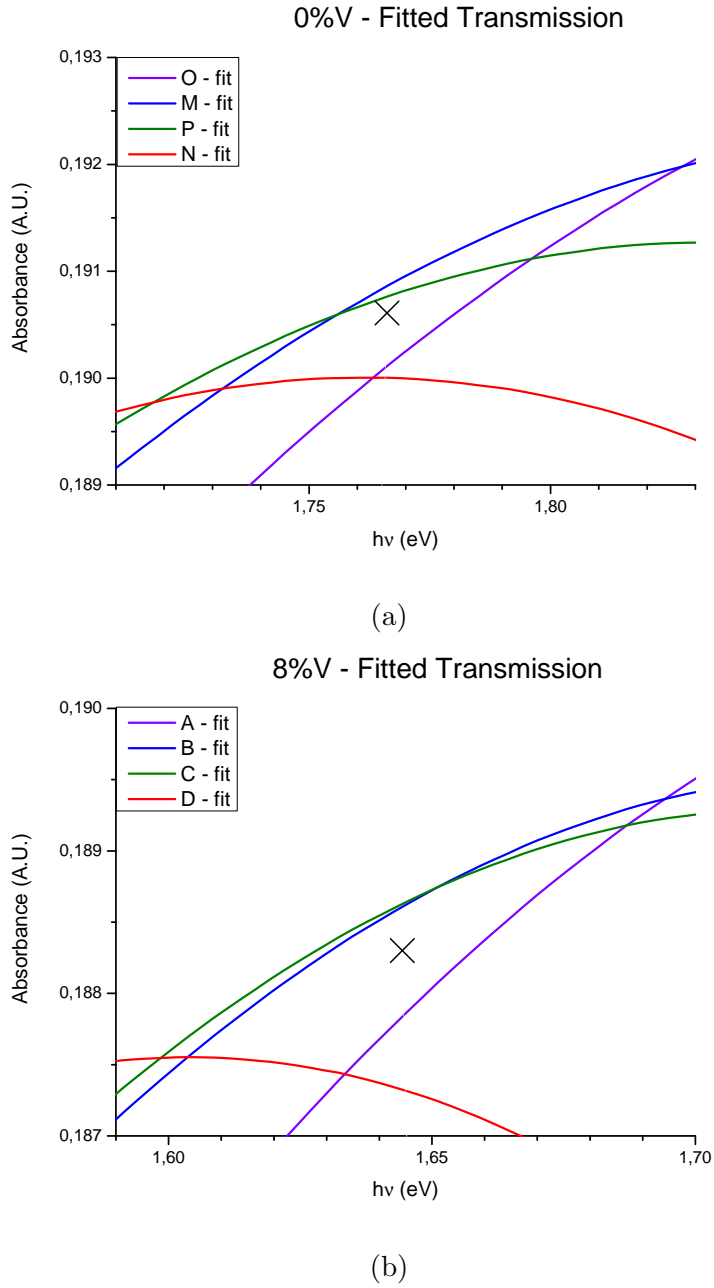
Figure 4.5: Closeups on the near-intersection regions of the simulated *raw bare* transmission spectra for **(a)** undoped and **(b)** doped samples. The cross is the average position of all the intersections between the various spectra. The full range of the simulations is in Appendix A.2.
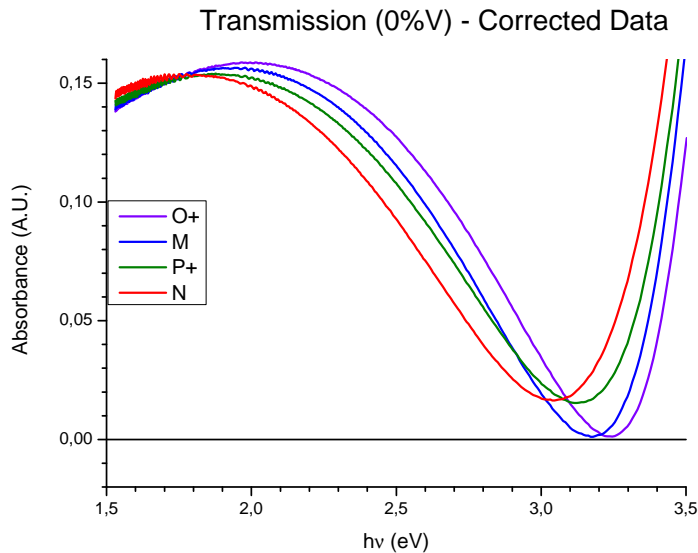
Figure 4.6: Transmission spectra, in *absorbance units*, of the *shifted bare* un-doped samples. The interference fringe appearing below $\approx 3.25eV$ is clearly visible and, contrary to Figure 4.4, no sample crosses the X-axis reaching negative and unphysical values.

Sample	V Doping Level $[at.\%]$	*Optical* Thickness $[nm]$	χ^2
A	$\approx 8\%$	75.2	4.752
B	$\approx 8\%$	77.4	7.094
C	$\approx 8\%$	78.8	8.523
D	$\approx 8\%$	83.5	11.99
M	0%	72.0	3.303
N	0%	76.3	3.838
O	0%	69.5	2.619
P	0%	73.4	3.536

Table 4.5: Result of the fittings of the *shifted bare* transmission spectra measured, using the *Optical* software.

bution to transmission measurements, a study on the optical properties of the samples can be performed. Such study is mainly focused on the determination of the bandgap values both for the doped and undoped samples. The dataset that will be analysed are the *shifted bare* ones.

To determine the bandgap values, two different methods were used: the *Tauc-plots* and the *Cody-plots*. Both are analysis devices widely known in literature, and used to determine the bandgap value of dielectrics. The difference between the two comes down to the fact that the first is based on the constant momentum matrix approximation, which leads to the functional dependence [56]

$$\sqrt{\alpha h\nu} \propto (h\nu - E_{gap}) \tag{4.1}$$

whereas the latter is based on a constant dipole matrix approximation leading to

$$\sqrt{\alpha/h\nu} \propto (h\nu - E_{gap}) \tag{4.2}$$

In both equations α is the *absorption coefficient* of the material, E_{gap} its bandgap, and $h\nu$ the energy of the incident photons. Among the two methods, *Tauc-plots* is the most used, though recent literature pointed out that *Cody-plots* can be more appropriate to thin film measurements as they were found to be less sensitive to artefacts arising from the thin film interference [57, 58]. After comparing the two methods and found the most appropriate one, the bandgap values of the samples were identified.

4.4.1 Tauc-plots vs Cody-plots

In order to "build" *Tauc-* and *Cody-plots*, the *absorption coefficient* of the samples must be known as the wavelength of the incident light varies. The soundest way of doing this is with the imaginary part of the complex refractive index k, using the well known:

$$\alpha(\lambda) = \frac{4\pi}{\lambda} k(\lambda) \tag{4.3}$$

However, due to the not-complete reliability of the refractive indices measured (Section 4.2.2), α was obtained from the *absorbance* measurements of the transmission spectra:

$$\alpha \simeq 2.30259 \frac{A}{d} \quad [m^{-1}] \tag{4.4}$$

where A is the *absorbance* and d the sample thickness. The mathematical explanation of (4.4) can be found in Appendix B.

Using (4.4) all the transmission spectra were converted and the *Tauc-* and *Cody-plots* realised. From there, to obtain the bandgap values a linear fit have

45

to be performed in the rising region of the plots, and the intercept of the fit with the X-axis is the bandgap value [56]–[58]. But here some issues arise, as the optimal region to perform the fit is not known. A MATLAB script was developed, to find such regions for every samples; its source code is reported in Appendix C.1, and the fits performed following the boundary it provided are reported in Appendix A.3. Moreover, another script was developed, reported in Appendix C.2, which finds the "best-linear-fit region" with the condition of starting it from the highest energy points of the plots; the resulting fits are in Appendix A.3. This second script was done because it was anticipated that the best-linear-region overall might be in a place where thin film interference effects are present, which would corrupt the fit.

In fact, the comparison of the resulting bandgaps reported in Figure 4.7, shows clear trends between bandgap value and sample thickness in all the fitting procedures, except for the *Tauc- plots* fitted at *high energies*. This can be explained by the fact that the "best-linear-fit region", and the spectral regions below $3.5 \div 3.6 eV$ in general, lie where a "bulge" in the spectra is caused by thin film interference and thickness-dependant, as also stated in literature [4, 58]. The *Tauc-plot* fits performed at *high energy* ranges (Figure A.12) are thus the most reliable ones.

4.4.2 Samples Bandgap Values

As stated above, the best results for the samples bandgap determination was achieved with the *Tauc-plots* fitted at *high energies*. The values obtained are graphically represented in Figure 4.8, and numerically tabulated in Table 4.6. The average value for the undoped samples is $(3.277 \pm 0.011)eV$, in perfect agreement with literature as reported in Section 2.1.1. For the doped samples, a small red-shift of the gap is observed, as expected due to the widening of the Urbach tails caused by the dopant states, to an average of $(3.154 \pm 0.015)eV$.

4.5 Nanoparticles Choice

After all the physical and optical properties of the sample, the nanoparticles to deposit on them have to be chosen. As four samples are available for each doping level, the ideas behind the choice are the following:

– one of the nanoparticles chosen should have a plasmon resonance energy just below the samples bandgap;

– the remaining three nanoparticles must have plasmon energies covering the region near $2.2eV$.
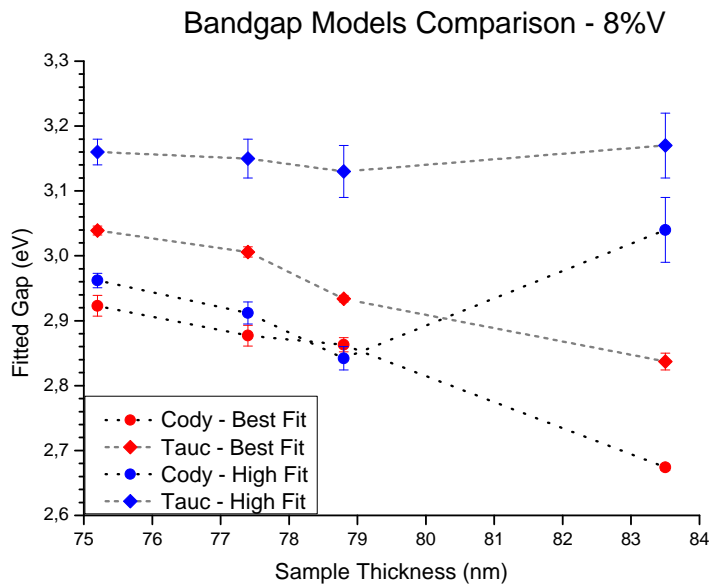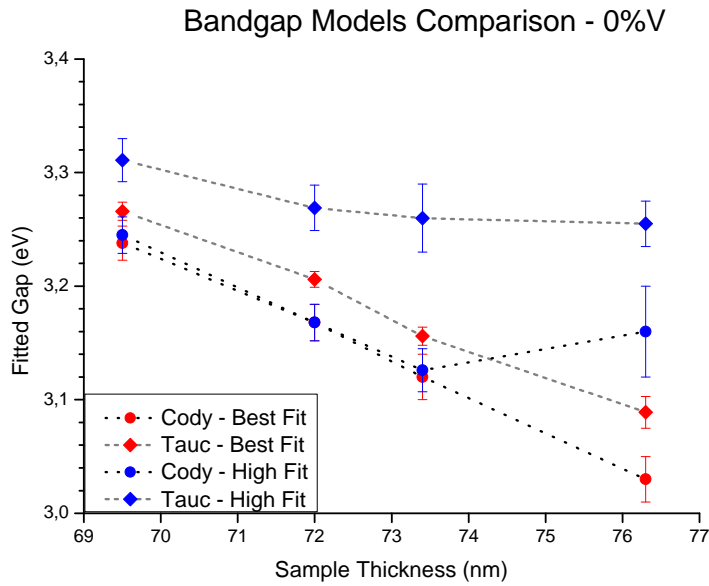
Figure 4.7: Comparison between the bandgaps obtained from the *Tauc-* and *Cody-plots*, respectively identified by circle and diamond symbols, versus the samples thickness. Red sets indicate the *best* fits, according to Appendix C.1, while the blue ones are for the *high* fits obtained by the script of Appendix C.2. Clear linear patterns are visible for the *best* fits; *Cody* fits have all similar patterns with the exception of one strongly deviating point, probably due to random features on the sample. *Tauc high* fits have all consistent values, and show only a faint linear pattern.
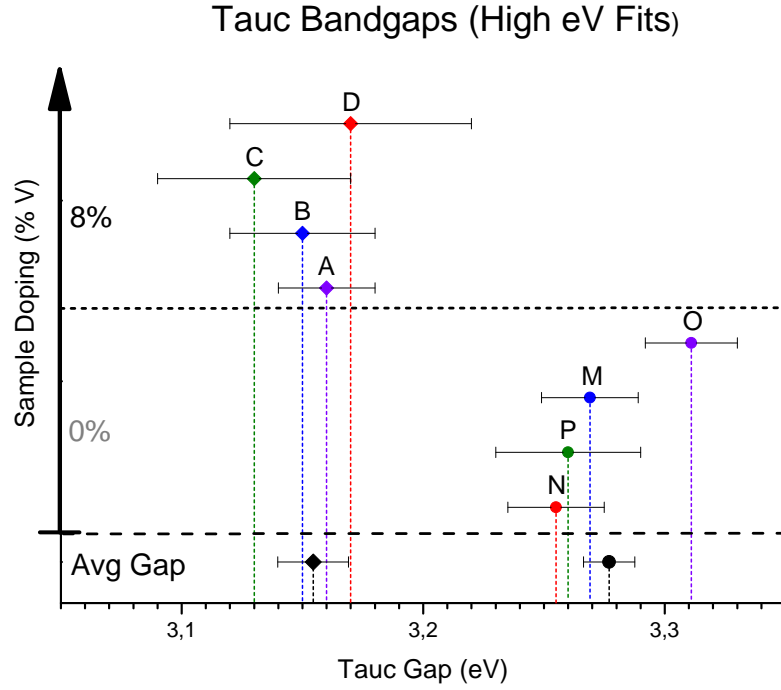
Figure 4.8: Samples bandgaps obtained from linear fitting their *Tauc-plots* at the *highest energies*. The numerical values are reported in Table 4.6.

Sample	Bandgap [eV]	MSE of the Linear Fit
A	3.16 ± 0.2	4.752
B	3.15 ± 0.3	7.094
C	3.13 ± 0.4	8.523
D	3.17 ± 0.5	11.99
M	3.311 ± 0.019	3.303
N	3.269 ± 0.020	3.838
O	3.26 ± 0.03	2.619
P	3.255 ± 0.020	3.536

Table 4.6: Samples bandgap values obtained from linear fitting their *Tauc-plots* at the *highest energies*. A graphical representation of the values is shown in Figure 4.8.

The reasoning is that in such a way it would be able to compare how the presence of the V doping influences the nanoparticles near the dopant states; for the NPs with LSPR at higher energies there should be no significant difference observable. Also, if differences arise only for some of the lower energy LSPR nanoparticles, it could also provide evidence on where the actual dopant states lie. In fact, it is reasonable to believe that only the nanoparticles with plasmon energy higher that the necessary to promote electrons from the V states to the conduction band can "couple" with this process, while the NPs with LSPR at lower energies would not have energetic enough electrons.

First of all, based on literature and previous experience, Au and Ag were chosen as the materials to be used [18, 27, 29, 30, 59]. This is because of the wide availability of commercially produced nanoparticles solutions of these two metals, with resonant energy compatible with the required specifications. Before any deposition took place, preliminary *Finite-Difference Time-Domain* (*FDTD*) simulations of the nanoparticles absorption when in contact with a TiO_2 layer were performed, to better evaluate which nanoparticles were suited to the task. *FDTD* is a method of simulating electromagnetic interactions in a wide variety of environments, which has been widely used in literature since its conception in 1966 [17, 31, 60].

After the optimal nanoparticles were found through simulations, they were procured and their spectra measured for reference.

4.5.1   Preliminary FDTD Simulations

First of all, the absorption of a variety of Au and Ag nanoparticles was studied. Simulations were performed ranging the particle diameters from 5 to $100nm$ for gold and from 10 to $80nm$ for silver, using a script provided by the research group of Prof. Baldi. The refractive index used to model the TiO_2 are those obtained in Section 4.2.2. The resulting plots are shown in Figure 4.9. It must also be noted that, according to previous experience with such simulations, a small redshift of the actual peak position from the simulated value is to be expected in the real samples. This can be caused by inaccuracies in the measurements, particles shape deviating from spherical, or the presence of oxides and surfactants on them.

Concerning Ag, the refractive index used is by Yang et. al. [61]. The diameter of $50nm$ was chosen as such nanoparticles were easily available, and their peak is positioned at $3.205eV$ and in the actual samples it should shift to right below their bandgap value.

Regarding Au, the refractive index is by Johnson and Christy [62], and the three diameters 100, 50 and $20nm$ were chosen. The first two showed peaks at 2.282 and $2.389eV$ respectively, while the peak of the smallest particle couldn't be
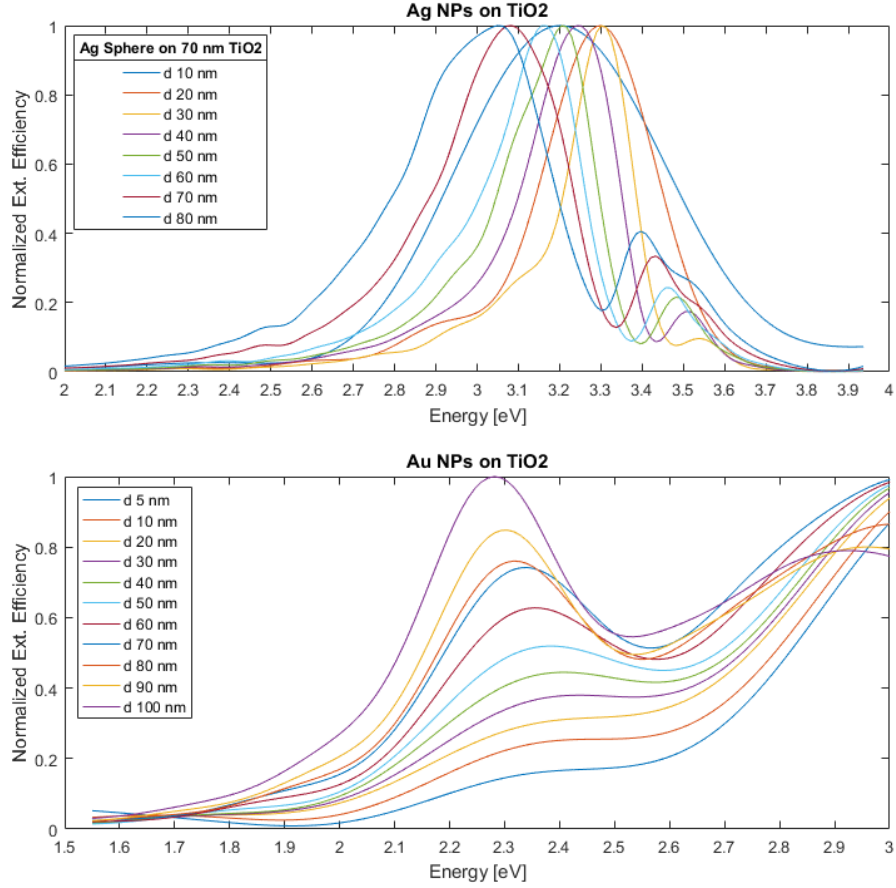
Figure 4.9: *FDTD* simulations of the light extinction for a range of *Ag* and *Au* nanoparticles of different diameters, deposited on a TiO_2 film $70nm$ thick. While choosing which *silver* nanoparticle to choose, the presence of secondary peaks at higher energies was also taken into consideration. In the *gold* simulations it is clearly visible that, for energies above $2.5 \div 2.6eV$ the extinction coefficient rises significantly; this can be explained by the fact that interband transitions are happening in the *Au* bulk, but shouldn't interfere so much with the simulations, and in reality this rising is excessive and due to simulation artefacts.

precisely determined due to its low light-nanoparticle-interaction cross-section, and its being close to the intergap transitions of Au. It was chosen nonetheless as, from the available data, it seemed to have a slightly higher peak energy than the $50nm$ one; this grants that even if lightly red-shifted after the deposition, the peak would still remain above the $2.2eV$ value where the V states are expected.

4.5.2 Nanoparticles Spectra

According the nanoparticle choice done, the following solutions were acquired:

- **$Ag50nm$**: *Simga-Aldrich 796131-25ML*, $50nm$ avg. diameter, Ag citrate functionalized nanospheres, in $25mL$ of $2mM$ aqueous sodium citrate;

- **$Au20nm$**: *Simga-Aldrich 741965-25ML*, $20nm$ diameter, citrate-surfactant-stabilised suspension of Au nanoparticles, in $25mL$ of water;

- **$Au50nm$**: *Simga-Aldrich 742007-25ML*, $50nm$ diameter, citrate-surfactant-stabilised suspension of Au nanoparticles, in $25mL$ of water;

- **$Au100nm$**: *Simga-Aldrich 742031-25ML*, $1000nm$ diameter, citrate-surfactant-stabilised suspension of Au nanoparticles, in $25mL$ of water.

The measured transmission spectra of the solution is reported in Figure 4.10, while their plasmonic energy peaks are tabulated in Table 4.7. The values obtained are all slightly lower than those simulated through FDTD. This should not be the case, as a redshift is expected once the particles are deposited, rather than a blueshift. Further investigation and improvements of the FDTD scrips are thus required before future simulations are made, as well as the use of a better-fitted refractive index for the TiO_2.

4.6 Spectroscopic Analysis

In this final section, the spectroscopic analysis of the samples is discussed. First, a brief overview on the physical and optical properties of the samples manufactured is reported, together with a microscopical analysis to judge the deposition quality.

Then, the bulk of the analysis is presented. It covers the study of the transmission and reflection measurements spectra of all the samples datasets, with a focus on comparing the measurements before and after NPs deposition and washing, as well as on finding similarities and differences between the undoped

Nanoparticle Solutions Transmission Spectra
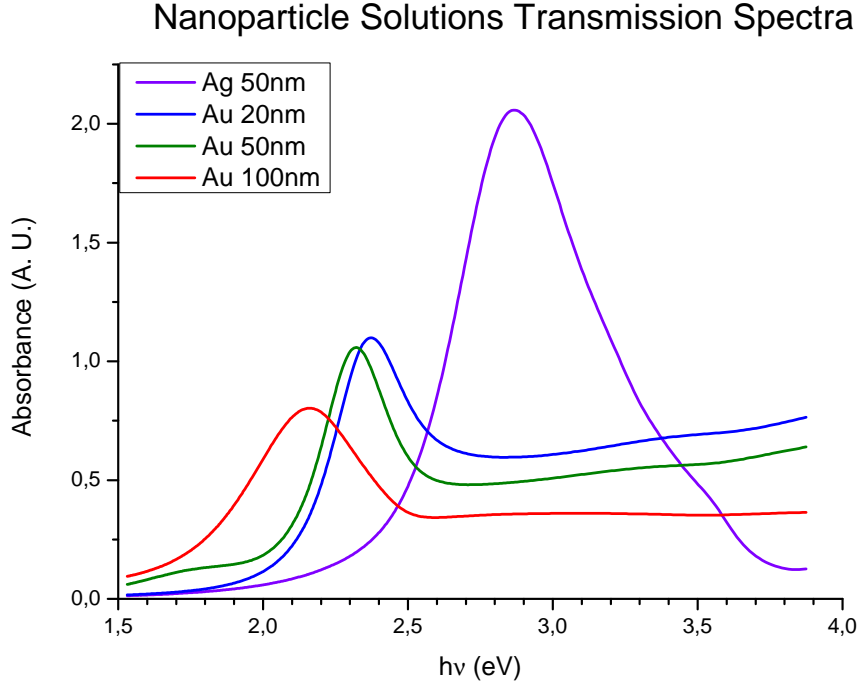
Figure 4.10: Transmission spectra of the chosen nanoparticles solution. The absorption peaks are clearly visible. It can also be noted that for energies above the peaks, Au NPs show non-zero absorbance, due to interband absorption and light scattering phenomena, though the amplitude of the absorption is not as pronounced as in the FDTD simulations of Figure 4.9.

Nanoparticle Solution	Absorption Peak $[eV]$
$Ag 50nm$	2.863
$Au 20nm$	2.375
$Au 50nm$	2.322
$Au 100nm$	2.160

Table 4.7: *Absorption peak* positions of the four nanoparticle solutions chosen.

Sample	Deposited NPs	TiO_2 Thickness [nm]	Bandgap [eV]	$V\%$ [$at.\%$]
O	$Ag50nm$	69.5	3.26 ± 0.03	0%
M	$Au20nm$	72.0	3.311 ± 0.019	0%
P	$Au50nm$	73.4	3.255 ± 0.020	0%
N	$Au100nm$	76.3	3.269 ± 0.020	0%
A	$Ag50nm$	75.2	3.16 ± 0.2	$\approx 8\%$
B	$Au20nm$	77.4	3.15 ± 0.3	$\approx 8\%$
C	$Au50nm$	78.8	3.13 ± 0.4	$\approx 8\%$
D	$Au100nm$	83.5	3.17 ± 0.5	$\approx 8\%$

Table 4.8: Overview of the physical and optical properties of the samples. The sample ordering is: undoped samples before doped ones; more energetic nanoparticles deposited before less energetic ones (which incidentally means the ordering is from thinnest to thickest).

and doped samples.

To better understand the data acquired, further analysis are performed comparing it with FDTD simulations to check the validity of the deduced conclusions.

4.6.1 Samples Overview

Before proceeding at analysing the data, an overview on the samples properties and specifications determined so far must be done. All the relevant informations concerning the samples measured are reported in Table 4.8. The association of nanoparticle solution and sample was done linking the particles LSPR energy to the samples thickness: i.e. the NPs with highest LSPR energy were deposited on the thinnest samples, and so forth until the particles with lowest LSPR energy were deposited on the thickest samples. The choice was arbitrary.

Other than the significant values reported, it is also important to know how the deposited nanoparticles were distributed, before and after the washing procedure. In Appendix D the most significant DF microscopy images of each sample are shown. It can be clearly seen that the *deposited dataset* of samples with *Au* NPs have significant quantities of contaminants deposited on them. These whitish objects, which make the samples look "milky" at the bare eye, are probably made of the citrate capping of the *Au* particles, but completely disappear after the washing procedure. Moreover, the washing does strip away most of the clustered nanoparticles in the samples deposited with *Au* NPs, but also not many particles persist after the washing, causing a significant reduction in the amplitude of the measured spectra as less nanoparticles are present. Other

than that, all the Au NPs tend to cluster, with the phenomenon being more emphasised as their diameter decreases. This is an expected phenomenon as explained in Section 2.2.1. The Ag nanoparticles were significantly less effected by both these phenomena, implying that the citrate capping of the Au NPs might also play a role in the clustering. Finally, it is clear that the dropcasting method of deposition used (Section 3.4.3), even if assisted by plasma-cleaning procedures, is not optimal for studying single-particle effects on the plasmonic nanoparticles. Other approaches must be taken in the future, as NP-NP interactions are inevitably present in the measurements performed.

4.6.2 Transmission Measurements

Transmission measurements were performed on all the three datasets of samples (*bare*, *deposited*, *washed*) as described in Section 3.4.1. The quantity studied is the *absorbance*, measured in *absorbance units* (*A.U.*). As the *bare* samples have been already discussed in Section 4.4, this section is focused in studying the other two datasets, and how they are related the doping level and the deposited nanoparticles.

With the experimental apparatus used the interference fringes present in the spectra cannot be removed using (2.2) as it requires to measure the perpendicular *reflectance*, which is not possible. As those fringes lie in the region where the V states and the Au NPs plasmonic resonance are, no evaluation of their linewidth could be made to study possible CID phenomena, and other ways to investigate that region of the spectrum have to be used. The most promising way of analysing the effect of the NPs presence is to analyse the difference between the *deposited/washed* spectra and the *bare* ones. Thus, the quantities plotted and studied are:

$$\Delta_{dep} = T_{dep} - Tbare \qquad [A.U.] \qquad (4.5)$$

$$\Delta_{wash} = T_{dep} - Tbare \qquad [A.U.] \qquad (4.6)$$

with clear meaning of the symbols. The resulting graphs are reported in Appendix A.4.

From a qualitative point of view, the *deposited* plots all have the same shape, which indicates an improved absorption capability of the samples at energies similar to the TiO_2 bandgap and a worsening at other energies. Quantitatively speaking, when $Au20nm$ and $Au50nm$ particles are deposited, a redshift in the position of the peak between doped and undoped samples is clearly visible. Looking at these shifts plotted against the NPs plasmonic energy in Figure 4.11 a clear trend is visible: for plasmonic energies until $\approx 2.2eV$ there is no
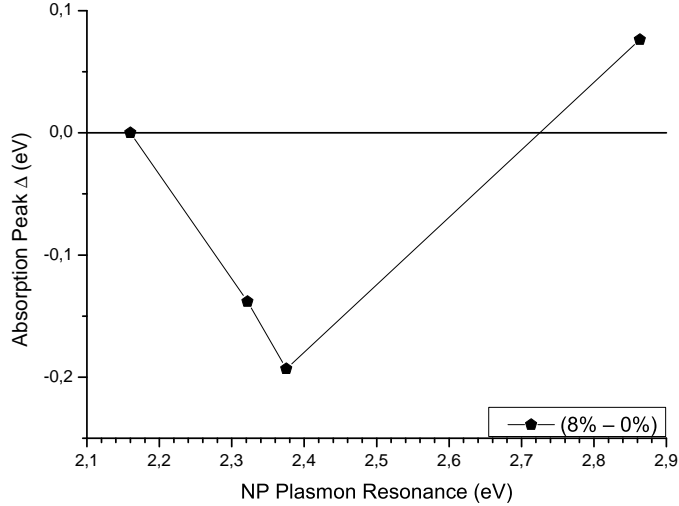
Figure 4.11: *Absorption peak shifts* between doped and undoped *deposited* samples (doped minus undoped), versus the *plasmon energy* of the NPs used.

difference between doped and undoped samples; at higher energies the doped samples have peak absorption at lower energies rather than the undoped ones; as the bandgap energy approaches, the peak shift becomes smaller and eventually transform into a blueshift. This is only a partial results, and further measurements with different NPs would be needed to certainly establish the trend. Given the available data, the observed phenomenon could be explained by the fact that the nanoparticle plasmonic excitations couple with the dopant states, artificially shrinking the value of the bandgap, and thus improving the light absorption at energies slightly lower than if no dopant states were present. However, no good explanation for the reduction of the absorbance at other energies can be found, except the possibility that the observed feature is actually an artefact caused by thin film interference. The adding of NPs on top of the sample does in fact change its surface structure, in particular its roughness. It is in fact possible that the *deposited* plots suffer from this, as they are obtained by subtracting the *absorbance* of two samples with very different surface structures. It must also be remembered that the *deposited* samples have significant quantities of contaminants on their surface, which can contribute at dispersing light and thus causing artificial reductions of the absorbed light.

Looking at the *washed* samples, the first observation that the signal intensity is significantly less than in the *deposited* dataset. This can easily be explained by the reduce amount of NPs that this dataset has, and also by the removing

of diffracting contaminants on the samples surface. Thus, these samples are expected to provide more reliable data, though less intense and more difficult to analyse. In fact, while for the $Ag50nm$ samples it can clearly be stated that no significant difference is seen (as expected), already the analysis of the $Au20$ samples becomes difficult. As it can be seen in Figure A.15, sample M provides no significant feature, meaning that the nanoparticles presence doesn't change any optical property compared to the *bare* samples. Looking at the other plots, it is possible to make some qualitative observation. In the undoped samples, the presence of Au NPs enhances light absorption at energies higher than the bandgap, and reduces it at lower energies, while the contrary is true for doped samples. The explanation might be that in the undoped samples, the NPs allow for highly-energetic photons to excite their electrons directly into the conduction band of the TiO_2 through *direct-charge-transfer* processes. But when V states are present at energies similar to the NPs plasmonic resonance, the dopant *quenches* the electron transfer to the conduction band, as now the NPs have another *direct-charge-transfer* channel at lower energy, directed to the dopant states themselves. This process might explain the absorption increase, but cannot determine why there is an absorption reduction at other energies. The reason behind this last phenomena might be again due to thin film interference issues, caused by the variation of surface structure and properties. An observation further confirmed by the fact that the samples deposited with $Ag50nm$ particles, which showed much less clustering than the Au ones, have almost no negative points in their *washed* plots.

To better understand the dynamics of these processes, FDTD simulations of the samples were performed and are discussed in the final section of this chapter.

4.6.3 Reflection Measurements

Reflection measurements yielded results even less clear than the ones reported in the previous chapter. This is probably due to the use of equipment (Section 3.4.2) not sensitive enough to the small scale of the phenomena observed, or to the inadequacy of the technique used and the samples prepared. First of all, reflection measurements should be performed with a perpendicular incident beam of light, rather than angulated, so that it would be possible to use (2.2) to remove thin-film-interference-fringes. As such measurements were not possible, the same approach of the previous section as used for the analysis of reflection spectra, studying the values

$$\Delta_{dep} = R_{dep} - Rbare \quad [A.U.] \tag{4.7}$$

$$\Delta_{wash} = R_{dep} - Rbare \quad [A.U.] \tag{4.8}$$
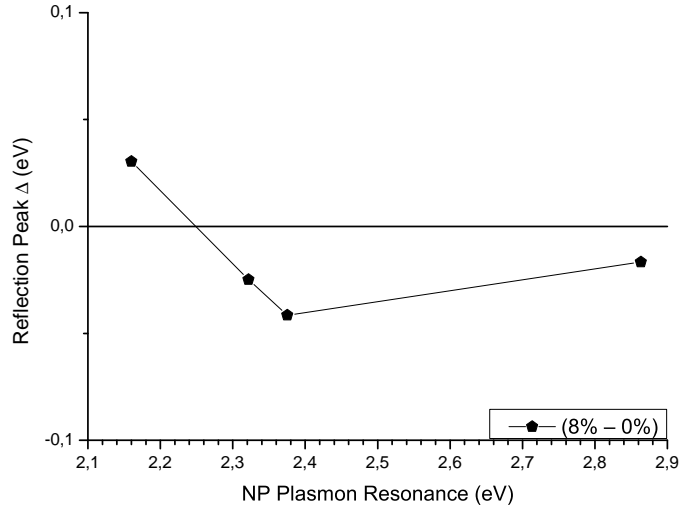
Figure 4.12: *Reflection peak shifts* between doped and undoped *deposited* samples (doped minus undoped), versus the *plasmon energy* of the NPs used.

instead of (4.5) and (4.6). The resulting plots are shown in Appendix A.5.
In these plots it is clearly visible that the *washed* samples carry no meaningful data, and their reflection spectra is essentially identical to those of the *bare* samples.

Concerning the *deposited* samples, the same reasoning discussed in the previous section can be applied. Looking at the reflection shifts plotted against the NPs plasmonic energy in Figure 4.12, the same trend as of Figure 4.11 is visible. The fact that the same phenomena happens in both the transmission and reflection spectra can however be more reasonably explained by thin-film-interference phenomena than electronic coupling. The latter, in fact, should influence only the amount of absorbed, and not the reflected and diffracted light.

The FDTD simulations discussed in the next section are used to try to give a final interpretation to the phenomena observed.

4.6.4 Comparison with FDTD Simulations

Due to time constraints, the FDTD simulations were performed using scripts already in use by the research group of Prof. Baldi, which are not tuned to perfectly model the phenomena observed, but can give some insight on the processes involved. The simulations model the behaviour of a single nanoparticle deposited on top of a TiO_2-glass substrate, giving as a result the extinction

Ag50nm on 0%V:TiO$_2$ - Transmission Spectrum

Ag50nm on 8%V:TiO$_2$ - Transmission Spectrum
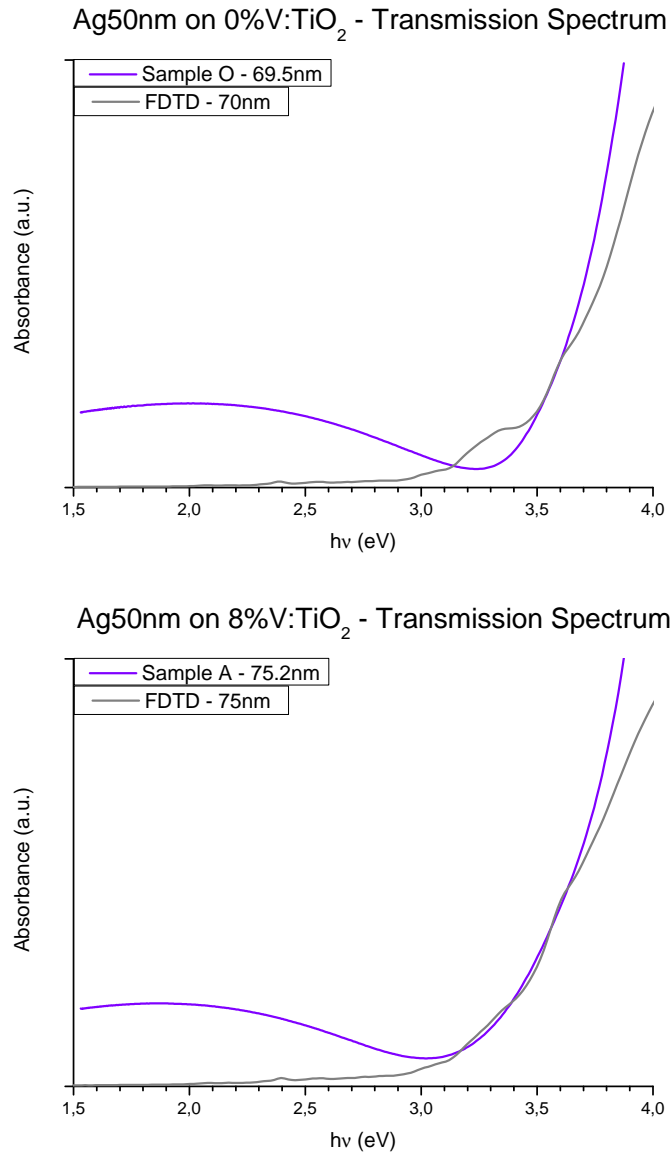
Figure 4.13: *Transmission spectra* in *arbitrary units*: comparison between measurements and FDTD simulations; the thickness in the plot labels are referred to the TiO_2 film. It is clearly visible that the FDTD fails at modelling the interference fringe, and presents a small "bulge" where the $Ag50nm$ plasmonic resonance is; this feature cannot be seen in the measured spectra, probably due to non-comparable scales of the data.

Au50nm on 0%V:TiO$_2$ - Transmission Spectrum

Sample P - 73.4nm
FDTD - 73nm

Absorbance (a.u.)

hν (eV)

Au50nm on 8%V:TiO$_2$ - Transmission Spectrum

Sample C - 78.8nm
FDTD - 79nm

Absorbance (A. U.)

hν (eV)
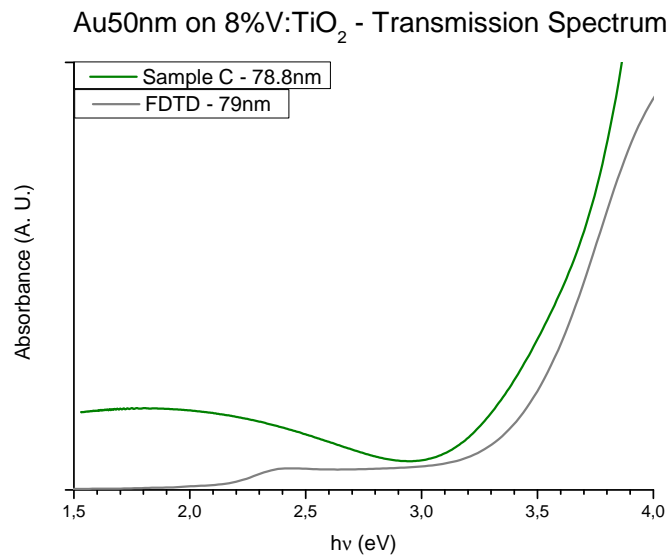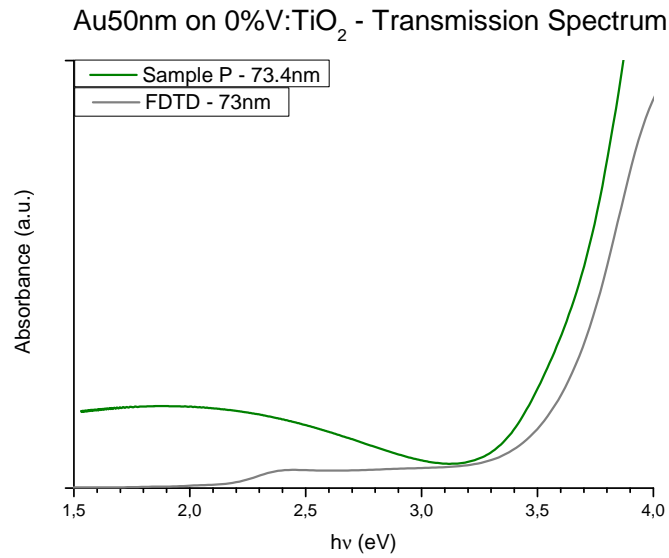
Figure 4.14: *Transmission spectra* in *arbitrary units*: comparison between measurements and FDTD simulations; the thickness in the plot labels are referred to the TiO_2 film. It is clearly visible that the FDTD fails at modelling the interference fringe, and no plasmonic feature is visible.

and transmission spectra of the particle. By comparing the last one with the experimental data, it should be observed if there is agreement on the shape and position of the features previously described in this chapter. The simulated extinction peak position can also help in discerning features of plasmonic origin from those caused by interference and other causes. As with the previous FDTD simulations described in Section 4.5.1 the refractive indices used for Au and Ag are by Johnson and Christy, and Yang respectively [61, 62]; for the TiO_2 the indices obtained through ellipsometry are used (Section 4.2.2). The samples which were chosen to be modelled (as time constraints made it impossible to simulate them all) are:

- sample O: $Ag50nm$ deposited, $69.5nm$ of 0% $V:TiO_2$;

- sample A: $Ag50nm$ deposited, $75.2nm$ of 8% $V:TiO_2$;

- sample P: $Au50nm$ deposited, $73.4nm$ of 0% $V:TiO_2$;

- sample C: $Au50nm$ deposited, $78.8nm$ of 8% $V:TiO_2$.

The choice was done in order to be able to compare samples with NPs of the same size but different metal, one of which with plasmon resonance slightly below the substrate bandgap ($Ag50nm$) and the other slightly above the expected dopant states ($Au50nm$).

Looking at the comparison of measured and simulated transmission spectra in Figure 4.13 and Figure 4.14, it is immediately and unfortunately clear that the scripts used do not model accurately the thin film interference of the substrate, making these simulations of little use.

Analysing the simulated extinction spectra shown in Figure 4.15 can on the contrary provide some meaningful informations. First of all, it is clearly visible that the extinction peaks of $Ag50nm$ particles completely overlap the spectral region where the TiO_2 bandgap is. This is true even after considering the fact that the peak is slightly blueshifted rather than redshifted in comparison to the peak of the NPs solution shown in Figure 4.10, an issue probably due to imperfect simulation parameters or to the deviation of the actual particle size from the declared $50nm$. The fact that the extinction lies so close to the bandgap can explain part of the features visible in Figure A.14.

Looking at the $Au50nm$ peaks, on the other hand, there is no clear connection to the data observed. The only feature in Figure A.16 which could be explained by the presence of NPs extinction peaks, i.e. the "double valleys" at $2 \div 2.5eV$, are present at significantly higher energies that the peaks obtained with the FDTD simulations. As for the Ag simulations this can be explained by their inadequacy in modelling such phenomena, indicating that in the future *ad hoc*

scripts must be used to obtain any significant information.

An interesting qualitative observation can finally be made. Even if the extinction peak positions are with all probability offset from real values, the fact that there is a visible shift in the Au peaks but not in the Ag ones is in agreement with the peak shift discussed in the previous sections and summarised in Figure 4.11. Whether this is a coincidence or a clue to some phenomena, happening while hidden by interference fringes, is a question that must be answered by new measurements and more accurate simulations.
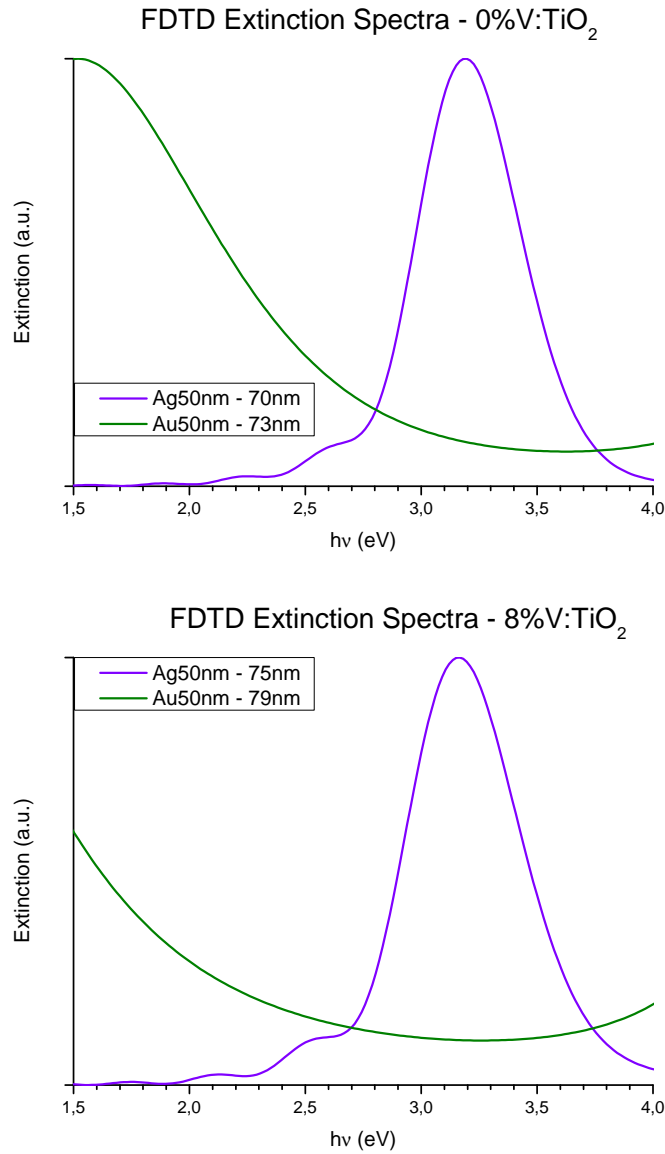
Figure 4.15: *Extinction spectra* in *arbitrary units* as obtained with FDTD simulations; the thickness in the plot labels are referred to the TiO_2 film. *Ag* peaks are clearly modelled, though slightly blueshifted respect to the value measured from the nanoparticle solution actually used $(2.863eV)$; this is probably due to simulation imprecisions or NPs diameter being slightly different than the $50nm$ declared by the manufacturer. *Au* peaks are extremely wide and redshifted respect to measured values, indicating possible flaws in the simulations or that further measurements at lower energies are needed to observe meaningful data; though the discrepancies with the small peaks observed in Figure A.16 tend to confirm the presence of simulation errors.

5 - Conclusions

The experiments performed while working on this thesis have proven to yield a mixture of satisfactory and unsatisfying result at the same time, though the work done for this project can be considered relevant to any future research in the field of *metal/doped-semiconductor plasmonic nanostructures*. The results obtained and described in the previous chapter are now summarised and discussed, following the same order of topics.

Concerning the thin-film preparation good results have been achieved, although further improvements are necessary for future samples preparation. All the films turned out to be significantly thicker than expected, though this can be primarily attributed to the wearing of the sputterer target, for which a new calibration is suggested. The annealing process performed consistently produced Anatase, confirming the reliability of the procedure used. Moreover the bandgap of the samples were measured, giving an average result of (3.277 ± 0.011), in complete agreement with literature.

The only real issue regards the *ellipsometry* and *XRR* measurements. To use effectively these techniques, extremely smooth samples are needed, and the ones deposited did not match this requirement effectively. This is visible especially with ellipsometry: it was in fact impossible to accurately obtain the refractive indices of the samples. An approximate model had in fact to be used, compromising the accuracy of both *Optical* and *FDTD* simulations. In future works, high attention must be paid in producing samples as flat as possible, if a good measurement of the refractive index of the samples is necessary. This can be achieved in three ways: plasma cleaning the substrate before the film deposition to improve its wettability and reduce roughness; performing longer and more powerful *plasma cleaning* of the samples, with the risk of damaging it and compromising its optical properties; using flatter substrates than glass, e.g. quartz. The best approach is probably to do a combination of all of them, with a careful observation of the effects caused on the optical properties. Finally more extensive measurements, performed at non-fixed angles, should be performed to improve the general quality of data.

A huge issue encountered in this work arises from the fact that the *dropcasting* of nanoparticles solution is an absolutely sub-optimal technique, if accurate optical measurements have to be performed. This is because after dropcasting the solution the particles inevitably tend to cluster together, even after the plasma cleaning hugely improved their wettability, and the drying time was increased. Moreover, smaller particles tend to cluster more, and especially the Gold ones. This is probably due to their citrate capping, which also remains deposited acting as light scatterer and reducing measurement accuracy. Finally, when NPs clusters and contaminants are washed, the signal intensity decreases significantly, though this could be compensated by the use of more intense light sources. In conclusion, alternative deposition techniques have to be used in future works: the use of *spin-coating* deposition [63] rather than dropcasting might improve this, though the contaminant issue could remain if commercial nanoparticles as those deposited in this project are used. A possibility would be to self-produce the needed nanoparticles, but their quality (consistency of size and shape) should first be evaluated. An alternative method would be to use nanomaterials other than particles, directly "printed" on the semiconductor to avoid contamination. *Metallic nanodisks* could prove to be a viable solution, though a more thorough research regarding the materials and sizes to use is necessary.

Finally, a discussion on the actual optical spectra, and the informations obtained from them, is necessary. First of all, spectra analysis of the samples has been plagued by the presence of *thin-film-interference*. Even if its presence proved valuable in accurately determine the samples thickness through Optical simulations, all the features of interest for this project were "hidden" by it. No evaluation has in fact been possible on the presence of *CID*, as the extinction peaks of the nanoparticles could not be measured. The mathematical removal of the interference fringes also could not be performed, as it required the measurements of perpendicular reflection other than transmission, which could not be performed with the available instrument. A possible solution to this issue could be to deposit ultra-thin films, which should have little-to-no interference in the spectral region of interest. For this project such samples could not be made due to time constraints, and the attention was shifted in finding other evidence of nanoparticle-TiO_2 interaction, trying to study the variation in *absorbance* and *reflectance* in the samples, after nanoparticles *deposition* and *washing*.

The *reflection measurements* performed using the setup we had at hand proved to be extremely inaccurate and devoid of any information. For future works great attention must be put into accurately measure such spectra, especially in doing so with a perpendicular incident beam of light, to try reducing the

interference fringe with (2.2).

Regarding the *transmission spectra*, some apparent evidence of interactions were observed (Appendix A.4). The *deposited* samples all showed improved absorbance peaked around energies near the TiO_2 bandgap value. More interestingly, shifts of these peaks were observed between samples with the same nanoparticles deposited but different doping levels; this shift was present only in the samples with nanoparticles resonating at energies slightly above the expected V doping states. This can be interpreted as a sign of some interaction between the plasmonic nanoparticles and the dopant states. However, this claim was not backed up by any successful FDTD simulation, which might be due to the fact that the phenomena studied are out of the scope of application of this numerical tool. Thus, it must not be excluded that what is being observed is simply due to interference artefacts.

The *washed* samples on the other hand provide better results. Looking at the samples with $Ag50nm$ deposited (Figure A.14), which has a LSPR energy lower than the bandgap, it can be seen that the presence of the nanoparticles improves the absorbance at the energies compatible with their extinction peak, both with doped and undoped dielectrics. This is expected, as the nanoparticles absorb at those energies, though not with such a broad peak, which could be explained by the coupling of the particle excitations with the promotion of electrons to the conduction band. On the other hand, almost all the samples with Au nanoparticles, which have LSPR energy close to the expected V states, show a peculiar pattern (Figures A.15-A.17): in the samples with undoped TiO_2 an improved absorbance of photons more energetic than its bandgap is present, and a reduction below it; the contrary is true in the samples with the doped semiconductor. The only exception is sample M (undoped TiO_2, $Au20nm$ particles deposited, Figure A.15), for which no feature is observable, as probably due to the excessive removal of particles after the washing.

The conclusion formulated from this observation is the following. Independently by their LSPR energy, the nanoparticles interact with the dielectric, "coupling" the plasmon excitation and the promotion of electrons to the conduction band, through *direct-charge-transfer* mechanisms between the particle to the TiO_2. This means that when photons of energy greater than the Anatase bandgap put the electrons of the nanoparticle in motion, they could then be transferred directly to the conduction band of the semiconductor. When a dopant state is present in between the bandgap, it causes a "quenching" of this phenomenon, as now are the less energetic V states to which the electrons are yielded, causing improved absorbance at all the energies below the bandgap. The fact that this phenomenon is not very intense can be explained by the fact that the V states, which are thought to be partially filled by electrons [10],

first have to be vacated through other optical transitions before this process can happen. A graphical representation of the phenomenon is shown in Figure 5.1. This interpretation however does not explain the reduction in absorbance
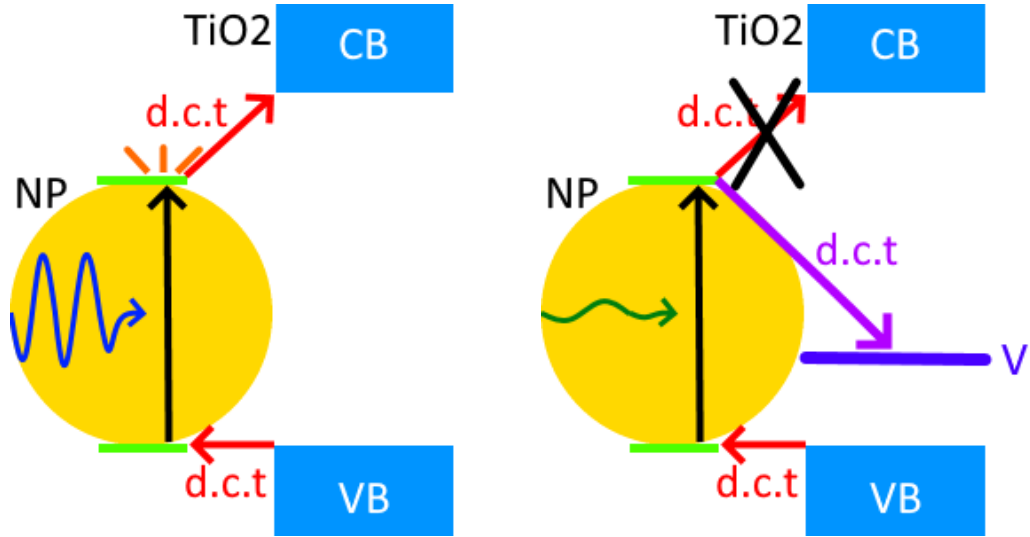
Figure 5.1: Graphical representation of the "quenching" phenomenon discussed. If no dopant states are present (left), photons with energy $> E_{gap}$ excite surface electrons of a nanoparticle (NP) into the plasmonic state, and they "over-excited" as the promoting photon gave them more energy than the one necessary to achieve the plasmonic state; from here, thanks to energy in excess they possess, the excited electrons are transferred to the conduction band (CB) of TiO_2 through *direct-charge-transfer* (*d.c.t.*), while the same happens from the valence band (VB) for charge conservation. If a V dopant state is present (right), due to its lower energy level compared to the CB, it allows the same phenomenon to happen through photons just energetic enough to excite electrons in the plasmonic state ($E_{photon} < E_{gap}$); as this process requires less energy, the dopant redirects all the d.c.t. towards itself, effectively "quenching" the charge transfer to the CB.

present at other energies, which could also be attributed to interference effects. Unfortunately the FDTD simulations could not provide significant help in understanding the processes observed. This is to ascribe mainly to the fact that the simulations performed were developed to model other phenomena, and proper modifications to the scripts could not be performed due to a lack of available time.

In conclusion, currently no strong evidence of the coupling between plasmonic and dopant states in a semiconductor could yet be found, though hints of

its existence are present. In fact, some interesting correlations between the nanoparticles and the presence of doping (or its absence) were discussed. The true causes of these correlations will have to be determined by further experiments on the subject, which can benefit from the work done in this project, providing suggestions and hopefully solutions on how to proceed in the experimental investigation.

A - Plots Addendum

Here, in the following sections, are reported all the plots cited in the main body of the text which, due to space limitations, couldn't be promptly showed.

A.1 XRD Spectra

In these plots, the XRD spectra of the samples are shown. The black line is the actual spectrum; the red vertical lines indicate the position of the *anatase* lines; the blue ones (hardly visible) should indicate the lines of metallic V, which can be deemed non-present in grains sufficiently big to produce measurable results. Background signal of the X-rays was previously subtracted.
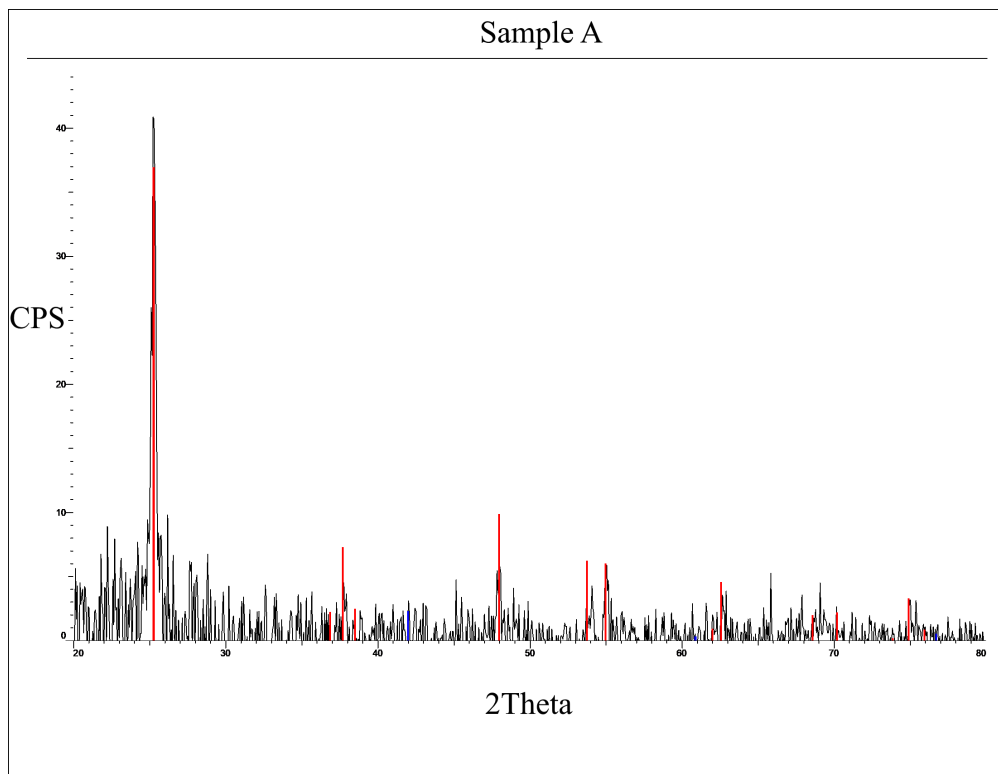
Figure A.1: XRD spectrum of sample A.
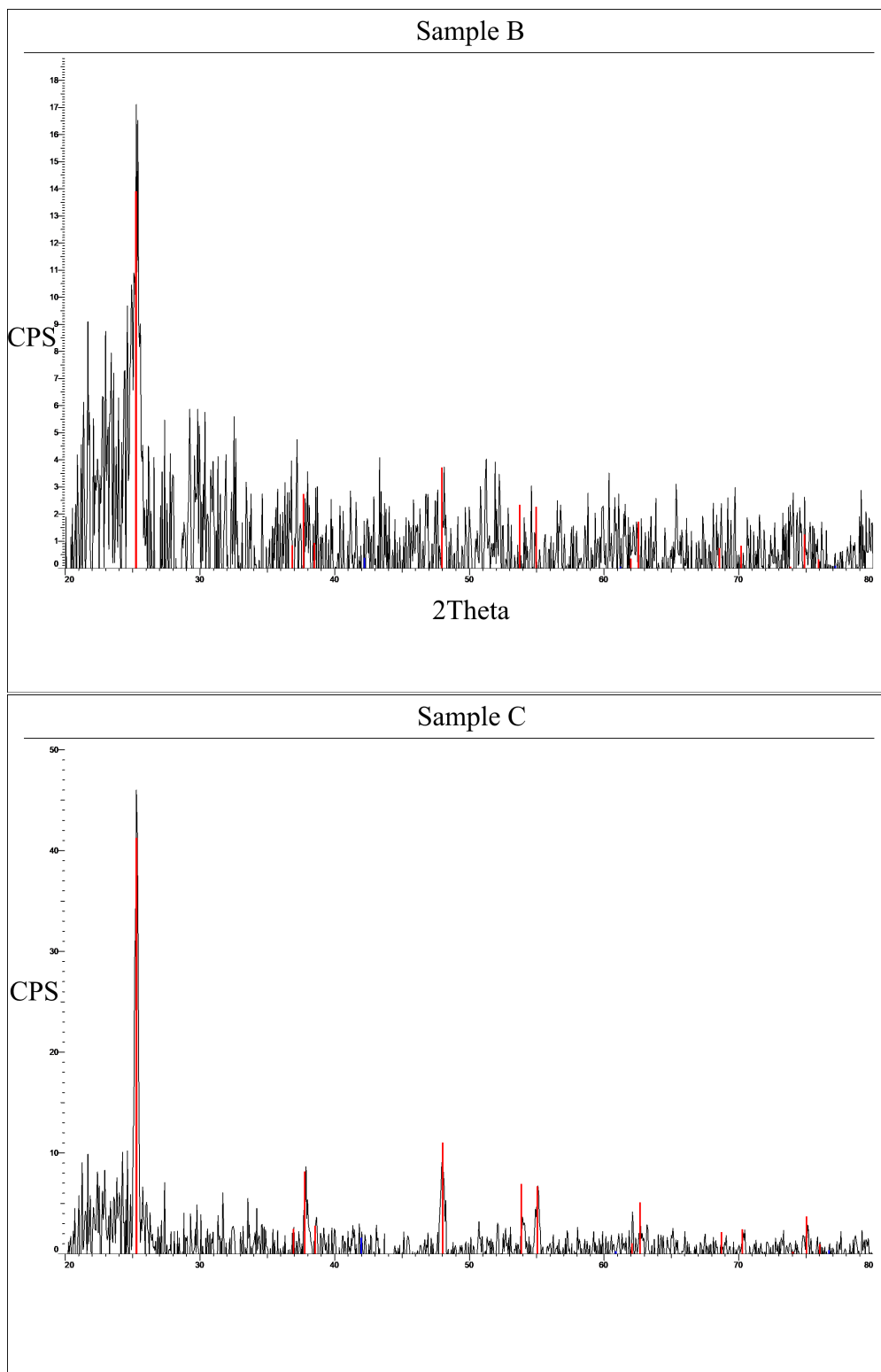
Figure A.2: XRD spectrum of sample B (**top**) and C (**bottom**).
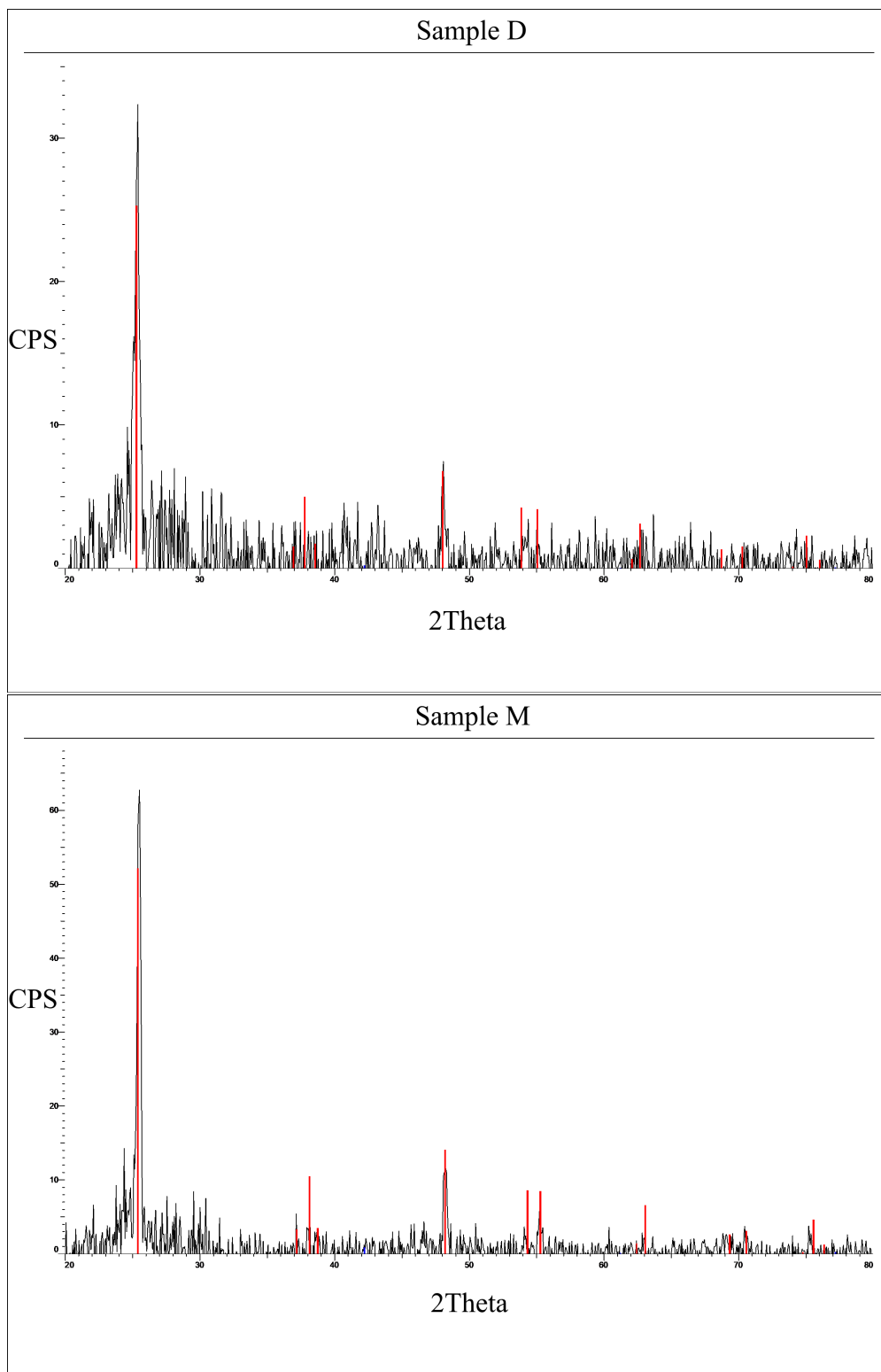
Figure A.3: XRD spectrum of sample D (**top**) and M (**bottom**).
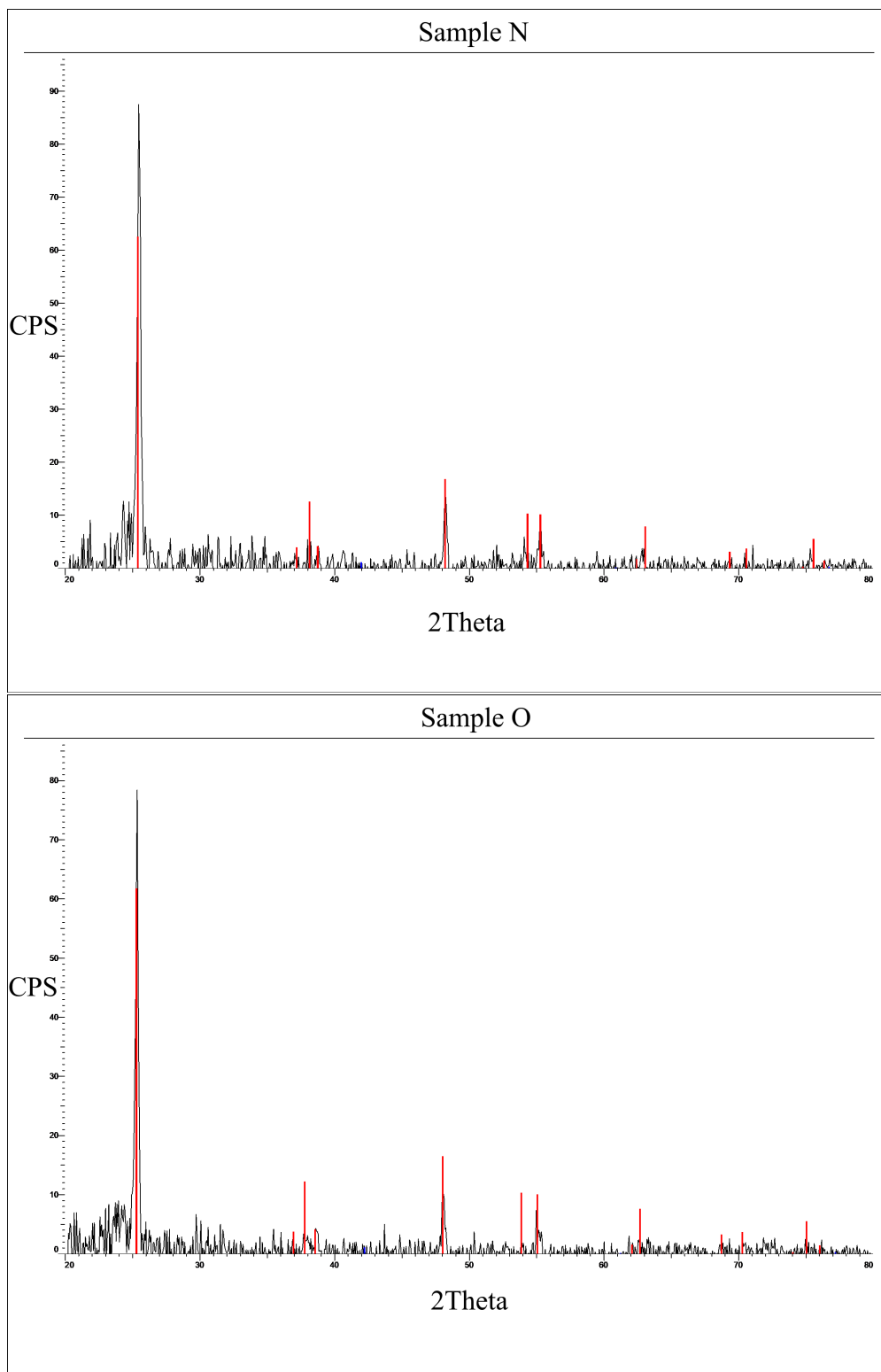
Figure A.4: XRD spectrum of sample *N* (**top**) and *O* (**bottom**).
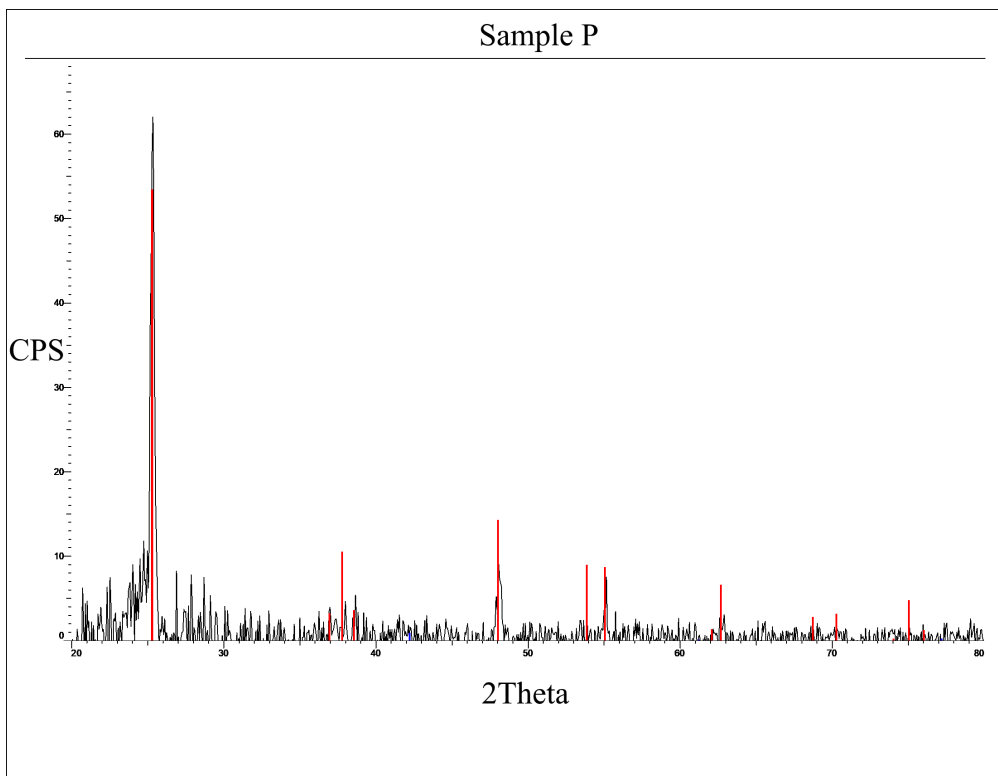
Figure A.5: XRD spectrum of sample P.

A.2 Optical Simulations of *Raw Naked* Samples

These plots show the simulations performed with the *Optical* software, used to search for a common point in the transmission and reflection spectra. Data are in *A.U.*, and to model the TiO_2 films the refractive indices determined in Section 4.2.2 were used.
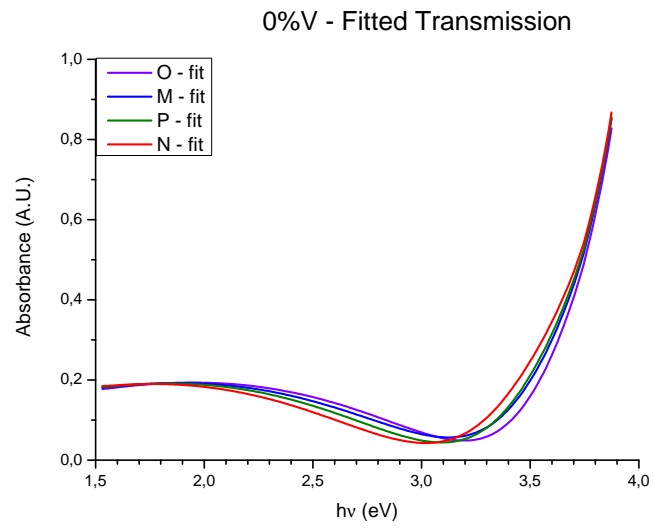
(a)
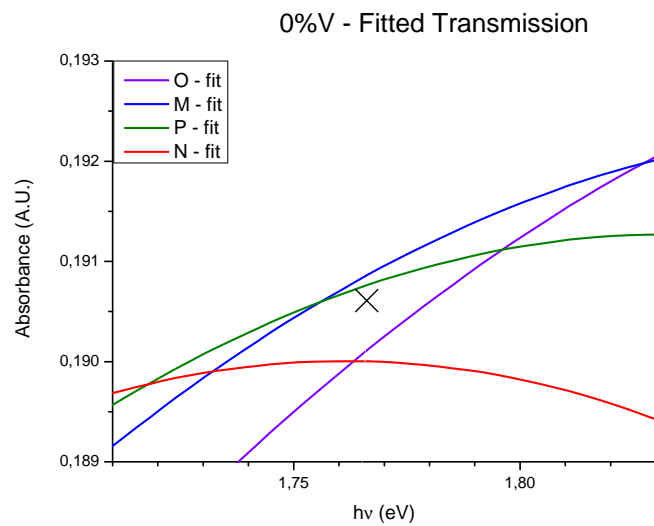
(b)

Figure A.6: **(a)** *Optical* simulation of the transmission spectra of the *raw bare* undoped samples. **(b)** Closeup on the near-intersection region at low energies; the cross is the average position of all the intersections between the various spectra.

8%V - Fitted Transmission

(a)

8%V - Fitted Transmission
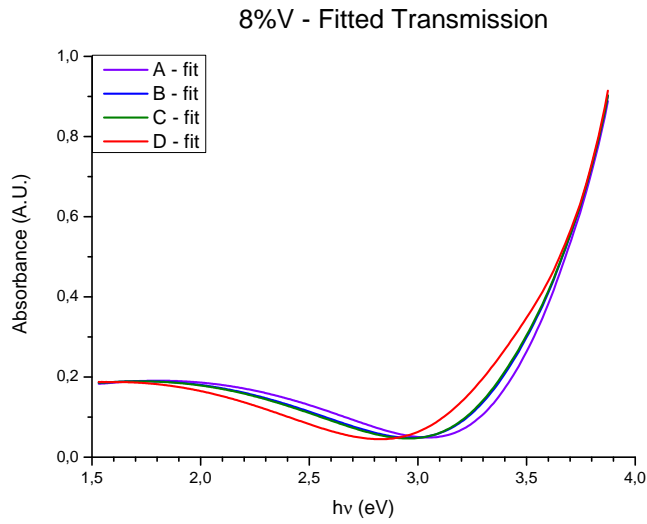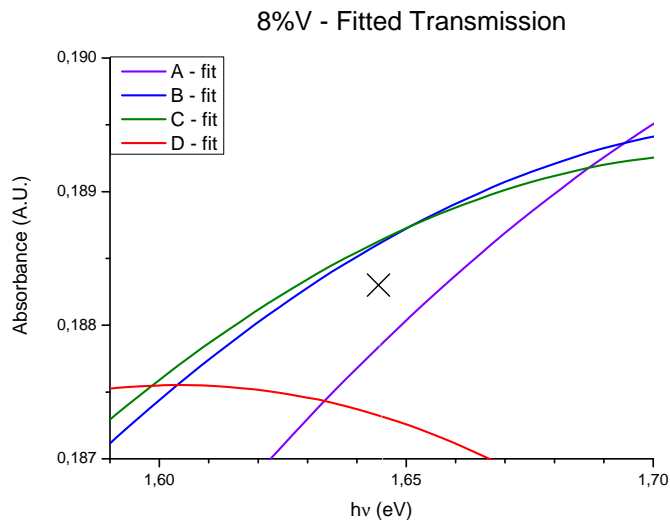
(b)

Figure A.7: **(a)** *Optical* simulation of the transmission spectra of the *raw bare* doped samples. **(b)** Closeup on the near-intersection region at low energies; the cross is the average position of all the intersections between the various spectra.
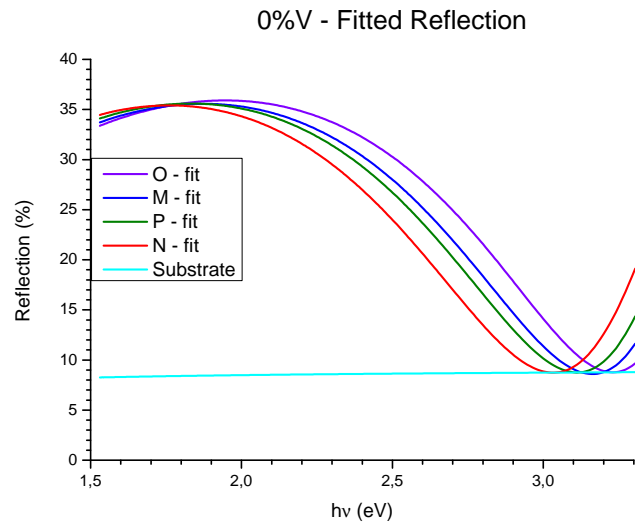
(a)
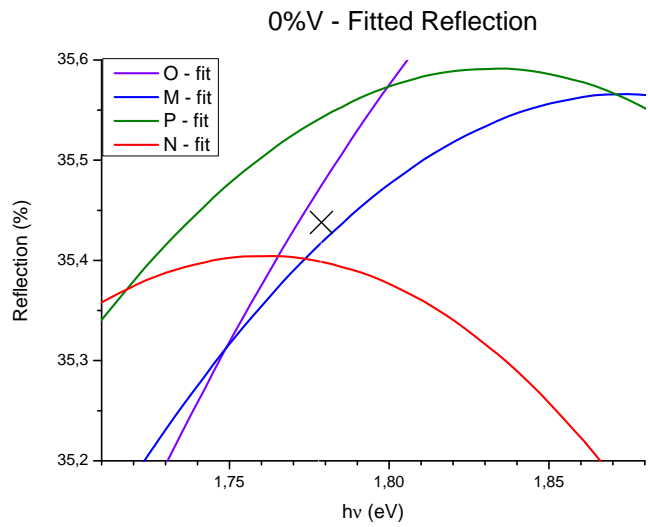
(b)

Figure A.8: **(a)** *Optical* simulation of the reflection spectra of the *raw bare* undoped samples; the glass substrate reflection is also shown for comparison. **(b)** Closeup on the near-intersection region at low energies; the cross is the average position of all the intersections between the various spectra.
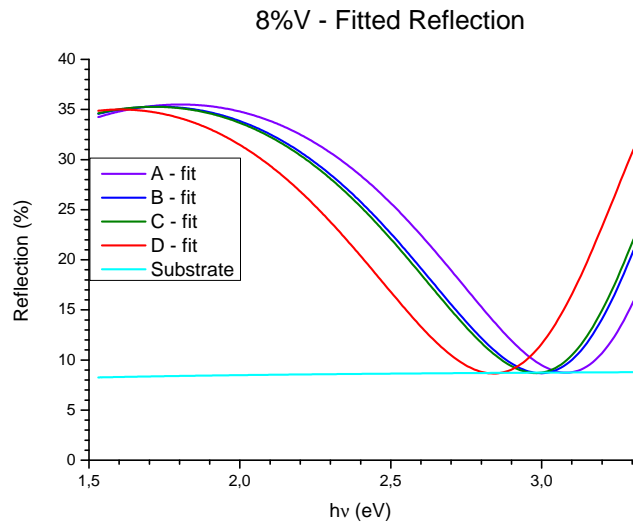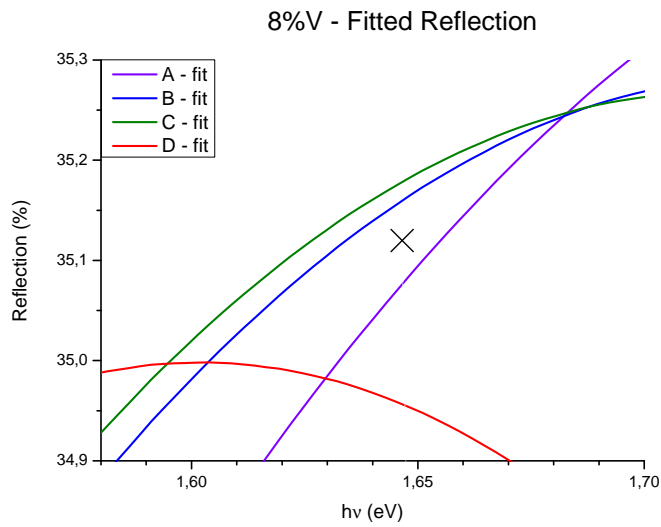
Figure A.9: **(a)** *Optical* simulation of the reflection spectra of the *raw bare* doped samples; the glass substrate reflection is also shown for comparison. **(b)** Closeup on the near-intersection region at low energies; the cross is the average position of all the intersections between the various spectra.

A.3 *Tauc- & Cody-plots* Fitting

The plots represented here show the linear fits of the *Tauc-* and *Cody-plots*, obtained from the transmission spectra, used to determine the samples bandgap. For both of the plots, two different fits were performed. The first aims at fitting the spectral region which provided the best linear fits, found using the MATLAB script shown in AppendixC.1. The second one has the same objective, nut with the additional constraint that one edge of the fitting region has to be the high-energy-extreme of the dataset. This was done to prevent data corruption from disturbances related to think film interference.
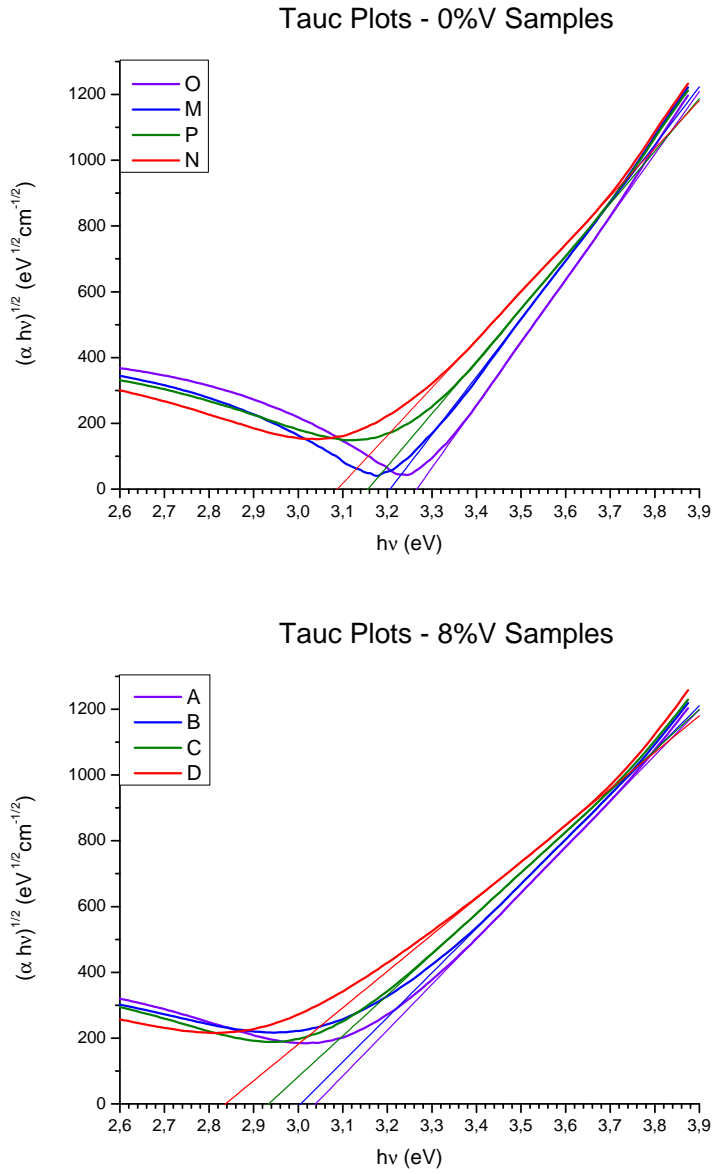
Figure A.10: *Tauc-plots* obtained from the transmission spectra of the undoped (top) and doped samples (bottom). The thick lines are the actual data, the thin ones are the fits, performed in the *absolute* optimal ranges found by the algorithm in Appendix C.1.
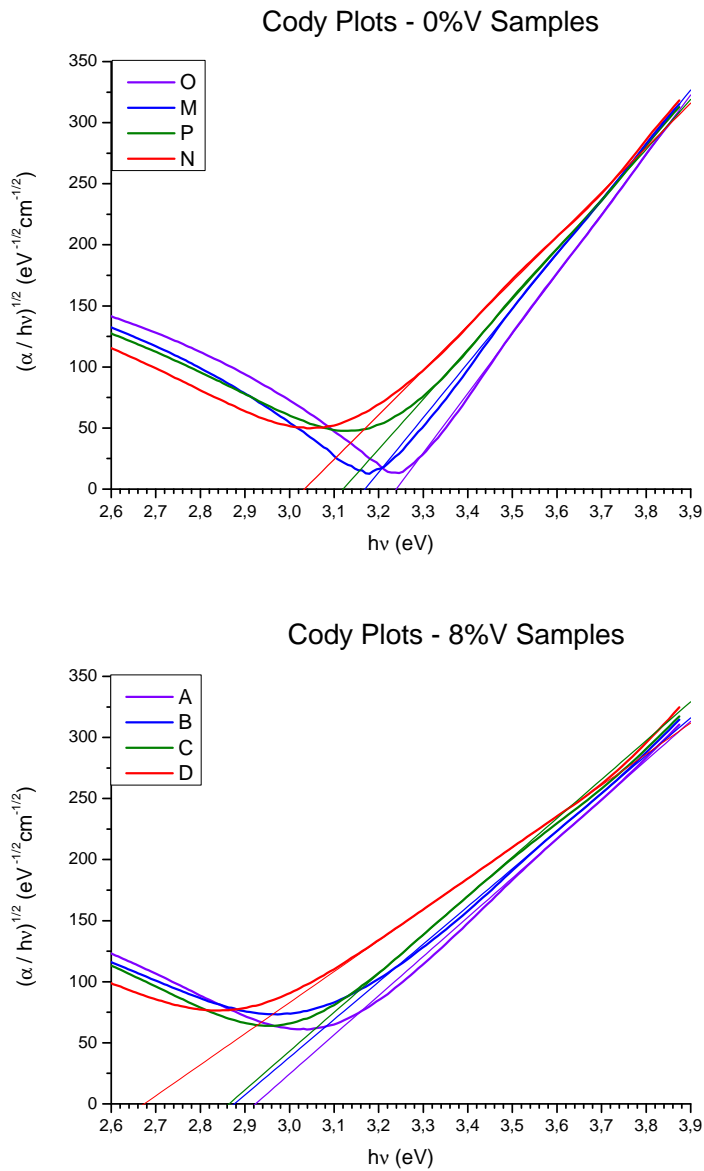
Figure A.11: *Cody-plots* obtained from the transmission spectra of the undoped (top) and doped samples (bottom). The thick lines are the actual data, the thin ones are the fits, performed in the *absolute* optimal ranges found by the algorithm in Appendix C.1.
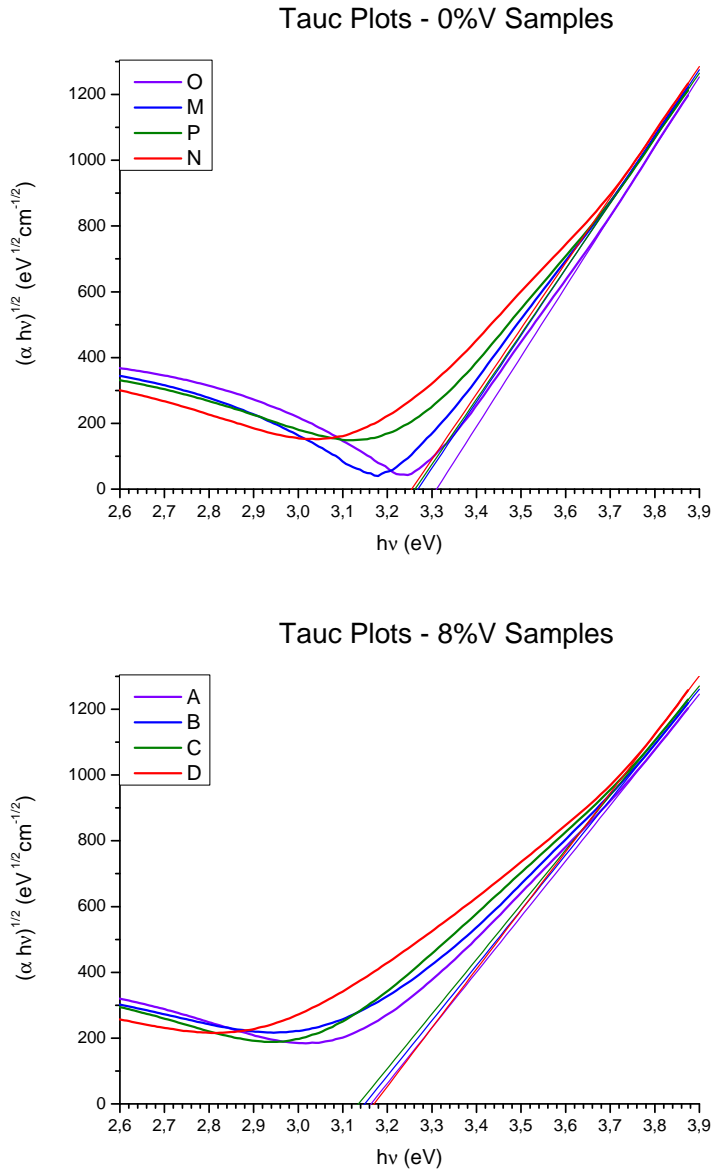
Figure A.12: *Tauc-plots* obtained from the transmission spectra of the undoped (top) and doped samples (bottom). The thick lines are the actual data, the thin ones are the fits, performed in the *absolute* optimal ranges found by the algorithm in Appendix C.1.
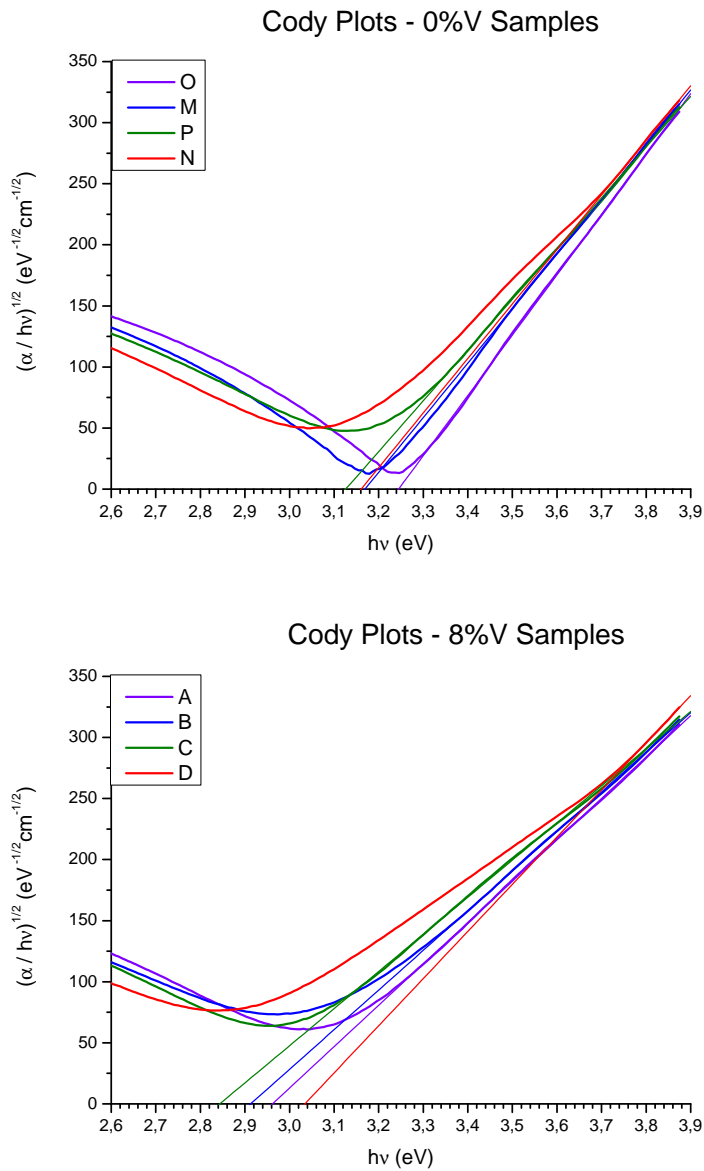
Figure A.13: *Cody-plots* obtained from the transmission spectra of the undoped (top) and doped samples (bottom). The thick lines are the actual data, the thin ones are the fits, performed in the optimal ranges starting at the *highest energy* available found by the algorithm in AppendixC.2.

A.4 Transmission Spectra Analysis

To study the combined effect of doping and NPs on the TiO_2, as the thin-film-interference-fringes could not be removed from the data, the quantities (4.5) and (4.6) are studied. Following are shown the resulting plots, coupled by the nanoparticle deposited on the sample, to better compare the doping effect. The qualitative and quantitative analysis of the plots is in Section 4.6.2.
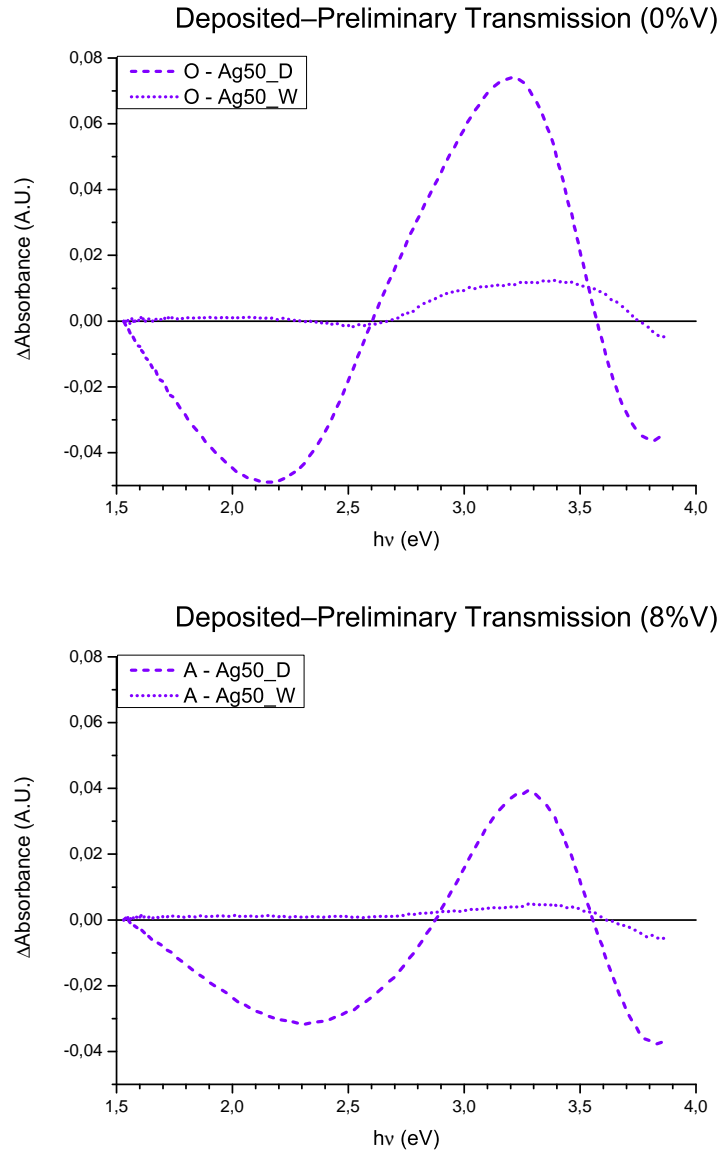
Figure A.14: *Absorbance* difference respect to the *bare* sample of the *deposited* (dashed line) and *washed* (dotted line) datasets, for the samples with $Ag50nm$. The asymmetrical peak shape in the *deposited* samples, as well as the broad peak in the *washed* ones can be explained by the presence of the extinction peak of the nanoparticles present at those energies. No substantial difference is visible among the plots.
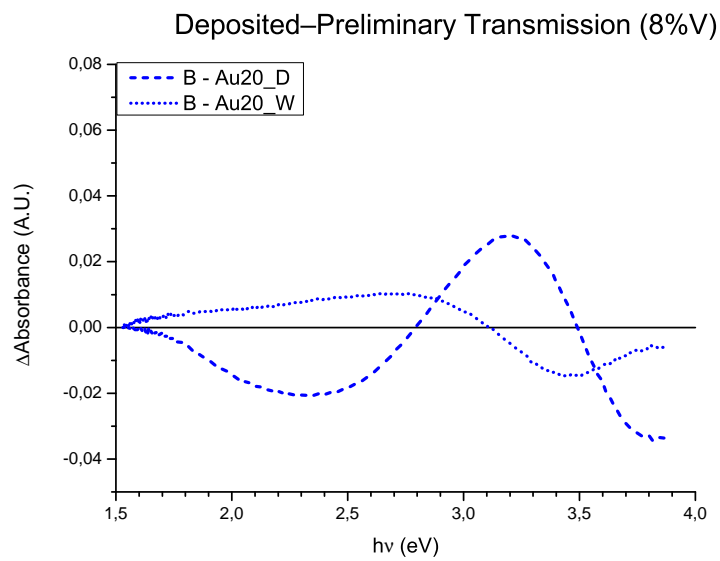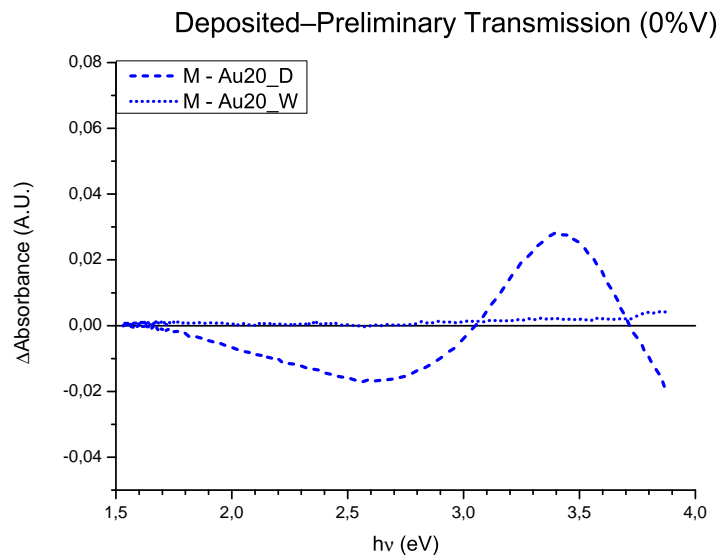
Figure A.15: *Absorbance* difference respect to the *bare* sample of the *deposited* (dashed line) and *washed* (dotted line) datasets, for the samples with $Au20nm$. A significant redshift of the *deposited* peak is visible, while the *washed* plot of sample M completely lacks any feature.
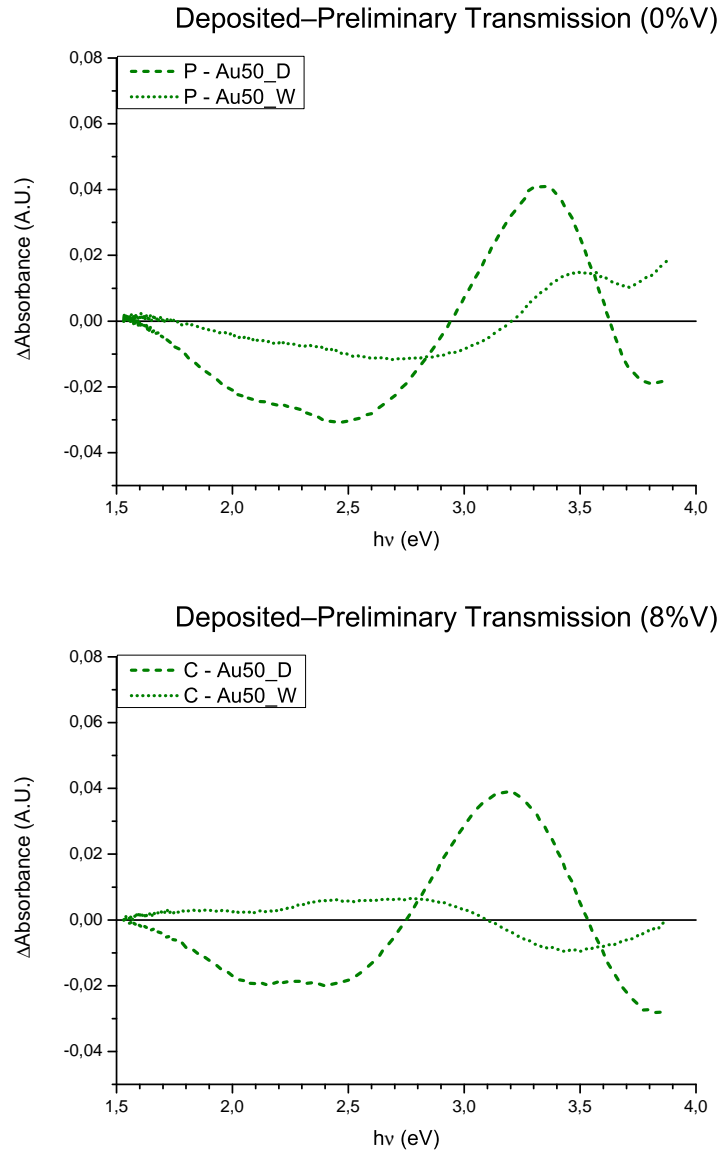
Figure A.16: *Absorbance* difference respect to the *bare* sample of the *deposited* (dashed line) and *washed* (dotted line) datasets, for the samples with $Au50nm$. A significant redshift of the *deposited* peak is visible, while the *washed* plots show similar yet mirrored shape. The "double valleys" between $2 \div 2.5eV$ are probably due to the NPs absorption, but the feature is too weak to be properly analysed.
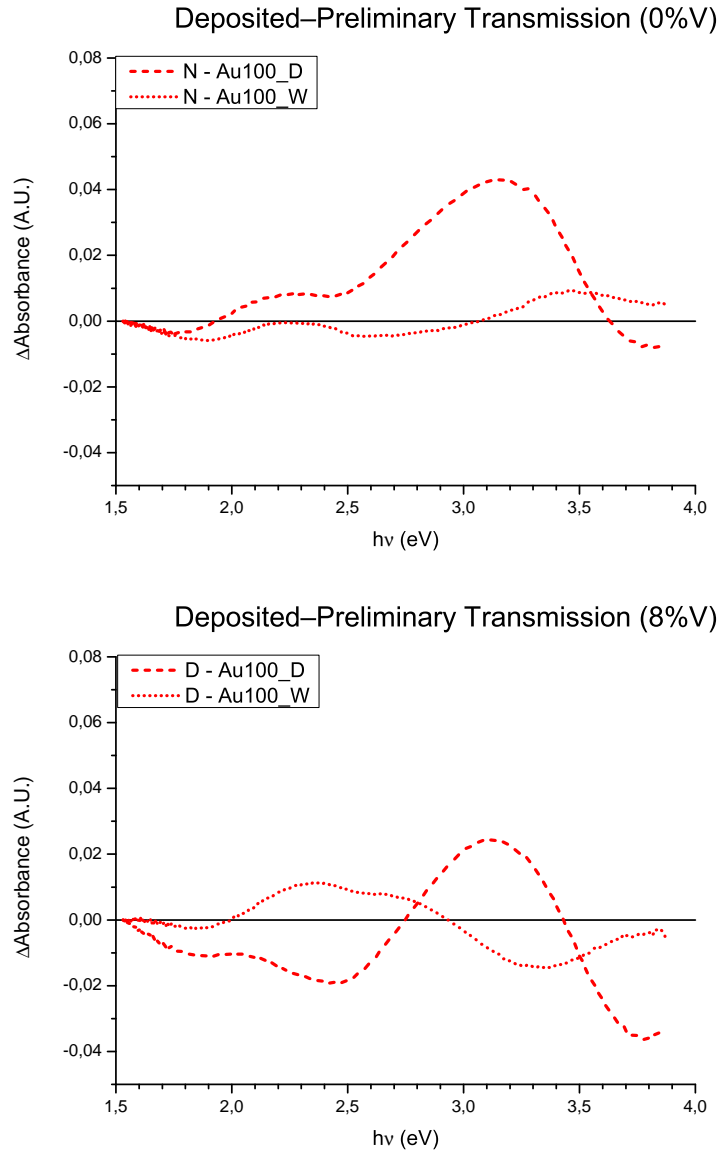
Figure A.17: *Absorbance* difference respect to the *bare* sample of the *deposited* (dashed line) and *washed* (dotted line) datasets, for the samples with $Au100nm$. No substantial difference is visible among the *deposited* plots, while the *washed* ones show similar yet mirrored shape. The "double valleys" between $1.5 \div 2.5eV$ are probably due to the NPs absorption, but the feature is too weak to be properly analysed.

A.5   Reflection Spectra Analysis

In a similar fashion as done in the preceding appendix, the quantities (4.7) and (4.8) are studied. Following are shown the resulting plots, coupled by the nanoparticle deposited on the sample, to better compare the doping effect. The qualitative and quantitative analysis of the plots is in Section 4.6.3.
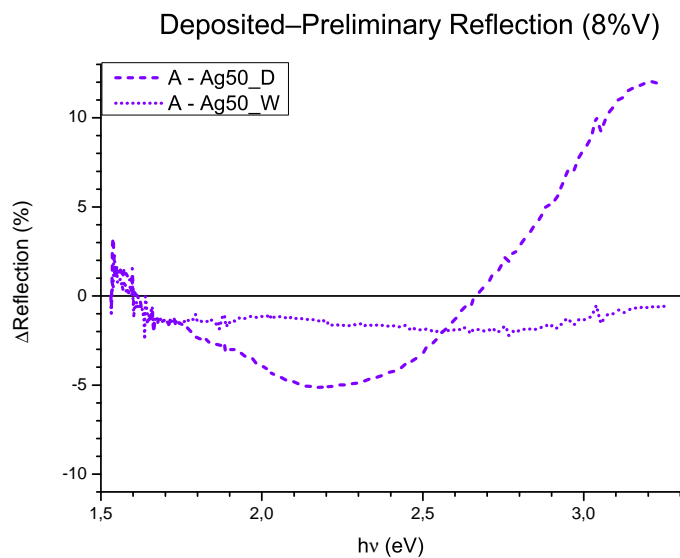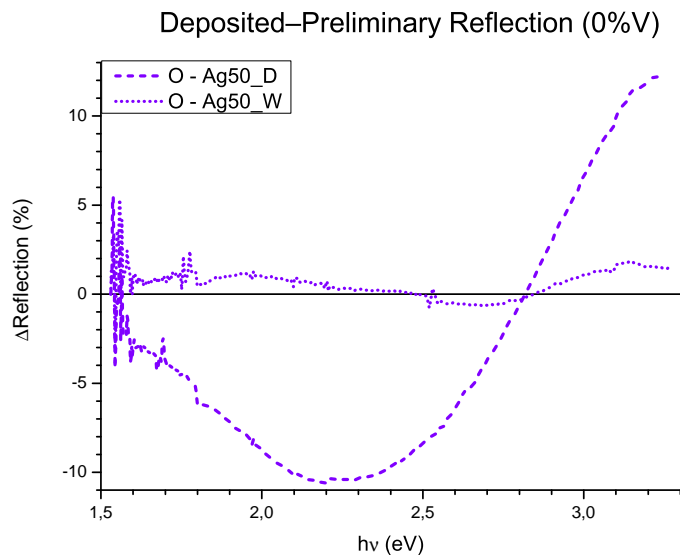
Figure A.18: *Reflectance* difference respect to the *bare* sample of the *deposited* (dashed line) and *washed* (dotted line) datasets, for the samples with $Ag50nm$. No substantial difference is visible among the plots, and the *washed* plots lack any significant feature.
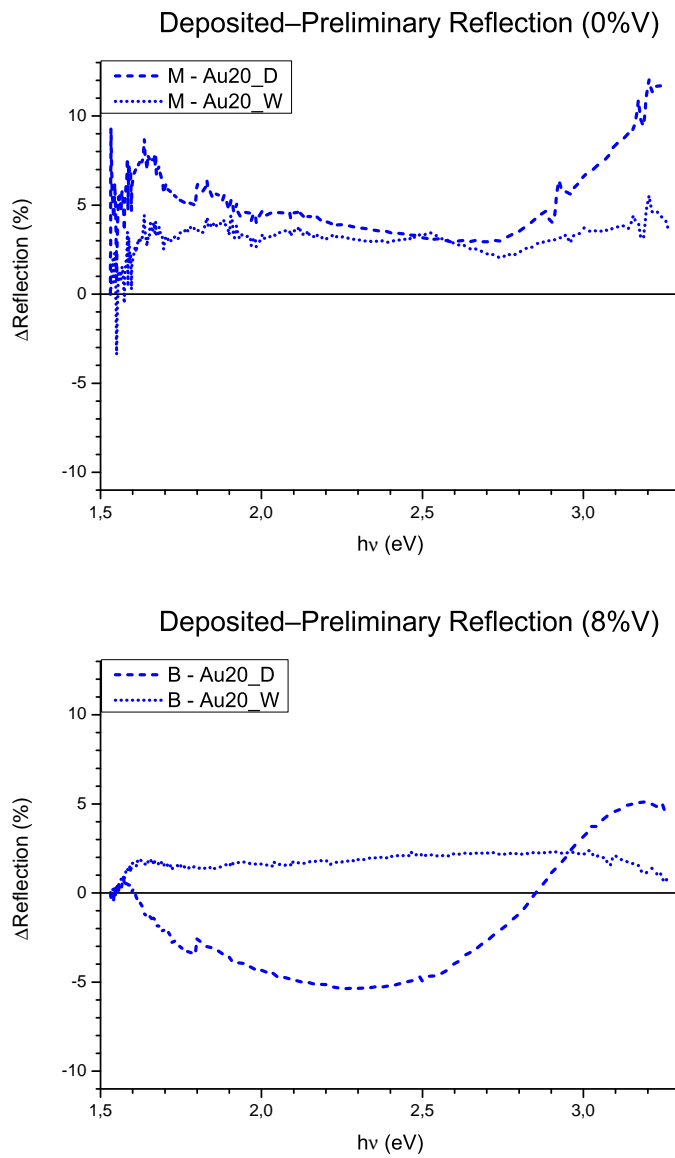
Figure A.19: *Reflectance* difference respect to the *bare* sample of the *deposited* (dashed line) and *washed* (dotted line) datasets, for the samples with *Au20nm*. A significant redshift of the *deposited* peak is visibl; on the contrary the *washed* plots lack any significant feature.
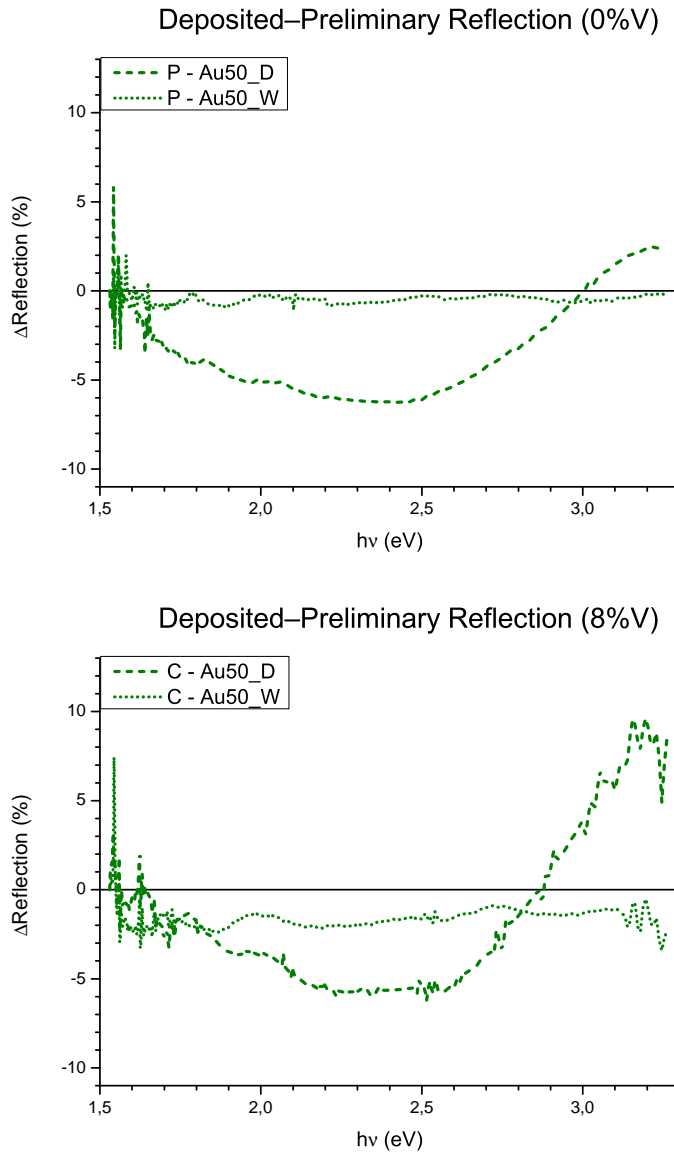
Figure A.20: *Reflectance* difference respect to the *bare* sample of the *deposited* (dashed line) and *washed* (dotted line) datasets, for the samples with $Ag50nm$. No substantial difference is visible among the plots, and the *washed* plots lack any significant feature. The small peak around $2eV$ is due to the NPs, but the feature is too weak to be properly analysed.

Deposited–Preliminary Reflection (0%V)

Deposited–Preliminary Reflection (8%V)
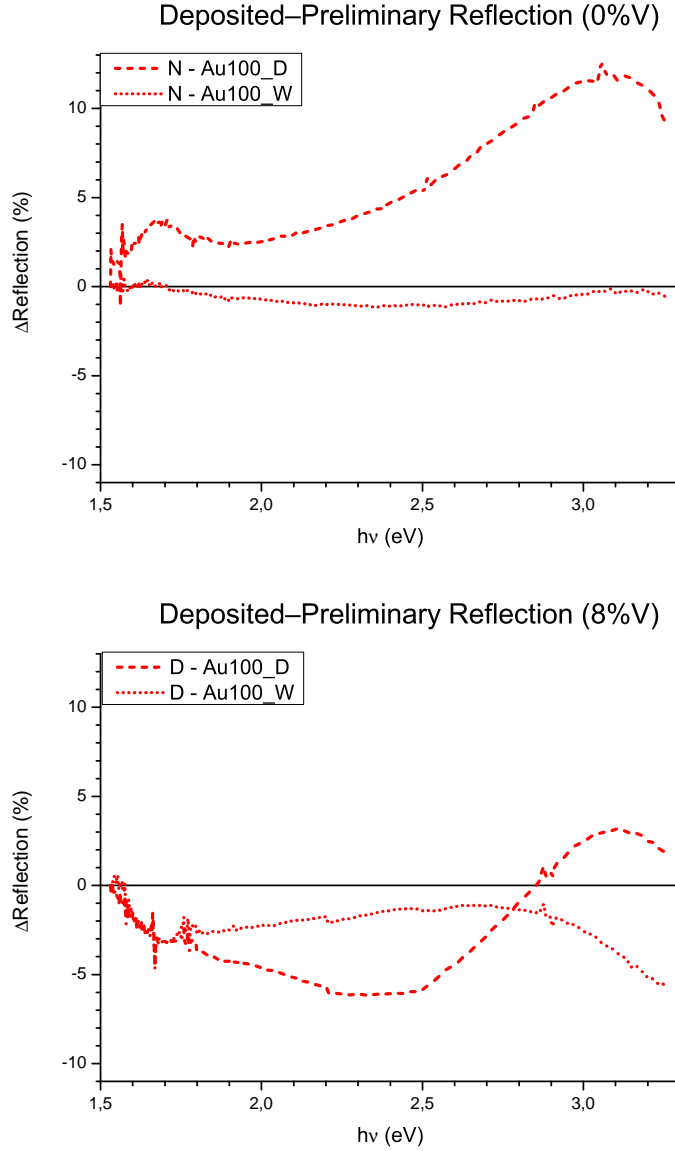
Figure A.21: *Reflectance* difference respect to the *bare* sample of the *deposited* (dashed line) and *washed* (dotted line) datasets, for the samples with $Ag50nm$. No substantial difference is visible among the *deposited* plots, while the *washed* plot of sample M lacks any feature, and the D one shows a valley-like feature at energies above the bandgap. The small peaks around $1.5 - 1.7eV$ are due to the NPs, but are too weak to be properly analysed.

B - Absorption Coefficient from Absorbance Measurements

The transmission measurements performed in this thesis gave their results as *absorbance A*, measured in *absorption units A.U.*. In order to use these measurements to investigate the bangap of the samples these values must be converted in *absorption coefficient*, measured in m^{-1}.
The *Beer-Lambert law* states

$$10^{-A} = e^{-\tau} \equiv T \tag{B.1}$$

where τ is the *attenuation coefficient* and T is the *transmittance* through the material studied. Following the *linear attenuation* approximation, the two quantities can be considered linearly dependent through the *optical path d* travelled by light:

$$\tau = d\alpha \tag{B.2}$$

and in thin films d can be considered their thickness. Combining (B.1) with (B.2):

$$A = d\alpha \log e \tag{B.3}$$

is obtained. From here it is elementary to reach the explicit:

$$\alpha = \ln 10 \frac{A}{d} \simeq 2.30259 \frac{A}{d} \qquad [m^{-1}] \tag{B.4}$$

C - MATLAB Scripts

In order to perform the best fits on the *Tauc-* and *Cody-plots* of the samples to calculate their bandgap, MATLAB scripts able to find the best regions where to perform the fits were needed.

The first script written, simply finds the subset of points that are *best* linearly fitted inside the dataset.

As concerns were present that the best subset might be part of a part of the dataset corrupted by thin film interference effects, another script was developed. It varies only slightly from the first one, simply adding the constraint that the top edge of the subset searched is the *highest* energy point available in the dataset. This way, as the thin film interference in the samples should appear only at mid-low energies ($\lesssim 3.5 \div 3.6 eV$), the subset found shouldn't be affected by it, though it would lack the precision that a large set provides. The full source code is available on GitHub [64]. A brief description of the scripts now follows.

C.1 "Best" Linear-fit-region Finder

This script works by calculating the pseudo-derivative of the dataset provided, and finding the subset of it which best fits a horizontal line. This means that the script is searching for the subset with the least varying derivative.

The pseudo-derivative of a point is calculated as the slope of the line passing between the two other points adjacent to it. The user define the size of the subset to be fitted, and the script starts fitting all the possible subset of adjacent points of that size. Instead of fitting every time a horizontal line, the average value of the points in the subset is used, and the *reduced* χ^2 is calculated. After all the dataset has been examined, the script prints a graph with the pseudo-derivative plot, the best fitted horizontal line, the boundaries of the subset and its calculated chi^2.

The process of finding the best number of points in the subset is not automated and must be performed manually by the user. The protocol to follow is to start

the script with a big number of subset elements, e.g. 15, and then proceed to reduce this number until $\chi^2 \lesssim 1$ and then stop to prevent over-fitting.

C.2 "High-energy" Linear-fit-region Finder

This script is a modification of the previous one. It aims at finding the largest subset of the pseudo-derivative dataset which better fits a horizontal line. There is also the added constraint that the upper limit of the subset must be the point with highest energy of the dataset.

The script starts by trying to fit the whole dataset, and iteratively removing le lowest-energy point until either the calculated χ^2 becomes $\lesssim 1$, or the subset size reaches 3 points. In this case the process is automatic and no user intervention is necessary, but the calculations performed are the same as those described in Appendix C.1.

D - Dark Field (DF) Microscopy Images

These images are the most significant representation of the DF microscopy performed on the samples. From them it is possible to evaluate the deposition quality and the efficiency of the washing routine.

It is clearly visible that the *Ag* particles show much less clustering and dirt residues than the *Au* ones. This can be explained by the different solutions in which they were provided, and it is safe to assume that the whitish items visible in the *Au* samples are residues of the citrate capping of the particles.

Clustering is observed to be stronger in smaller particles than in bigger ones. The washing procedure resulted efficient in cleaning the samples from the residues, as well as removing the main part of big particles clusters. However, clustering persist in the washed samples too, though less prominently, and the total number of particles available to be measured is significantly decreased.

The procedures used in this thesis might prove efficient in measuring single-particle spectra, though not reliably. The ensemble measurements performed, on the other hand, do inevitably suffer from NP-NP interactions.
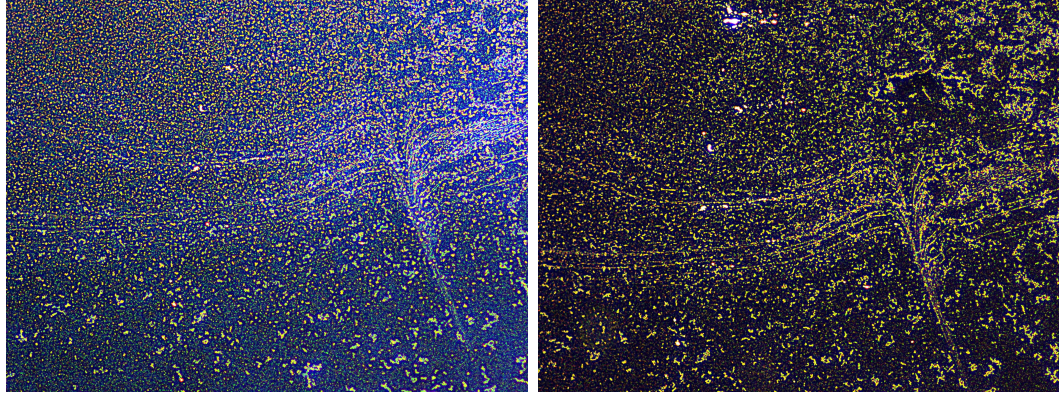
Figure D.1: *DF microscopy images* of sample *O* after the NP deposition (left) and after washing (right). The *deposited* and *washed* samples are not much different, the only apparent change being the disappearance of the "white halo" after washing; this is probably due to the solutions residuals being washed away. The area shown in each image is $352\mu m$.
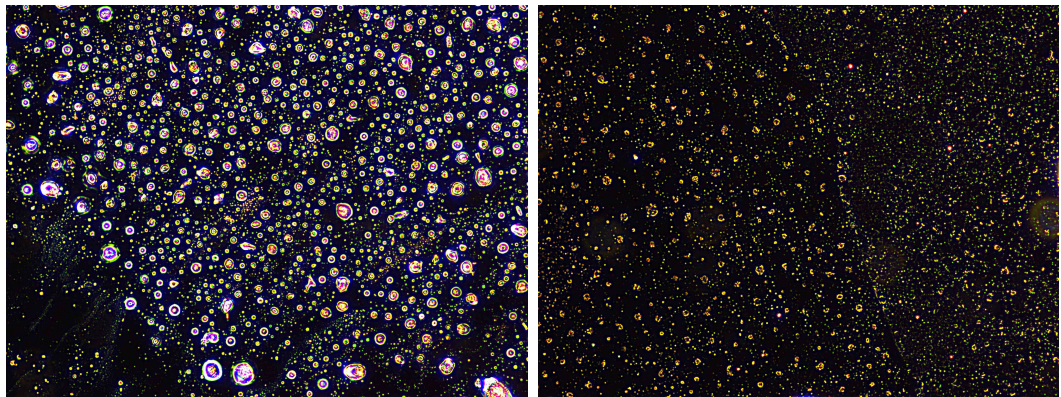
Figure D.2: *DF microscopy images* of sample *M* after the NP deposition (left) and after washing (right). Significant clustering is visible in both samples, though slightly less in the *washed* one; the whitish objects in the *deposited* sample are probably citrate residues, which disappear after washing. The area shown in each image is $352\mu m$.
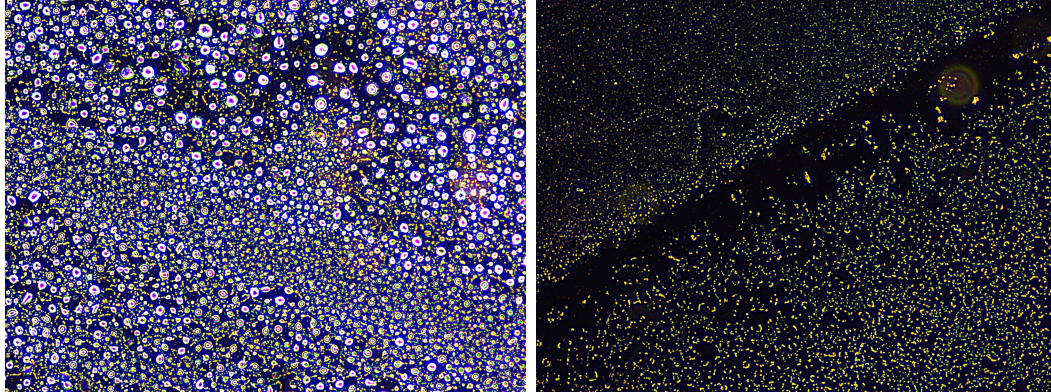
Figure D.3: *DF microscopy images* of sample P after the NP deposition (left) and after washing (right). Significant clustering is visible in both samples, though slightly less in the *washed* one; the whitish objects in the *deposited* sample are probably citrate residues, which disappear after washing. The area shown in each image is $352\mu m$.
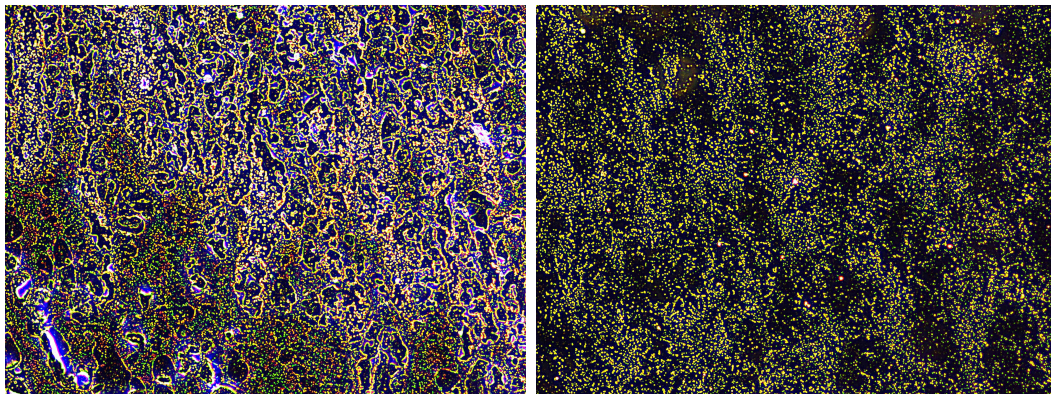
Figure D.4: *DF microscopy images* of sample N after the NP deposition (left) and after washing (right). Clustering is visible in both samples, though it is much less prominent in the *washed* one; the whitish objects in the *deposited* sample are probably citrate residues, which disappear after washing. The area shown in each image is $352\mu m$.
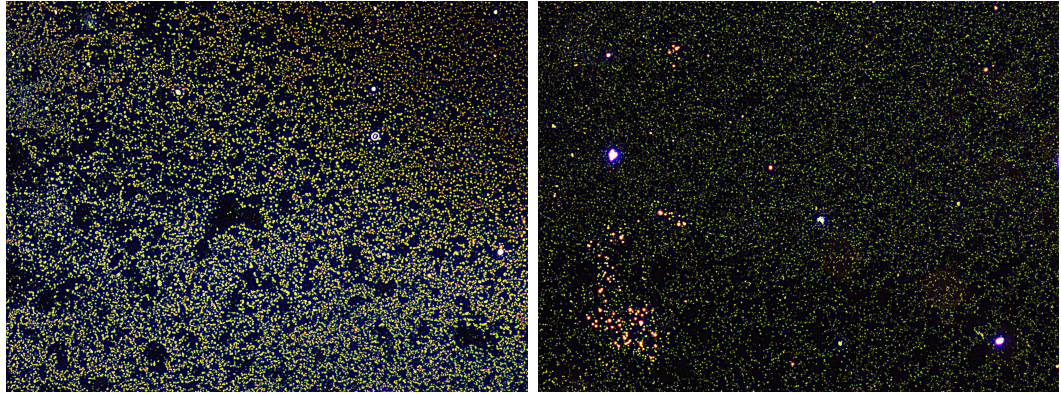
Figure D.5: *DF microscopy images* of sample *A* after the NP deposition (left) and after washing (right). The *washed* sample is more sparsely populated, and some clustering features are present anyway. The area shown in each image is $352\mu m$.
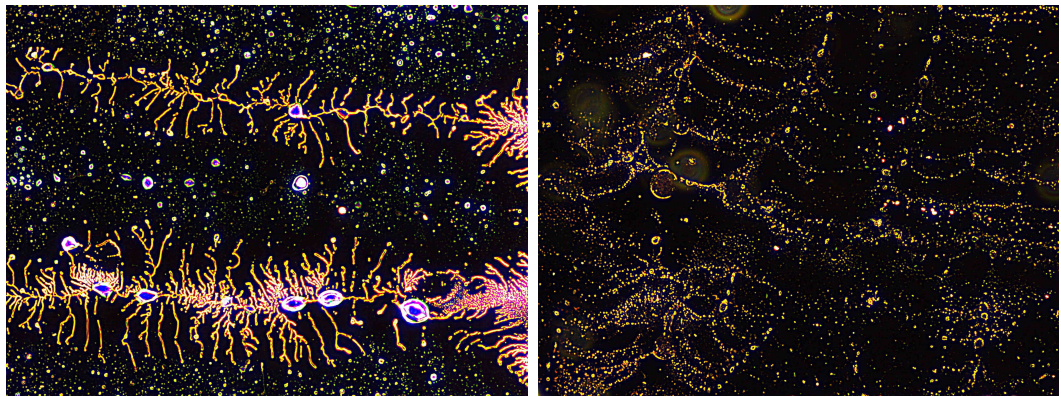
Figure D.6: *DF microscopy images* of sample *B* after the NP deposition (left) and after washing (right). Clear, structured clustering is visible in both samples, though much more evident in the *deposited* one; the whitish objects in the *deposited* sample are probably citrate residues, which disappear after washing. The area shown in each image is $352\mu m$.
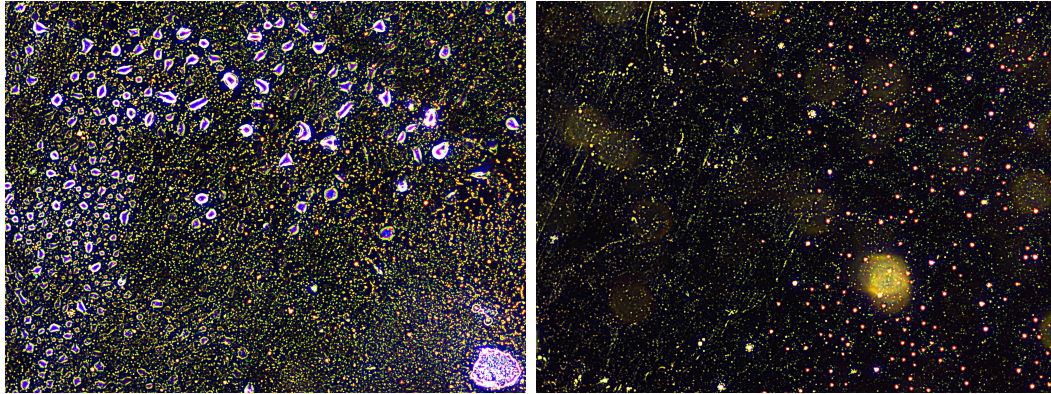
Figure D.7: *DF microscopy images* of sample C after the NP deposition (left) and after washing (right). Clustering is visible in both samples, though less in the *washed* one; the whitish objects in the *deposited* sample are probably citrate residues, which disappear after washing; the lines of particles in the *washed* sample probably clustered during the drying process, following its path. The area shown in each image is $352\mu m$.
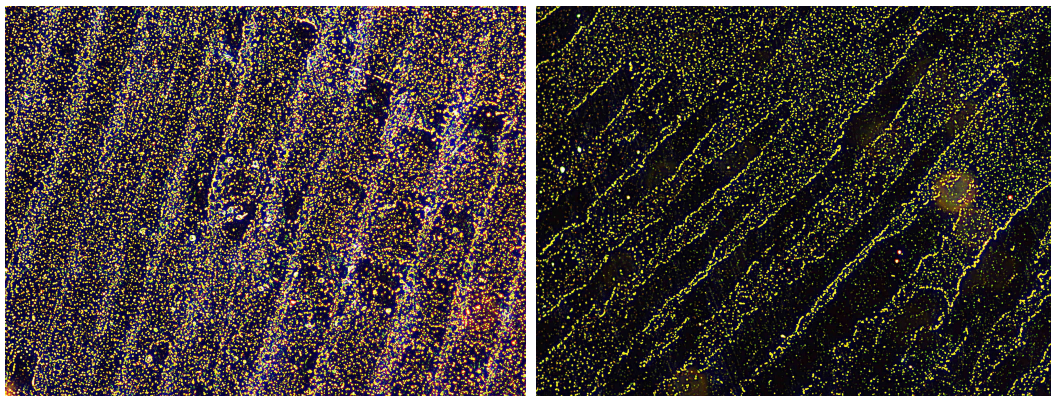
Figure D.8: *DF microscopy images* of sample D after the NP deposition (left) and after washing (right). Clustering is visible in both samples, though less in the *washed* one; the whitish objects in the *deposited* sample are probably citrate residues, which disappear after washing; the structures visible in both samples probably formed during the drying process. The area shown in each image is $352\mu m$.

Bibliography

[1] Bjørn Jamtveit and Paul Meakin. "Wolfgang Pauli, quoted in Schroeder, 1991". In: *Growth, Dissolution and Pattern Formation in Geosystems.* Springer Netherlands, 1999, p. 291.

[2] Edna R. Spada et al. "Preparation, characterization and application of phase-pure anatase and rutile TiO2 nanoparticles by new green route". In: *Journal of Materials Science: Materials in Electronics* (2017). DOI: `10.1007/s10854-017-7613-z`.

[3] mindat.org, ed. *Definition of titanium dioxide.* URL: `https://www.mindat.org/glossary/titanium_dioxide`.

[4] Ryan Lance and Janet Tate. "Optical Analysis of Titania: Band Gaps of Brookite, Rutile and Anatase". Oregon State University, 2018.

[5] David O. Scanlon et al. "Band alignment of rutile and anatase TiO2". In: 12.July (2013), pp. 10–13. DOI: `10.1038/nmat3697`.

[6] Zhijun Yi and Ran Jia. "The electronic structure and optical response of The electronic structure and optical response of rutile , anatase and brookite". In: *Journal of Physics: Condensed Matter* (2012). DOI: `10.1088/0953-8984/24/19/195503`.

[7] Tsutomu Umebayashi et al. "Analysis of electronic structures of 3d transition metal-doped TiO2 based on band calculations". In: *Journal of Physics and Chemistry of Solids* 63.10 (2002), pp. 1909–1920. DOI: `10.1016/S0022-3697(02)00177-4`.

[8] W. Avansi et al. "Vanadium-doped TiO2 anatase nanostructures: the role of V in solid solution formation and its effect on the optical properties". In: *CrystEngComm* 16.23 (2014), pp. 5021–5027. DOI: `10.1039/C3CE42356E`.

[9]   H. X. Zhu et al. "First-principles study on electronic, magnetic properties and optical absorption of vanadium doped rutile TiO2". In: *Physics Letters, Section A: General, Atomic and Solid State Physics* 384.26 (2020), p. 126637. DOI: 10.1016/j.physleta.2020.126637. URL: https://doi.org/10.1016/j.physleta.2020.126637.

[10] Giacomo Rossi et al. "Charge carrier dynamics and visible light photocatalysis in vanadium-doped TiO2 nanoparticles". In: *Applied Catalysis B: Environmental* 237 (2018), pp. 603–612. DOI: 10.1016/j.apcatb.2018.06.011.

[11] Emanuele Centurioni. "Generalized matrix method for calculation of internal light energy flux in mixed coherent and incoherent multilayers". In: *Appll. Opt.* 44.35 (2005), pp. 7532–7539. DOI: 10.1364/AO.44.007532.

[12] A. S. Ferlauto et al. "Analytical model for the optical functions of amorphous semiconductors from the near-infrared to ultraviolet: Applications in thin film photovoltaics". In: *Journal of Applied Physics* 92.5 (2002), pp. 2424–2436. DOI: 10.1063/1.1497462.

[13] D. Ritter and K. Weiser. "Suppression of interference fringes in absorption measurements on thin films". In: *Optics Communications* 57.5 (1986), pp. 336–338. DOI: 10.1016/0030-4018(86)90270-1.

[14] F. Neri, G. Saitta, and S. Chiofalo. "A simple procedure to remove the interference fringes from optical spectra". In: *J. Phys. E.: Sci. Instrum* 20 (1987).

[15] Neil W. Ashcroft and N. David Mermin. "AC Electrical Conductivity of a Metal". In: *Solid State Physics*. 1976. Chap. 1.5.

[16] C. J. Powell and J. B. Swan. "Origin of the Characteristic Electron Energy Losses in Aluminum". In: *Physical Review Letters* 115.4 (1959), p. 869. DOI: https://doi.org/10.1103/PhysRev.115.869.

[17] Shuwen Zeng et al. "Nanomaterials enhanced surface plasmonresonance for biological and chemicalsensing applications". In: *Chem Soc Rev* 43 (2014), pp. 3426–3452. DOI: 10.1039/c3cs60479a.

[18] Matteo Parente. "0D and 1D Metals: Plasmonic Sensors and Charge Conductors". PhD thesis. Technische Universiteit Eindhoven, 2020. Chap. 2.

[19] Stefan A. Maier and Harry A. Atwater. "Plasmonics: Localization and guiding of electromagnetic energy in metal/dielectric structures". In: *Journal of Applied Physics* 98.1 (2005). DOI: 10.1063/1.1951057.

[20] Sigma-Aldrich (Merck KGaA), ed. *Gold Nanoparticles: Properties and Applications*. URL: https : / / www . sigmaaldrich . com / technical - documents / articles / materials - science / nanomaterials / gold - nanoparticles.html#newMaterials.

[21] Steven J. Oldenburg. *Silver Nanoparticles: Properties and Applications*. Ed. by Sigma-Aldrich (Merck KGaA). URL: https://www.sigmaaldrich. com/technical-documents/articles/materials-science/nanomaterials/ silver-nanoparticles.html.

[22] Jack J. Mock et al. "Distance-dependent plasmon resonant coupling between a gold nanoparticle and gold film". In: *Nano Letters* 8.8 (2008), pp. 2245–2252. DOI: 10.1021/nl080872f.

[23] Roel van de Krol and Michael Grätzel. *Photoelectrochemical Hydrogen Production*. Ed. by Roel van de Krol and Michael Grätzel. Vol. 102. Electronic Materials: Science & Technology. Boston, MA: Springer US, 2012. ISBN: 978-1-4614-1379-0. DOI: 10.1007/978-1-4614-1380-6. URL: http://link.springer.com/10.1007/978-1-4614-1380-6.

[24] Matthias Graf, Gregor B Vonbun-feldbauer, and Marc T M Koper. "Direct and Broadband Plasmonic Charge". In: (2020). DOI: 10.1021/ acsnano.0c09776.

[25] Lucas V Besteiro et al. *Understanding Hot-Electron Generation and Plasmon Relaxation in Metal Nanocrystals : Quantum and Classical Mechanisms*.

[26] T V Dolgova et al. "Surface-plasmon relaxation dynamics in planar plasmonic crystals". In: *International OSA Network of Students 8-Moscow*. 2010.

[27] Benjamin Foerster et al. "Chemical Interface Damping Depends on Electrons Reaching the Surface". In: *ACS Nano* 11.3 (2017), pp. 2886–2893. DOI: 10.1021/acsnano.6b08010.

[28] M. Perner et al. "Optically induced damping of the surface plasmon resonance in gold colloids". In: *Physical Review Letters* 78.11 (1997), pp. 2192–2195. DOI: 10.1103/PhysRevLett.78.2192.

[29] Min Jung Seo et al. "Role of chemical interface damping for tuning chemical enhancement in resonance surface-enhanced Raman scattering of plasmonic gold nanorods". In: *Nanoscale Horizons* 5.2 (2020), pp. 345–349. DOI: 10.1039/C9NH00524B.

[30] Matteo Parente et al. "Equilibration of Photogenerated Charge Carriers in Plasmonic Core@Shell Nanoparticles". In: *Journal of Physical Chemistry C* 122.41 (2018), pp. 23631–23638. DOI: `10.1021/acs.jpcc.8b05003`.

[31] Ferry Anggoro Ardy Nugroho et al. "Topographically Flat Nanoplasmonic Sensor Chips for Biosensing and Materials Science". In: *Acs Sensors* (2016). DOI: `10.1021/acssensors.6b00612`.

[32] Ferry Anggoro Ardy Nugroho et al. "A fiber-optic nanoplasmonic hydrogen sensor via pattern-transfer of nanofabricated PdAu alloy nanostructures". In: *Nanoscale* 10 (2018), pp. 20533–20539. DOI: `10.1039/c8nr03751e`.

[33] Oxford Vacuum Science, ed. *Sputter Deposition*. URL: `http://www.oxford-%20vacuum.com/background/thin_film/sputtering.htm`.

[34] Matteo Bischi and Luca Pasquini. "Realizzazione di un impianto di magnetron sputtering per la deposizione di film sottili". PhD thesis. Alma Mater Studiorum - Università di Bologna, 2017.

[35] E V Shun and V S Belkin. "Cleaning properties of atomic oxygen excited to metastable state 2s2 2p4 (1S0)". In: *Journal of Applied Physics* 102 (2012). DOI: `10.1063/1.2794857`.

[36] diener, ed. *Translation of the operating and maintenance manual*. Zepto. s.n. 119300. 2019.

[37] Kyung Rok Choi et al. "Dry etching properties of TiO2 thin films in O 2/CF4/Ar plasma". In: *Vacuum* 92 (2013), pp. 85–89. DOI: `10.1016/j.vacuum.2012.11.009`.

[38] "Formation of oxygen vacancies and Ti3+ state in TiO2 thin film and enhanced optical properties by air plasma treatment". In: *Scientific Reports* 6.August (2016), pp. 1–12. DOI: `10.1038/srep32355`. URL: `http://dx.doi.org/10.1038/srep32355`.

[39] Neil W. Ashcroft and N. David Mermin. "Dtetermination of Crystal Structures by X-ray Diffraction". In: *Solid State Physics*. 1976. Chap. 6.

[40] Bruker, ed. *DIFFRAC.EVA*. URL: `https://www.bruker.com/content/bruker/int/en/products-and-solutions/diffractometers-and-scattering-systems/x-ray-diffractometers/diffrac-suite-software/diffrac-eva.html`.

[41] Q. Yang and L. R. Zhao. "Characterization of nano-layered multilayer coatings using modified Bragg law". In: *Materials Characterization* 59.9 (2008), pp. 1285–1291. DOI: `10.1016/j.matchar.2007.11.001`.

[42] Matts Björck and Gabriella Andersson. "GenX: An extensible X-ray reflectivity refinement program utilizing differential evolution". In: *Journal of Applied Crystallography* 40.6 (2007), pp. 1174–1178. DOI: `10.1107/S0021889807045086`. URL: `https://genx.sourceforge.io/`.

[43] "X-Ray Interactions: Photoabsorption, Scattering, Transmission, and Reflection at E = 50-30,000 eV, Z = 1-92". In: *Atomic Data and Nuclear Data Tables* 54.2 (1993), pp. 181–342. DOI: `https://doi.org/10.1006/adnd.1993.1013`. URL: `https://henke.lbl.gov/optical_constants/`.

[44] Alexandre Rothen. "The Ellipsometer, an Apparatus to Measure Thicknesses of Thin Surface Films". In: *Review of Scientific Instruments* 16.2 (1945), pp. 26–30. DOI: `10.1063/1.1770315`.

[45] J. A. Woollam Co., ed. *CompleteEASE® Software Manual*. Version 4.63. Data Acquisition and Analysis Software for J.A. Woollam Co. Spectroscopic Ellipsometers. 2014.

[46] Harland G Tompkins and Eugene A Irene, eds. *Handbook of Ellipsometry*. William Andrew Publishing & Springer, 2005.

[47] Mikhail N. Polyanskiy. *Refractive index database*. URL: `https://refractiveindex.info`.

[48] Buntgarn. *Ellipsometry setup*. Buntgarn, at the English Wikipedia project, CC BY-SA 3.0 ¡http://creativecommons.org/licenses/by-sa/3.0/¿, via Wikimedia Commons. 2008. URL: `https://commons.wikimedia.org/wiki/File:Ellipsometry_setup.svg`.

[49] Josef Humlíček. "Polarized Light and Ellipsometry". In: *Handbook of Ellipsometry*. Ed. by Harland G Tompkins and Eugene A Irene. William Andrew Publishing & Springer, 2005. Chap. 1.

[50] Mathias Schubert. "Theory and Application of Generalized Ellipsometry". In: *Handbook of Ellipsometry*. Ed. by Harland G Tompkins and Eugene A Irene. [William Andrew Publishing, Springer], 2005. Chap. 9.

[51] Simon Henry Gage. "Modern Dark-Field Microscopy and the History of Its Development". In: *Transactions of the American Microscopical Society* 39.2 (1920), pp. 95–141.

[52] William Chambers, Fellers Thomas J., and Michael W. Davidson. *Darkfield Illumination*. Nikon Instruments Inc. URL: `https://www.microscopyu.com/techniques/stereomicroscopy/darkfield-illumination`.

[53] R0oland. *Dark Field Microscope @D*. R0oland, CC BY-SA 3.0 ¡https://creativecommons.org/lice sa/3.0¿, via Wikimedia Commons. 2012. URL: `https://commons.wikimedia.org/wiki/File:Dark_Field_Microscope_@D..svg`.

109

[54] "Wide-field hyperspectral 3D imaging of functionalized gold nanoparticles targeting cancer cells by reflected light microscopy". In: *Journal of Biophotonics* 8.5 (2015), pp. 401–407. DOI: https://doi.org/10.1002/jbio.201400025.

[55] David Barthelmy, ed. *Anatase Mineral Data*. URL: http://webmineral.com/data/Anatase.shtml#.YD4h_NzSLIX.

[56] J. Tauc, R. Grigorovici, and A. Vancu. "Optical Properties and Electronic Structure of Amorphous Germanium". In: *Physica Status Solidi b* 15.2 (1966), pp. 627–637. DOI: https://doi.org/10.1002/pssb.19660150224.

[57] Tat M. Mok and Stephen K. O' Leary. "The dependence of the Tauc and Cody optical gaps associated with hydrogenated amorphous silicon on the film thickness: α l Experimental limitations and the impact of curvature in the Tauc and Cody plots". In: *Journal of Applied Physics* 102.11 (2007), p. 113525. DOI: 10.1063/1.2817822.

[58] Pei Liu et al. "Optical bandgap of single- and multi-layered amorphous germanium ultra-thin films". In: *Journal of Applied Physics* 119.1 (2016). DOI: 10.1063/1.4939296. URL: http://dx.doi.org/10.1063/1.4939296.

[59] Lucia Amidani et al. "Probing Long-Lived Plasmonic-Generated Charges in TiO 2 /Au by High-Resolution X-ray Absorption Spectroscopy". In: *Angewandte Chemie* 127.18 (2015), pp. 5503–5506. DOI: 10.1002/ange.201412030.

[60] Kane Yee. "Numerical solution of initial boundary value problems involving maxwell's equations in isotropic media". In: *IEEE Transactions on Antennas and Propagation* 14.3 (1966), pp. 302–307. DOI: 10.1109/TAP.1966.1138693.

[61] Honghua U. Yang et al. "Optical dielectric function of silver". In: *Phys. Rev. B* 91 (23 June 2015), p. 235137. DOI: 10.1103/PhysRevB.91.235137.

[62] P. B. Johnson and R. W. Christy. "Optical Constants of the Noble Metals". In: *Phys. Rev. B* 6 (12 Dec. 1972), pp. 4370–4379. DOI: 10.1103/PhysRevB.6.4370.

[63] S. K. WILSON, R. HUNT, and B. R. DUFFY. "The rate of spreading in spin coating". In: *Journal of Fluid Mechanics* 413 (2000), pp. 65–88. DOI: 10.1017/S0022112000008089.

[64]   Matteo Marchesini a.k.a. Morak-Ants. *Mobile-derivative-linear-fitting*. URL: https://github.com/Morak-Ants/Mobile-derivative-linear-fitting.

Acknowledgements

I would also like to personally thank all the people that actively contributed to the realisation of this project:

First of all, Prof. Luca Pasquini and Prof. Andrea Baldi, Supervisor and Co-supervisor of this thesis, for having given me the chance to realise this project, supporting and guiding me until its completion, even through the multiple and unexpected difficulties occurred in the last, crazy year.

Then Andrea Piccioni, for his valuable contribution provided in the initial stages of the thesis preparation.

Finally, the NEA people at DIFFER: Ruben Hamans, Francesco Verdelli and especially Dr. Ferry A. A. Nugroho, for their welcoming spirit and for always being there whenever I troubled them asking for help.

Matteo Marchesini